

NASA Contractor Report 174668

A Theoretical and Experimental Study of Turbulent Nonevaporating Sprays

A. S. P. Solomon, J-S. Shuen, Q-F. Zhang, and G. M. Faeth

The Pennsylvania State University
University Park, Pennsylvania

June 1984

Prepared for

NATIONAL AERONAUTICS AND SPACE ADMINISTRATION
Lewis Research Center
Under Grant NAG 3-190

TABLE OF CONTENTS

	<u>Page</u>
SUMMARY.	1
NOMENCLATURE	3
1. INTRODUCTION	5
2. THEORY	7
2.1 Introduction.	7
2.2 Locally Homogeneous Flow Model.	8
2.2.1 Governing Equations.	8
2.2.2 State Relationships.	9
2.2.3 Computations	11
2.3 Deterministic Separated Flow Model.	12
2.3.1 Discrete Phase	12
2.3.2 Continuous Phase	13
2.4 Stochastic Separated Flow Model	14
3. EXPERIMENTAL METHODS	15
3.1 Introduction.	16
3.2 Test Apparatus.	16
3.3 Measurement Techniques and Instrumentation.	19
3.3.1 Gas-Phase Velocity Measurements.	19
3.3.2 Liquid-Phase Properties.	22
3.3.2.1 Drop Size Measurements.	22
3.3.2.2 Drop Size and Velocity Correlation Measurement	24
3.3.2.3 Liquid Flux Measurement	28
3.3.3 Jet Momentum Measurement	28
3.4 Experimental Conditions	28
4. RESULTS AND DISCUSSION	31
4.1 Introduction.	31
4.2 Air-Jet Calibration	31
4.3 Initial Conditions.	31
4.3.1 Jet Momentum, Spray Angle and Gas-Phase Properties	31
4.3.2 Liquid-Phase Properties.	34
4.4 Axial Variation of Spray Properties	47
4.5 Radial Variation of Mean-Spray Properties	57
4.6 Radial Variation of Gas-Phase Turbulence Properties	61
4.7 Sensitivity Study	69
5. SUMMARY AND CONCLUSIONS.	76
5.1 Summary	76
5.2 Conclusions	76

TABLE OF CONTENTS (Continued)

	<u>Page</u>
REFERENCES	79
APPENDIX A: BREAKUP OF LIGAMENTS--CASE 2 NONEVAPORATING SPRAY, $x/d = 50$	82
APPENDIX B: DEPTH-OF-FIELD BIAS CORRECTIONS FOR PHOTOGRAPHIC MEASUREMENTS OF DROP SIZE DISTRIBUTIONS	85
APPENDIX C: DATA FOR THE NONEVAPORATING SPRAY (CASE 1). . . .	88
C.1 Gas-Phase Properties.	88
C.2 Liquid-Phase Properties	93
APPENDIX D: DATA FOR THE NONEVAPORATING SPRAY (CASE 2). . . .	111
D.1 Gas-Phase Properties.	111
D.2 Liquid-Phase Properties	116

A Theoretical and Experimental Study of Turbulent Nonevaporating Sprays

SUMMARY

A study of the structure of sprays, limited to the properties of nonevaporating sprays, is described. Several models of these processes were evaluated by comparison of predictions with new measurements in nonevaporating sprays completed during this investigation. Analysis and measurements were limited to the dilute portions of the flows, where the volume fraction of the continuous phase was greater than 99.1%.

Three models of the process were evaluated: (1) a locally homogeneous flow (LHF) model, where slip between the phases was neglected; (2) a deterministic separated flow (DSF) model, where slip was considered but effects of turbulent fluctuations and drop dispersion by the turbulence were ignored; and (3) a stochastic separated flow (SSF) model, where effects of interphase slip, turbulent fluctuations and turbulent dispersion were considered using random sampling for turbulence properties in conjunction with random-walk computations for drop motion. All three models used in $k-\epsilon$ model which was extensively evaluated for constant and variable density single-phase jets during earlier work in this laboratory.

The new spray experiments employed vacuum pump oil--to insure negligible evaporation. The sprays were produced by an air-atomizing injector. Mean and fluctuating velocities and Reynolds stress were measured in the continuous phase using laser Doppler anemometry. Liquid mass fluxes were measured by isokinetic sampling. Drop sizes were measured by slide impaction, Fraunhofer diffraction and photography. Simultaneous measurements of drop size and velocity were obtained using a multiframe photographic technique.

The LHF and DSF models did not provide very satisfactory predictions over the present measurements. The DSF model generally underestimated the rate of spread of the dispersed phase as a result of ignoring effects of turbulent dispersion. The LHF model provided reasonably good predictions for flows containing small drops, but was unsatisfactory for most practical flows. In earlier evaluations, LHF models generally overestimate the rate of spread of dispersed phases due to neglect of slip. However, the LHF model underestimated spread rates for the present nonevaporating sprays. This indicates that LHF models do not always provide an upper bound on the rate of development of dilute drop-laden flows--as suggested in the past.

In contrast to the other models, the SSF model provided reasonably good predictions of the present measurements. While this result is encouraging, uncertainties in initial conditions for some of the data limits the thoroughness of the evaluation of the SSF model. Some effects of drops on turbulence properties were observed in dense regions of the sprays. Treatment of such dense flow effects will require extension of the present SSF model. The SSF approach, however,

appears to provide an attractive formulation for treating nonlinear interphase transport processes in drop-laden turbulent flows. Current work in this laboratory is considering extension of the method to evaporating sprays as well as consideration of effects of turbulence modulation.

NOMENCLATURE

<u>Symbol</u>	<u>Description</u>
a	acceleration of gravity
C_D	drag coefficient
C_i	parameters in turbulence model
d	injector diameter
d_p	drop diameter
f	mixture fraction
G	liquid mass flux
k	turbulence kinetic energy, wave number
L_e	dissipation length scale
m	drop mass
n	number of drop groups
\dot{n}_i	number of drops per unit time in group i
r	radial distance
Re	Reynolds number
S_ϕ	source term
$S_{p\phi}$	drop source term
t	time
t_e	eddy lifetime
u	axial velocity
\vec{u}_p	drop velocity vector
v	radial velocity
We	Weber number
x	axial distance
\vec{x}_p	drop position vector
Z	Ohnesorge number

NOMENCLATURE (Continued)

<u>Symbol</u>	<u>Description</u>
$ \Delta \vec{x}_p $	path length of drops in an eddy
Δt	time of drop residence in an eddy
ϵ	rate of dissipation of turbulence kinetic energy
λ	disturbance wavelength
μ_t	turbulent viscosity
ρ	density
σ_i	turbulent Prandtl/Schmidt number
ϕ	generic property
ω	disturbance growth rate

Subscripts

c	centerline quantity
g	gas-phase property
j	liquid jet property
L	liquid-phase property
p	drop property
0	injector exit condition
∞	ambient condition

Superscripts

$(\bar{})$	time-averaged quantity
$()'$	time-averaged fluctuating quantity
$(\tilde{})$	Favre-averaged quantity
$()''$	Favre-averaged fluctuating quantity
$(\vec{})$	vector quantity

1. INTRODUCTION

The objective of this investigation was to complete measurements of spray structure, useful for evaluation of models of the process. The test considered nonevaporating sprays, generated by an air-atomizing injector, in a still environment. This arrangement has simple geometry and well-defined boundary conditions, which facilitates model evaluation. Furthermore, nonevaporating sprays highlight effects of drops on the properties of the continuous phase and effects of drop dispersion by turbulence in sprays, while minimizing complications due to density variations in the flow. The new data was also used to begin model evaluation considering methods typical of recent spray models.

During the first phase of this study [1-6]¹ models of nonevaporating sprays and particle-laden jets were developed and evaluated, using the existing measurements in particle-laden jets, as well as the new measurements in nonevaporating sprays. While predictions for some models were encouraging, the evaluation was inhibited throughout by insufficient information concerning initial conditions. Moreover, the flow structure data available in the existing measurements were not complete in most of the cases, which further hindered model evaluation.

Subsequently, complete measurements of the structure of particle-laden jets were undertaken in this laboratory to supplement the data base of existing measurements in the literature [7,8]. The experiments considered dilute solid-particle-laden jets in a still environment, considering three particle-size groups and two loading ratios. Measurements included mean and fluctuating velocities of both phases, particle mass fluxes, particle size distributions, and calibration of particle drag properties. Particular attention was given to defining initial conditions of the flows, to obtain definitive evaluation of spray models. Simplified models ignoring either interphase slip or turbulent dispersion yielded poor agreement with the measurements [7,8]. In contrast, a stochastic separated flow model of the process, which treated effects of interphase slip and turbulent dispersion performed reasonably well over the new data base, encouraging its extension to liquid sprays.

New measurements in particle-laden jets have also been reported by Elghobashi and his coworkers [9,10]. In contrast to all the other existing measurements, these authors provided some information on initial conditions of their test flows. Results of model evaluation using these measurements are reported in Reference [7].

Existing data on the mean and turbulent structure of nonevaporating sprays is limited. A recent review discusses early work in the field [5]. Subsequently, Alpert and Mathews [11,12] report predictions and measurements for nonevaporating sprays having

¹Numbers in brackets denote references.

configurations encountered in sprinkler systems. Due to the complexity of this geometry and the limited measurements available, however, they suggest that additional measurements and analysis would be desirable. Yule et al. [13] report measurements in nonevaporating sprays from a twin-fluid injector in a coflowing stream. Measurements of particle size were undertaken using a laser tomographic light-scattering technique while mean drop and continuous-phase velocities were measured using laser Doppler anemometry (LDA).

Work done in this laboratory supplemented the measurements of Yule et al. [13] considering the simpler limiting case of a spray in a stagnant environment [1,3]. Mean and fluctuating velocities of the continuous phase were measured, using LDA techniques. Drop sizes were measured using the Fraunhofer diffraction and the slide impaction methods. Liquid fluxes in the spray were found with an isokinetic sampling probe.

The present investigation completes the work done earlier in this laboratory on nonevaporating sprays [1,3], which was limited in its usefulness for model evaluation due to lack of measurements of drop properties and incomplete initial conditions. A multiframe photographic technique was employed in the present investigation to obtain simultaneous measurements of drop size and velocity in the entire spray, as well as initial conditions for the same properties at a position as close to the injector exit as possible. New predictions using typical recent spray models were then compared with the completed spray structure measurements to obtain a more convincing evaluation of the models.

The structure of sprays is generally influenced by turbulent dispersion of the discrete phase. Turbulent dispersion of drops is examined during this investigation by comparing predictions of several theoretical models with the present measurements in nonevaporating sprays. These results are also of interest for modeling evaporating and combusting sprays, however, since the two-phase flow dynamics is well-approximated while avoiding complications due to drop heat and mass transfer and combustion phenomena.

Past models of turbulent particle-laden jets and sprays often consider two limiting cases instead of treating turbulent drop dispersion [5,6]. At one limit the drops and the continuous phase are assumed to have equal rates of turbulent diffusion. The locally homogeneous flow (LHF) approximation provides a consistent formulation of this limit. This implies that interphase transport rates are infinitely fast, so that both phases have the same velocity at each point in the flow. The LHF approximation provides best results for flows containing small drops, where characteristic response times of drops are small in comparison to characteristic times of turbulent fluctuations. LHF models have been extensively evaluated during earlier work in this laboratory, but only yielded accurate predictions for drop sizes smaller than most practical applications [14-16].

Turbulent drop dispersion is neglected entirely at the other limit. This implies that drops follow deterministic trajectories since they only interact with mean properties of the continuous phase, yielding a deterministic separated flow (DSF) model. Such an approximation is appropriate for flows containing large drops, where characteristic drop response times to flow disturbances are large in comparison to characteristic turbulent fluctuation times. Several spray models have been proposed along these lines, e.g., El Banhawy and Whitelaw [17], Mongia and Smith [18], Boyson and Swithenbank [19], and Faeth and coworkers [1,6], among others [5]. Due to the complexities of sprays and uncertainties in initial conditions, however, the value of DSF models has not been clearly established as yet.

Most practical particle-laden flows exhibit properties between these limits and require consideration of turbulent particle dispersion. Early dispersion models, discussed by Yuu et al. [20] apply a gradient diffusion approximation with empirical correlations of turbulent particle exchange coefficients. This approach is not practical, however, since such exchange coefficients are influenced by both particle and turbulence properties--requiring excessive effort to accumulate a data base sufficient for general application of the method.

Several recent studies of turbulent drop dispersion use stochastic separated flow (SSF) methods to circumvent the limitations of the gradient diffusion approach. Stochastic analysis requires an estimate of the mean and turbulent properties of the continuous phase. Drop trajectories are then computed by random sampling to find instantaneous continuous phase properties. Mean and fluctuating drop properties are found by Monte Carlo methods--where a statistically significant number of drop trajectories are averaged to obtain system properties.

SSF models have been applied to particle-laden jets. Yuu et al. [20] use empirical correlations of mean and turbulent properties for SSF analysis of their particle dispersion measurements. Gosman and Ioannides [21] propose a more comprehensive approach, where flow properties for the stochastic calculations are computed with a $k-\epsilon$ turbulence model. This approach has been adopted by the present authors in their study of particle-laden jets and sprays, after only minor modification [1-6].

In the following, the models are described first of all. Experimental methods used for measurements in nonevaporating sprays are then discussed. The report concludes with an evaluation of the models using the spray measurements. Other preliminary reports of the findings of this investigation can be found in Refs. [1,3].

2. THEORY

2.1 Introduction

Three theoretical models of spray processes were considered:

- (1) a locally homogeneous flow (LHF) model, where slip between the

phases is neglected and the flow is assumed to be in local thermodynamic equilibrium; (2) a deterministic separated flow (DSF) model, where slip and finite interphase transport rates are considered but effects of drop dispersion by turbulence and effects of turbulence on interphase transport rates are ignored; and (3) a stochastic separated flow (SSF) model, where effects of interphase slip, turbulent dispersion and turbulent fluctuations are considered using random sampling for turbulence properties in conjunction with random-walk computations for drop motion.

All models employ the widely adopted procedures of k - ϵ - g turbulence models for the gas phase, since this approach has been thoroughly calibrated during earlier work [14-16,22]. Major assumptions for the gas phase are: exchange coefficients of all species and heat are the same, buoyancy only affects the mean flow, and kinetic energy is negligible. Effects of buoyancy are generally small in practical sprays, and neglecting kinetic energy limits the model to low Mach number flows, which is appropriate for the test conditions to be examined as well as for most practical combustion chambers. The assumption of equal exchange coefficients is widely recognized as being acceptable for high Reynolds number turbulent flows typical of spray processes. Other assumptions will be described when introduced since they differ for each model.

In order to ensure adequate numerical closure with reasonable computation costs, the models are limited to boundary-layer flows with no recirculation. The present test flows are axisymmetric with no swirl; therefore, the analysis is posed accordingly. The advantage of these conditions is that they correspond to cases where the turbulence models were developed [22] and have high reliability.

2.2 Locally Homogeneous Flow Model

2.2.1 Governing Equations

The formulation of the LHF model corresponds to the general treatment of the continuous phase for all three models. The basic premise of the LHF model is that the rate of momentum transport between phases is fast in comparison to the rate of development of the flow as a whole. This implies that all phases have the same velocity at each point in the flow.

Past formulations of the LHF model [14-16] use the Reynolds-averaged form of the governing equations. However, the Favre-averaged form of the equations has been proposed as a more formally correct treatment of the physical processes occurring in turbulent variable density and combusting flows [23]. Furthermore, the Favre-averaged form of the governing equations reduces to the Reynolds-averaged form for constant density flows. Jeng and Faeth [24] used the Favre-averaged equations and established a single set of turbulence model constants which satisfactorily predict both constant and variable density jets. Following Jeng and Faeth [24], the Favre-averaged governing equations for the LHF model based on the assumptions discussed in Section 2.1 are written as follows:

$$\frac{\partial}{\partial x} (\overline{\rho u \phi}) + \frac{1}{r} \frac{\partial}{\partial r} (r \overline{\rho v \phi}) = \frac{1}{r} \frac{\partial}{\partial r} (r \mu_{\text{eff}, \phi} \frac{\partial \tilde{\phi}}{\partial r}) + S_{\phi} \quad (2.1)$$

where

$$\tilde{\phi} = \frac{\overline{\rho \phi}}{\bar{\rho}} \quad (2.2)$$

is a Favre-averaged quantity and $\tilde{\phi}$ is a generic quantity. The conservation equations of mass ($\phi = 1$), momentum, mixture fraction, turbulent kinetic energy, rate of dissipation of turbulent kinetic energy and the square of the mixture fraction fluctuations are obtained using Equation (2.1) and the expressions for ϕ , $\mu_{\text{eff}, \phi}$ and S_{ϕ} shown in Table 1 along with the appropriate empirical constants. The empirical constants were established for noncombusting and combusting single-phase flows and are not changed when sprays are considered [14-16, 22, 24].

The turbulent viscosity is calculated from the turbulent kinetic energy and the rate of dissipation as follows:

$$\mu_t = C_{\mu} \bar{\rho} \frac{k^2}{\epsilon} \quad (2.3)$$

2.2.2 State Relationships

Under the LHF approximation, the flow is equivalent to a single-phase flow and effects of the dispersed phase only appear in the representation of thermodynamic properties (temperature, density, enthalpy, etc.) and molecular transport properties (viscosity, thermal conductivity, etc.). The representation of these properties is generally called the state relationships for the flow. Finding state relationships for thermodynamic properties involves conventional adiabatic mixing calculations, with the local state of the mixture specified by the mixture fraction, \tilde{f} , (the fraction of material at a point which originated at the injector).

With equal exchange coefficients, instantaneous properties are only a function of mixture fraction. This allows determination of all scalar properties (temperature, composition and density), as a function of mixture fraction--once and for all [14, 22]. The mass-averaged mean and variance of the flow properties are then found from the mass-averaged probability density function for mixture fraction, $\tilde{P}(f)$ as follows [23, 24]

$$\tilde{\phi} = \frac{\overline{\rho \phi}}{\bar{\rho}} = \int_0^1 \phi(f) \tilde{P}(f) df \quad (2.4)$$

Table 1. Source Terms in Equation (2.1)

ϕ	$\mu_{\text{eff},\phi}$	S_ϕ
1	--	0
\bar{u}	$\mu + \mu_t$	$a (\rho_\infty - \bar{\rho})$
\bar{f}	$(\mu/Sc) + (\mu_t/\sigma_f)$	0
k	$\mu + (\mu_t/\sigma_k)$	$\mu_t \left(\frac{\partial \bar{u}}{\partial r}\right)^2 - \bar{\rho} \epsilon$
ϵ	$\mu + (\mu_t/\sigma_\epsilon)$	$(C_{\epsilon 1} \mu_t \left(\frac{\partial \bar{u}}{\partial r}\right)^2 - C_{\epsilon 2} \bar{\rho} \epsilon)(\epsilon/k)$
g	$(\mu/Sc) + (\mu_t/\sigma_g)$	$C_{g1} \mu_t \left(\frac{\partial \bar{f}}{\partial r}\right)^2 - C_{g2} \bar{\rho} g \epsilon/k$
C_μ	$C_{\epsilon 1}$	C_{g1}
		$C_{\epsilon 2} = C_{g2}$
		σ_k
		σ_ϵ
		$\sigma_f = \sigma_g$
		Sc
0.09	1.44	2.8
		1.87
		1.0
		1.3
		0.7
		0.7

$$\phi''^2 = \frac{\overline{\rho \phi''^2}}{\bar{\rho}} = \int_0^1 (\phi(f) - \bar{\phi})^2 \bar{P}(f) df \quad (2.5)$$

where $\bar{\rho}$ is obtained from

$$\bar{\rho} = \left(\int_0^1 \frac{1}{\rho} \bar{P}(f) df \right)^{-1} \quad (2.6)$$

In Equations (2.4) and (2.5) $\phi(f)$ is known from the state relationships. A functional form must be assumed for $\bar{P}(f)$, although the specific form used has little effect on predictions. $\bar{P}(f)$ depends on the most probable value and the variance of the distribution which can be found from the local values of \bar{f} and g as follows:

$$\bar{f} = \int_0^1 f \bar{P}(f) df \quad (2.7)$$

$$g = \int_0^1 (f - \bar{f})^2 \bar{P}(f) df \quad (2.8)$$

In the present study, state relationships were not needed for the nonevaporating sprays since they were essentially constant-property flows. The mixture density, ρ , is a function only of mixture fraction, f , yielding,

$$\rho^{-1} = f/\rho_o + (1 - f)/\rho_\infty \quad (2.9)$$

Since ρ^{-1} is a linear function of f in the domain $0 \leq f \leq 1$, the mean value of the mixture density ρ , can be found by substituting \bar{f} in Equation (2.9). In this instance, it is not necessary to solve a transport equation for mixture fraction fluctuations and to adopt a probability density function (PDF) for f --which is usually necessary during LHF analysis when heat and mass transfer effects are considered [5,14-16].

2.2.3 Computations

Initial conditions for the calculations are prescribed at the injector exit similar to past work [14-16]. In the absence of other information, all properties are assumed to be constant at the injector exit, aside from a shear layer having a thickness equal to 1% of the injector radius at the passage wall. The constant property portion of the flow is specified as follows:

$$x = 0, r < 0.99d/2; \bar{u}_0 = \dot{M}_0/\dot{m}_0, \bar{f}_0 = 1, k_0 = (0.02\bar{u}_0)^2,$$

$$\epsilon_0 = 2.84 \times 10^{-5} \bar{u}_0^3/d \quad (2.10)$$

The initial variation of \bar{u} and \bar{f} in the shear layer was assumed to be linear. Equation (2.10) provides the inner boundary condition until the shear layer reaches the spray axis after which all gradients at the axis are zero. Initial values of k and ϵ in the shear layer were found by solving their transport equations while neglecting convection and diffusion terms. The ambient values of \bar{u} , \bar{f} , k and ϵ are all zero for the flows considered here.

The calculations were performed using a modified version of GENMIX [25]. The computational grid was similar to past work [14-16]: 33 cross-stream grid nodes; streamwise step sizes limited to 6% of the current flow width or an entrainment increase of 5%--whichever was smaller.

2.3 Deterministic Separated Flow Model

2.3.1 Discrete Phase

The deterministic separated flow model adopts the main features of the LHF model, but only for the gas phase. The liquid phase is treated by solving the Lagrangian equations of motion of the drops and then computing the source terms in the governing equations for the gas phase, resulting from interphase transport processes. This general procedure corresponds to the particle tracking or particle-source-in-cell methods used in most recent two-phase models and is often called a discrete droplet model (DDM) [5,6].

The main assumptions of the drop trajectory calculations for the nonevaporating spray are as follows: heat and mass transfer coupling between the phases is absent by definition; dilute spray with a drag coefficient equivalent to a single solid sphere in an infinite environment; since $\rho_p/\rho > 200$ for conditions treated here, effects of static pressure gradients, virtual mass, Basset and Magnus forces are considered negligible; quasisteady gas phase; negligible drop shattering; negligible collisions; and ambient conditions given by mean-flow properties. The last assumption is characteristic for the deterministic separated flow formulation and will be relaxed for the stochastic separated flow model. The remaining assumptions are common for dilute spray models--their justification is discussed elsewhere [5].

Drops leaving the injector are divided into n groups, defined by the initial position, size, velocity and direction. The subsequent motion of each group is given by

$$\vec{x}_{pi} = \vec{x}_{poi} + \int_0^t \vec{u}_{pi} dt, \quad i = 1, 2, 3 \quad (2.11)^2$$

The mean drop velocity is determined by integrating the equation for conservation of momentum

$$m \frac{d\vec{u}_{pi}}{dt} = - (\pi/8) d_p^2 \bar{\rho} C_D \left| \vec{u}_p - \vec{u} \right| (\vec{u}_{pi} - \vec{u}_i) + a_i, \quad i = 1, 2, 3 \quad (2.12)$$

The standard drag coefficient for solid spheres is employed in the calculations, approximated as follows [5]:

$$C_D = \frac{24}{Re} \left(1 + \frac{Re^{2/3}}{6} \right), \quad Re < 1000$$

$$= 0.44, \quad Re > 1000 \quad (2.13)$$

$$\text{where, } Re = \frac{d_p \left| \vec{u}_p - \vec{u} \right|}{\nu} \quad (2.14)$$

2.3.2 Continuous Phase

This portion of the analysis also utilizes the dilute spray approximation. This implies that the void fraction is unity and that the presence of drops does not contribute directly to the generation or dissipation of turbulence (the latter effect is frequently called turbulence modulation).

The interaction between the liquid and gas phases yields an additional source term S_p on the RHS of Equation (2.1). This term is found by computing the net change of momentum of each drop class i as it passes across a computational cell j .³ The momentum source term per unit cell volume is as follows:

$$\text{Momentum: } S_{pu_j} = \sum_{i=1}^n \dot{n}_i \left((m_i \vec{u}_{pi})_{in} - (m_i \vec{u}_{pi})_{out} \right)_j \quad (2.15)$$

²Since phase densities are constant in these flows, Favre- and time-averages are equivalent for separated flow analysis; therefore, Favre-averages are employed in the following to simplify notation.

³Only one index is needed to define a cell since the calculation is parabolic and each computational cell is defined by its radial position.

where \dot{n}_i is the number of drops per unit time in each class and in and out denote drop conditions entering and leaving the computational cell. This procedure allows for complete momentum coupling between the two phases.

Calculations for the nonevaporating sprays involve addition of only the momentum source term, $S_{p\dot{t}}$ in the gas-phase equations since heat and mass transfer coupling between the two phases could be neglected even when finely atomized--due to low liquid volatility, cf., Table 4. Moreover, the gas-phase density is constant, simplifying Equation (2.1), and a solution for f is no longer needed since drop concentrations are found from the discrete phase solution. The gas-phase equations are solved in the same manner as the LHF model. The only change in this portion of the program involves addition of the new source term given in Equation (2.15). The drop motion equations, Equations (2.11)-(2.14), are solved at the same time, in a stepwise fashion, using a second-order finite difference algorithm.

Computations with the separated flow models were initiated at $x/d = 50$ for all the test sprays, which was the position nearest the injector where adequate spatial resolution was obtained so that profile measurements could provide initial conditions for the calculations. These initial conditions included measurements of mean and fluctuating gas-phase properties, liquid flux, drop size and axial components of the mean and fluctuating drop velocities for both nonevaporating sprays. Initial conditions for ϵ were computed using Equation (2.3) and the measured values of u , k and the Reynolds stress.

Downstream of $x/d = 50$ the void fraction was always greater than 99.1%; therefore, the dilute spray approximation was justified with little error. The computations for the DSF model employed no less than 1200 drop groups.

2.4 Stochastic Separated Flow Model

The DSF model considers only deterministic trajectories for drop groups. The stochastic separated flow model, however, includes effects of turbulent fluctuations on drop dispersion and interphase momentum transport rates by using a technique proposed by Gosman and Ioannides [21].

The stochastic model involves computing the trajectories of a statistically significant sample of individual drops as they move away from the injector and encounter a random distribution of turbulent eddies--utilizing Monte Carlo methods. The key elements of this approach are the methods for specifying the properties of each eddy and the time of interaction of a drop with a particular eddy.

Properties within a particular eddy are assumed to be uniform, but properties change in a random fashion from eddy to eddy. The trajectory calculation is the same as the DSF model, involving solution of Equations (2.11)-(2.14); however, mean-gas properties in these equations are replaced by the instantaneous properties of each eddy.

7 The properties of each eddy were found at the start of drop/eddy interaction by making a random selection from the probability density function (PDF) of velocity. Velocity fluctuations were assumed to be isotropic with a Gaussian PDF having a standard deviation of $(2k/3)^{1/2}$ and mean components $u, v, 0$. The cumulative distribution function for each velocity component was constructed and sampled. This involved randomly selecting three numbers in the range 0-1 and computing the velocity components for these three values of the cumulative distribution function.

A drop was assumed to interact with an eddy for a time which was decided from either the eddy lifetime or the characteristic size of an eddy [21,4]. The characteristic size of an eddy was taken to be the dissipation length scale.

$$L_e = C_\mu^{3/4} K^{3/2} / \epsilon \quad (2.16)$$

The eddy lifetime was computed from the following:

$$t_e = L_e / (2k/3)^{1/2} \quad (2.17)$$

Drops were assumed to interact with an eddy as long as the time of interaction, Δt , and the distance of interaction $|\Delta \vec{x}_p|$, satisfied the following criteria:

$$\Delta t \leq t_e, \quad |\Delta \vec{x}_p| \leq L_e \quad (2.18)$$

Drop capture by an eddy corresponds to ending the interaction with the first criterion while a drop traverses an eddy when the interaction is ended with the second criterion.

The remaining computations are similar to the DSF model, except that the source term of Equation (2.15) is computed for the random-walk trajectories of the drops--as opposed to the deterministic solution. Also, more drop trajectories must be considered to obtain statistically significant drop properties (generally 4000-6000 trajectories were used). A by-product of the additional calculations, however, is that the SSF model yields both mean and fluctuating drop properties. This provides an additional test of model performance.

3. EXPERIMENTAL METHODS

3.1 Introduction

The experimental apparatus provided convenient optical and probe access to the flow. The injector and the fluid delivery system allowed selection of fine and coarse sprays and assured long-term repeatability of the test spray conditions.

The following flows were examined during the present study:

1. An isothermal air jet--to check experimental techniques.
2. Two nonevaporating sprays (with Sauter mean diameters of 30 and 87 μm).

Nonintrusive instrumentation included the laser-Doppler anemometer, Fraunhofer diffraction and multiframe photography. Other measurements involved probes such as an isokinetic sampling probe and a slide impactor.

3.2 Test Apparatus

The requirement for a flow configuration having no zones of recirculation, a simple geometry and well-defined boundary conditions is met with the apparatus illustrated in Figure 1. The injector was mounted on a two-dimensional traversing mechanism at the center of a cage assembly (1 m square by 2.5 m high). For all the test flows, injection was vertically downward into stagnant room air. The flow was protected from room disturbances using 16-mesh screens all around the cage. Major traversing, to obtain radial profiles of flow quantities, involved moving the entire cage assembly, which was mounted on a bearing track. This approach keeps the flow nearly concentric with the vertical axis of the cage, which minimizes disturbance of the axisymmetric flow due to off-center screen positions, and also allows optical instrumentation to be mounted on a rigid base. Unislide arrangements were used to position the injector relative to the measurement location.

A plenum chamber with an exhaust system was included at the bottom of the cage. The inlet to the plenum chamber is screened and is 1 m below the plane of instrumentation. The screened inlet provides uniform suction thus keeping the flow axisymmetric. The only purpose of the exhaust system was to prevent the smallest drops from recirculating and its operation did not introduce a coflow of any significance. Testing showed that the disturbance levels were less than 1% at the measurement location.

Measurements from this arrangement should be attractive for those wishing to evaluate models. The flow is analogous to a jet in stagnant surroundings, yielding a parabolic (boundary layer) flow. The turbulence characteristics of such a flow can be modeled more reliably than flows with recirculation. Naturally, boundary layer flows greatly simplify problems of obtaining accurate numerical solutions, releasing computer time for use in the two-phase portion of the problem. The absence of coflow eliminates problems of flow separation on bulky injector elements. Boundary conditions are well-defined, since there are no uncertainties regarding wall friction and heat losses and inlet flow properties which are encountered in enclosed chambers.

The flow system of the injector is illustrated in Figure 2. A Spraying Systems Company air atomizing injector (model 1/4 J2050 fluid nozzle and 67147 air nozzle with outlet diameter of 1.194 mm) was used

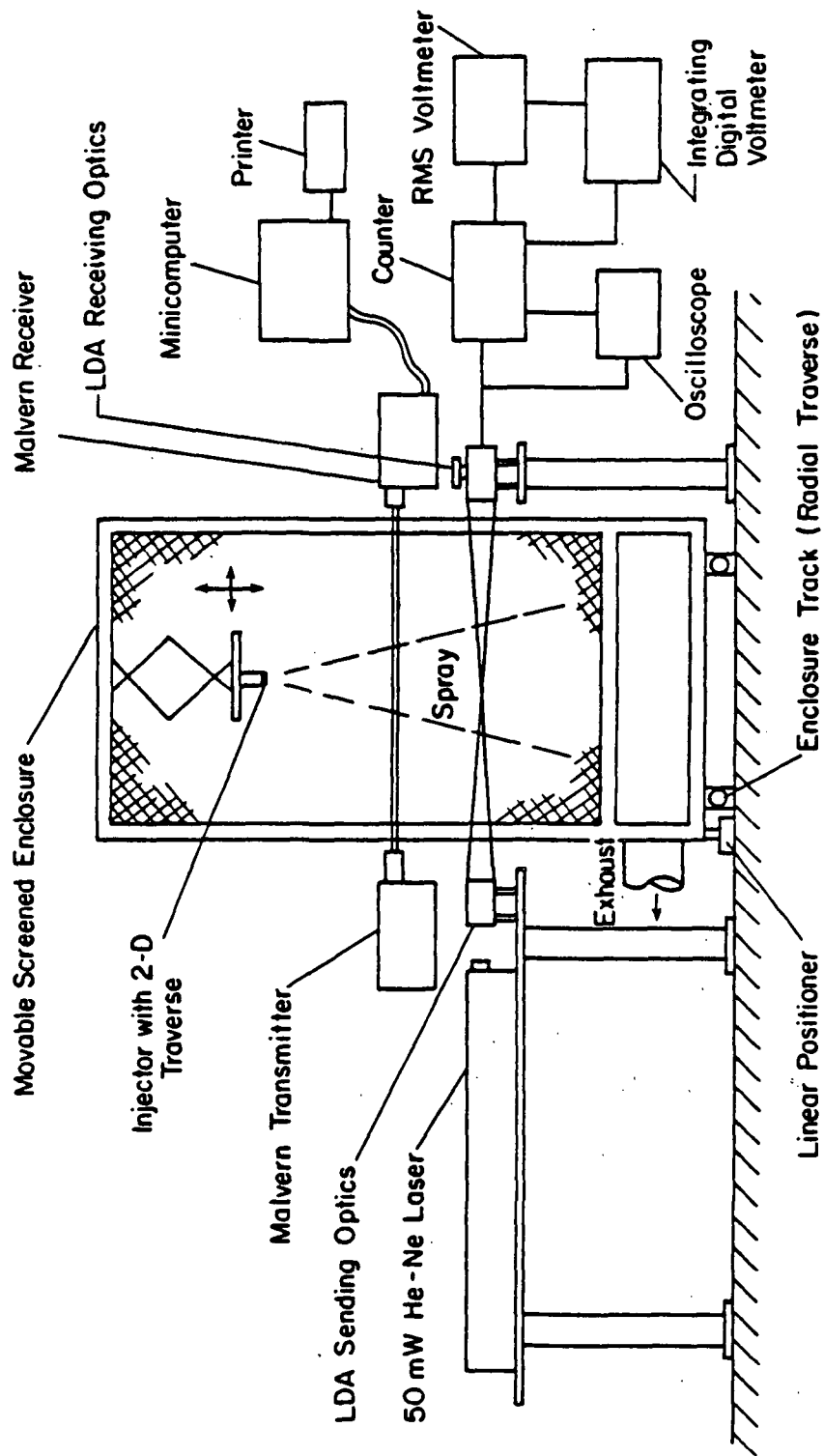


Figure 1. Sketch of the experimental apparatus.

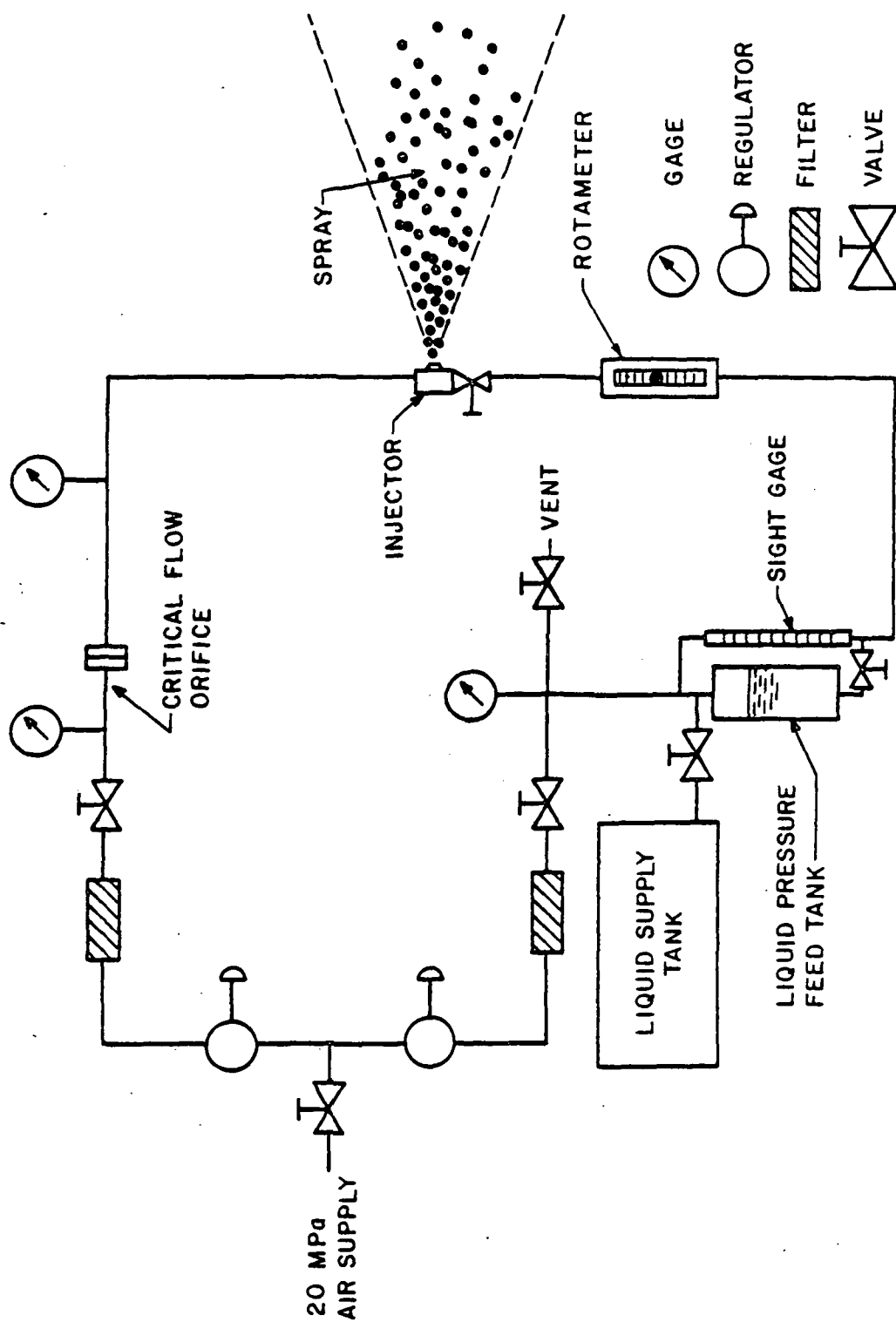


Figure 2. Sketch of the injector flow system.

for all the spray tests. The injector delivers a full-cone spray with no swirl. This injector is identical to that used by Faeth and coworkers [14,15].

The air flow to the injector is controlled with a pressure regulator and metered with a critical flow orifice to ensure long-term stable operation. The pressure regulator was a Matheson model 4 regulator with a 0-21 MPa output capacity. The pressure upstream of the critical-flow orifice was measured with a Hiese absolute pressure gauge with a 0-2.1 MPa capacity. The pressure gauge was calibrated with a dead-weight tester and the orifice was calibrated with a Precision Scientific Company wet-test meter (0.283 liters/rev.).

The liquid was stored in a tank under pressure, however, the tank was not agitated and pressure levels were moderate (0.3-0.8 MPa). Therefore, the dissolved air content of the spray liquids was negligible. The liquid flow is controlled with a valve and metered with a rotameter. A Fisher Porter rotameter tube no. 2A-25-A was used for the nonevaporating spray liquid and was calibrated by direct collection of liquid in a measuring flask.

The spray liquid must be a well-defined material in order to facilitate use of the measurements by others. Vacuum pump oil, supplied by Sargent-Welch Scientific Company, was used for tests of nonevaporating sprays, due to its low vapor pressure. Finally, in order to maintain repeatable flow and atomization conditions the entire test cell was heated to above-normal temperatures--to $27 \pm 1^\circ\text{C}$.

3.3 Measurement Techniques and Instrumentation

3.3.1 Gas-Phase Velocity Measurements

Table 2 is a summary of the flow structure measurements made and the techniques employed for each measurement.

Mean and fluctuating gas velocities were measured using a dual-beam, single-channel, frequency-shifted laser-Doppler anemometer (LDA). An equipment list for the LDA system appears in Table 3. The sending and receiving optics had a focal length of 242 mm with a 11.61° angle between beams. A 200 mm focal length lens was used to focus the scattered light onto a photomultiplier. The aperture diameter of the photomultiplier was 0.25 mm. The receiving lens was masked with a beam-stop which provided a collection aperture having a diameter of 25 mm. The above optical configuration produced a measuring volume 0.470 mm in length and 0.098 mm in diameter, with a fringe spacing of $3.128 \mu\text{m}$.

Seeding particles for operation of the LDA were provided in two ways. In the two-phase region, the smallest drops provided adequate seeding, while erroneous signals from large drops were eliminated by setting a low signal amplitude limit on the counter data processor, since large drops yield large pedestal signals. This natural source was supplemented by seeding the surroundings of the spray using oil

Table 2. Summary of Instrumentation for Spray Structure Measurements

Measurement	Technique	Equipment
Mean and fluctuating gas velocities.	Dual-beam, forward scatter laser-Doppler anemometer, frequency shifted with tracker and burst counter data processing.	Spectra Physics Model 125A (50 mW) He Ne laser, rest TSI, Inc.
Drop size and velocity.	Double-flash shadow photography.	In-house design.
Drop size distributions.	a) Fraunhofer diffraction (monitoring purposes). b) Slide impaction. c) Photography.	Malvern model 2200 particle sizer. In-house design. In-house design.
Liquid flux.	Isokinetic sampling and inertial separation.	In-house design.

Table 3. LDA Equipment List

Component	Manufacturer	Model
Helium-Neon Laser	Spectra Physics	125A
Integrated Optics	Thermo-Systems	900
Frequency Shifter	Thermo-Systems	9180
Photodetector	Thermo-Systems	960
Frequency Tracker	Thermo-Systems	1090
Burst Counter	Thermo-Systems	1980
RMS Voltmeter	Thermo-Systems	1060
Dual-Beam Oscilloscope	Thermo-Systems	561A
Integrating Digital Voltmeter	Hewlett-Packard	240IC

particles which are present suspended in the exhaust of a vacuum pump. The average diameter of the particles was $0.6 \mu\text{m}$ at a concentration of 2.8×10^{10} particles/ m^3 . Photographic measurements showed that the maximum concentration of spray drops was about 5.0×10^8 drops/ m^3 at $x/d = 40$ in the 30 SMD nonevaporating spray. The concentration of spray drops was over two orders of magnitude less than the concentration of the seeding particles in other downstream positions of the test sprays. Therefore, gas velocities were primarily measured, with a small bias due to spray drops. The seeding techniques provided a relatively high signal rate so that concentration biasing was eliminated by using time averages. This procedure also involved adjusting external seeding until intermittency was no longer observed on the oscilloscope trace of the LDA detector output.

Mean and fluctuating velocity components of the gas phase were measured at various axial and radial locations in both the test sprays. An integration period of one minute or more was used to determine the mean quantities. Radial profiles were obtained in a single traverse across the spray and components of mean and fluctuating velocities were recorded by employing different beam orientations at each radial location. Measurements of the tangential component of the fluctuating velocity $(\bar{w}^2)^{1/2}$ was made with a separate traverse in the third direction. The use of several beam orientations allowed measurement of Reynolds stress. Reynolds stress measurements are valuable for checking model predictions and for locating the flow centerline (since Reynolds stress is zero at the centerline and doesn't exhibit the broad maxima encountered for other variables). The above measurements were found to be repeatable within 5%.

3.3.2 Liquid-Phase Properties

3.3.2.1 Drop Size Measurement

Three methods were used to determine the drop size distributions and Sauter mean diameters (SMD) at various locations in the test sprays. The first method involved use of a Malvern particle size analyzer, model 2200, which operates on the principle of Fraunhofer diffraction of laser light scattered by drops. The data was reduced using a model-independent code and then processed to compute the SMD. The measuring region included the entire spray width (input laser beam diameter of 9 mm centered at $x/d = 12.6$). Since this technique provides a line-of-sight measurement over an irregular region of the spray, it was only used to monitor injector performance.

The second method used for drop size measurements involved inertial impaction [14]. A sketch of the slide impactor is shown in Figure 3. Small glass slides coated with a layer of magnesium oxide are momentarily exposed to the flow using a pneumatically driven shutter. Drops leave a crater in the coating, which can be related to the initial drop size [14]. The slides are then viewed under a microscope and each drop impression is sized and counted. Typically, 2000 drops were counted at each measurement location to obtain statistically reliable results. The collection efficiency of the shutter mechanism was calculated for a range of droplet sizes for a

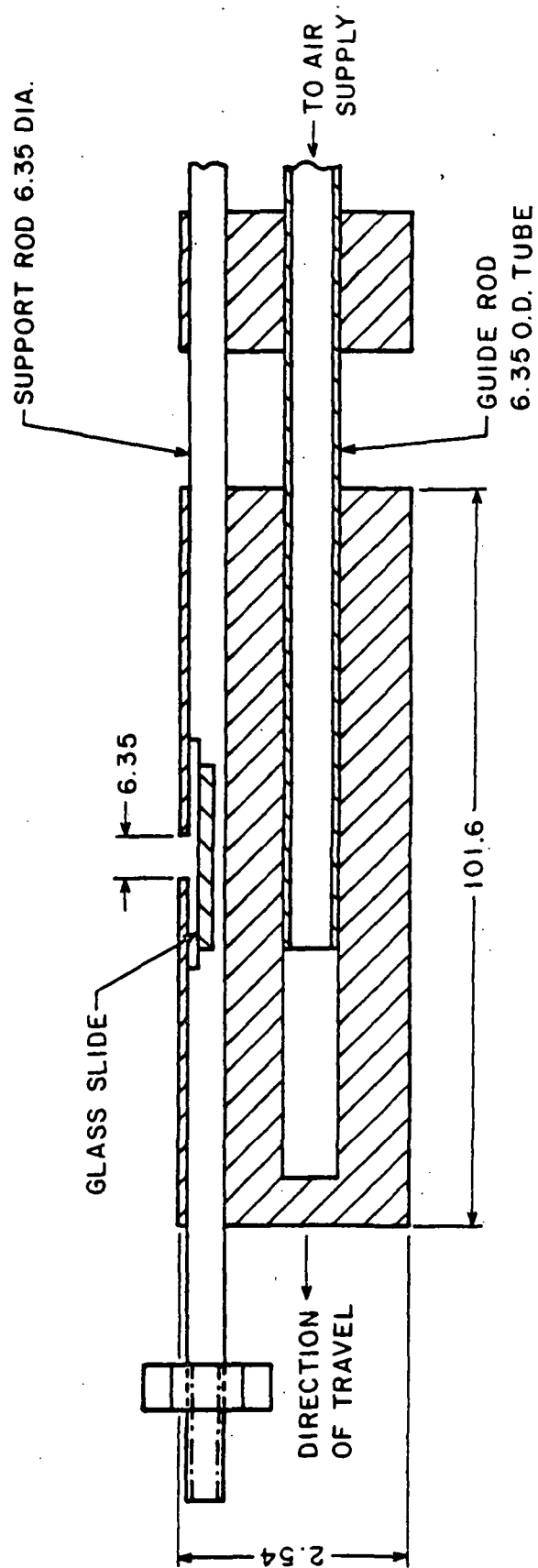


Figure 3. Sketch of the droplet impactor.

given gas velocity [14]. This was then used to correct the number of droplets actually collected. The SMD at each location was calculated directly from the drop size distributions. The size distribution data obtained by this slide impaction method can be classified as being temporal, as opposed to spatial, since the method of observation more closely approximates the flow of drops through a fixed area during intervals of time. The drop size distribution and the SMD are therefore proportional to flux density, i.e., number/(unit area x unit time).

Finally, an imaging technique viz., double-flash photography which was primarily used for simultaneous measurements of drop size and velocity also yielded drop size distributions. A description of the imaging technique is given in the next section.

3.3.2.2 Drop Size and Velocity Correlation Measurement

The optical system used for the double-flash shadow photograph technique for drop size and velocity measurements is shown in Figure 4. The arrangement consists of two submicrosecond flash sources, a lens system to focus the light and a camera, all arranged on the same optical axis [26]. The flashes are fired consecutively, at electronically controlled times, so that two images of each of the moving droplets are obtained on the same photographic negative. Subsequent magnification of the negative, measurement of the size and distance traveled by the droplet, as well as knowledge of the time interval between the flashes yields the size and velocity of the droplets. The resolution of the present technique allowed measurement of only the axial drop velocity component with sufficient accuracy. A typical double-flash shadow photograph is shown in Figure 5.

A General Radio type 1538-A Strobotac and type 1539-A Stroboslave were used as the first and second flash sources, respectively, cf., Figure 4. They produced flashes having durations of 0.5 μ s and 0.8 μ s, respectively, and effectively stopped the motion of the droplets. The first flash was located at the focal point of lens 1 so that a parallel beam illuminated the field of view, yielding the sharpest shadow image. The second flash was arranged so that the light was focused onto the point of origin of the first flash. Since the second flash was of longer duration, it produced a darker image than the first--providing a means for identifying flow reversals.

The strobe units were triggered consecutively by means of a specially-designed pulse generator. The generator delivered pulses that met the input specifications of the strobe units and was also equipped with a variable time delay circuit so that the time interval between the pulses could be selected in the range 0.1-1000 μ s. These pulses were recorded, as well, with a two-channel Nicolet Explorer III digital oscilloscope, model 204-A, so that the time interval could be measured within 0.05 μ s. Typical intervals used for the present test conditions ranged from 2-80 μ s.

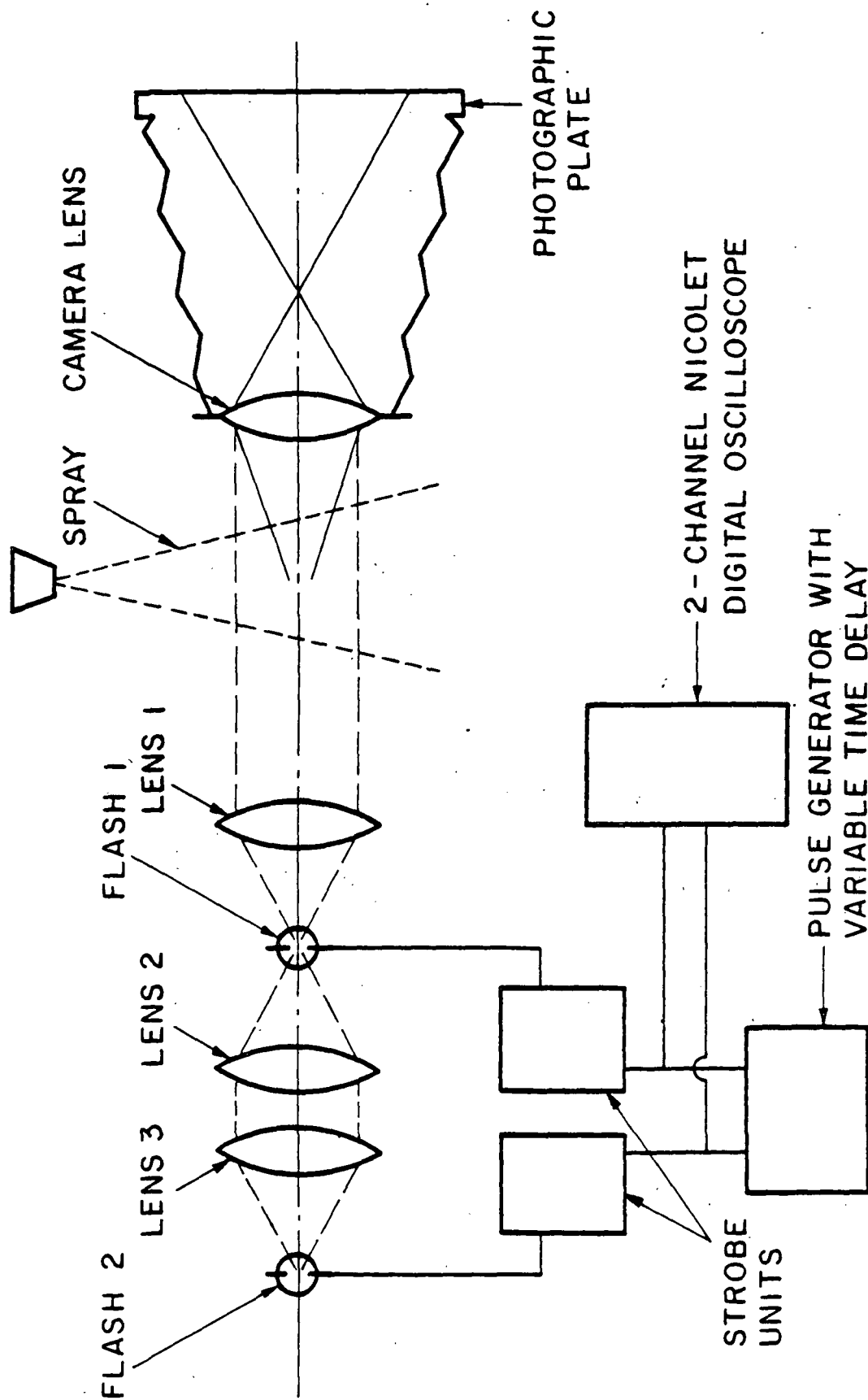


Figure 4. Sketch of the double-flash shadow photography system.

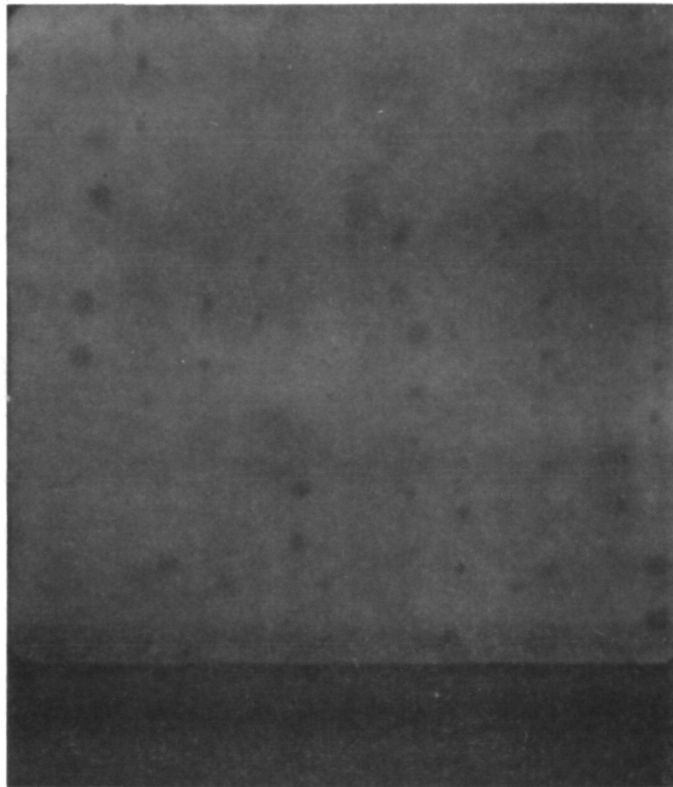


Figure 5. A typical double-flash shadow photograph.

Various configurations of camera lenses, film and data reduction methods were used in different regions of the sprays. Obtaining initial conditions of drop size and velocity required good spatial resolution in relatively dense regions of the sprays. In these regions a Graphlex Optar, $f/4-7$, 135 mm focal length lens, in conjunction with a rectangular magnifier lens (27 mm x 40 mm, 60 mm focal length), was used as the imaging lens system. A Graphlex 4 x 5 still camera was located at the end of an extension tunnel to give a primary magnification of 38:1. The resulting rectangular area of the spray viewed (2.34 mm x 2.29 mm) provided satisfactory spatial resolution at $x/d = 50$. Polaroid type 57 film (3000 ASA) was used with this setup and measurements of drop diameter and interimage distances were made by further magnification under a calibrated microscope.

In the dilute regions of the sprays ($x/d \geq 100$) the primary magnification was reduced to 6:1 and Agfa pan Vario-XL Professional 35 mm film (50-1600 ASA) was used. The negatives were projected on a screen at greatly increased magnifications to make measurements of size and distance between images. The spray area viewed with this arrangement was 5.7 mm x 8.0 mm.

The magnification associated with each optical arrangement was determined from photographs of a reticle, manufactured by Edmund Scientific Company. The depth of field in which droplets appear to be in focus in the optical sampling volume increases with increasing drop size. This behavior results in an underestimation of the relative number of small drops since they are counted over a smaller effective sampling volume. The depth of field associated with each optical arrangement varied between 0.1-3.0 mm, and bias corrections were applied to all photographic measurements of drop size distributions in the present study according to Appendix B.

The size distribution data obtained by this imaging method can be classified as a spatial measurement, unlike the data obtained by slide impaction. The drop size distribution and SMD are therefore proportional to concentration, i.e., number/unit volume.

The overall accuracy of the present method for velocity measurements was estimated to be $\pm 10\%$. The uncertainty associated with size was on the order of $\pm 10\%$ for drops having diameters greater than 25 μm . This uncertainty increased to $\pm 25\%$ for drops whose diameters were smaller than 25 μm . The minimum drop size measurable within the above limits of error was 10 μm . Approximately 600 to 800 drops were counted at each measurement location to obtain drop size and velocity distributions, which were processed to find mean and fluctuating axial velocities and the SMD. Since the number frequency of the large drops ($> 60 \mu\text{m}$ and $> 120 \mu\text{m}$ for the case 1 and case 2 sprays, respectively) at any given measurement location was relatively low, measurements of fluctuating velocities for the large drops are only qualitative. The SMD data obtained by this imaging method and the slide impaction method agreed within 15%, suggesting only moderate effects of velocity bias (spatial or temporal sampling) for present measurements.

3.3.2.3 Liquid Flux Measurement

Liquid flux measurements for the nonevaporating sprays employed isokinetic sampling. The collection probe, shown in Figure 6, is a modified version of the particle collection probe used by Szekely and Faeth [27]. The tip of the probe had an ID of 3 mm and provided sufficient spatial resolution at $x/d = 50$. The suction end of the probe was connected to the inlet of a vacuum pump via a rotameter. Isokinetic conditions were maintained by adjusting the suction flow rate so that the velocity at the probe inlet matched the local gas velocity determined from the LDA velocity measurements.

The nonevaporating liquid was collected on a composite which consisted of layers of No. 2 Whatman filter paper, gauze and cotton. Samples were weighed before and after collection of liquid on a Christian Becker balance, model AB-4, which had a sensitivity of 1 milligram. Sampling times varied from 1 minute to 10 minutes--depending on the location in the spray. The design of the probe allowed minimum loss of the liquid on the probe inlet and walls. The liquid flux data, integrated over the cross-section of the spray at each axial position, was checked against the injector liquid mass flow rate to determine the collection efficiency of the technique. These collection efficiencies at various axial locations in the case 1 and case 2 sprays are listed in Appendix B.2 and C.2, respectively.

3.3.3 Jet Momentum Measurement

The momentum of each of the test sprays was determined by measuring the axial force of an impingement plate held near the exit of the nozzle (95 mm diameter plate, 25 mm from the nozzle). A Unimeasure 80 force transducer was used to measure the force. The transducer was calibrated by placing known weights on the plate. The exit velocity of the two-phase spray was then calculated from the jet momentum and the mass flow rate. This calculation assumes locally homogeneous flow, and serves as initial conditions for the LHF spray model.

3.4 Experimental Conditions

The test conditions for the two nonevaporating sprays are summarized in Table 4. Case 1 is a finer spray than case 2. The selection of these cases was accomplished by measuring the nominal SMD with the Malvern particle size analyzer. Also shown in Table 4 are the experimental conditions for an air jet test which was used to check experimental techniques.

The loading ratio of each of the sprays was selected to be within the range of most practical liquid-fuel injection systems. Axial and radial profiles of various flow quantities in the sprays were measured using the techniques discussed earlier to obtain a detailed knowledge of the spray structure. In addition, initial conditions of flow

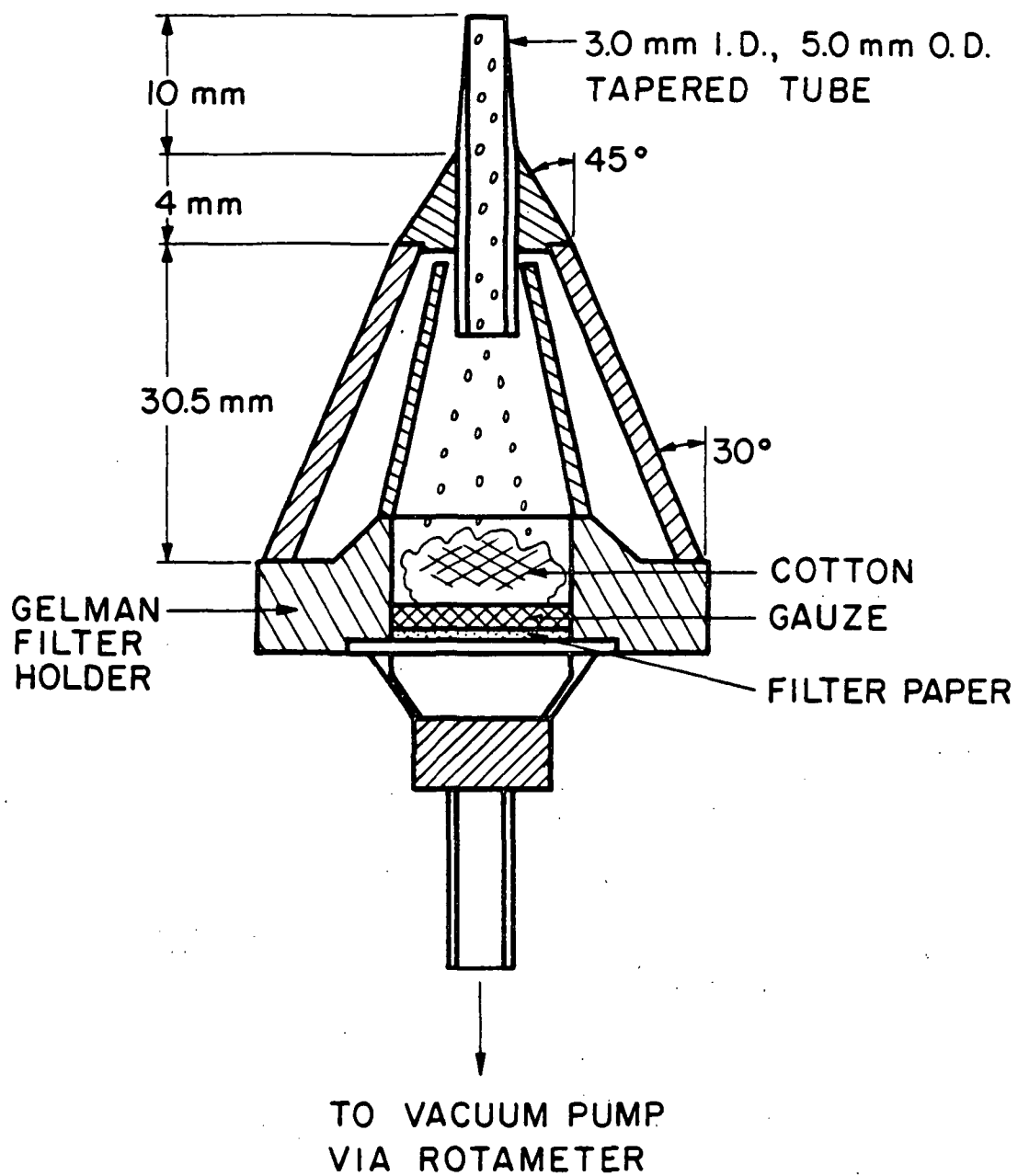


Figure 6. Sketch of the sampling probe for liquid flux measurements.

Table 4. Summary of Test Conditions for the Air-Jet and Nonevaporating Sprays

	Air Jet	Sprays	
		Case 1	Case 2
Injected fluid	air	air and oil ^b	air and oil ^b
Injector flow rates, mg/s			
Gas	338	338	216
Liquid	0	600	1400
Loading ratio ^c	0	1.78	6.48
Jet momentum, mN	120.1	137.2	70.1
Initial velocity, m/s ^d	175	146	43.4
Reynolds number ^d	2.6×10^4	3.0×10^4	2.4×10^4
SMD, μm^e	0	30	87
Spray angle ^f	--	30	33

^aAll flows employ Spraying Systems air-atomizing injector (model 1/4J2050 nozzle, No. 67147 air nozzle, 1.194 mm injector exit diameter). Ambient and injector inlet temperature 300 ± 1 K, ambient pressure, 97 kPa.

^bSargent-Welch Scientific Company, Duo Seal Oil Catalog No. 1407K25, density = 878 kg/m^3 , vapor pressure at 38°C = 4×10^{-4} mm Hg.

^cRatio of injected liquid to gas flow rates.

^dAssuming LHF. The viscosity of air was employed for the Reynolds number.

^eMeasured with the Malvern, model 2200 particle sizer at $x/d = 12.6$.

^fDetermined from liquid flux measurements at $x/d = 50$.

quantities were measured so that predictions of the various spray models could be compared with the present measurements.

4. RESULTS AND DISCUSSION

4.1 Introduction

The major objective of the present study was to complete systematic and comprehensive measurements in sprays. The experiments were planned so that the complexities found in practical sprays were introduced one at a time. Initial and boundary conditions were well established for the flows--to help in the development of reliable models of spray processes. In the following sections the experimental findings concerning the structure of the air jet and the two nonevaporating sprays, cf., Table 4 for operating conditions, will be presented. In addition, the comparison of measurements and the predictions of the three theoretical models of spray processes (LHF, DSF and SSF, cf., Section 2) will be discussed.

4.2 Air-Jet Calibration

The measurements of mean and fluctuating velocities in the air jet were in good agreement with earlier measurements by Shearer et al. [14] using a similar twin-fluid injector. The comparison between predictions and measurements was also satisfactory--similar to Ref. [14]. This established an acceptable baseline for measurements in the sprays and these results will not be considered any further here.

4.3 Initial Conditions

4.3.1 Jet Momentum, Spray Angle and Gas-Phase Properties

Due to its small size, measurements at the exit of the injector were limited to mass flow rate and momentum of the two-phase jet. The latter measurements was completed using an impact plate, similar to Ref. [14].

Photographs of the two sprays appear in Figures 7 and 8. Determination of spray angles from photographs is a subjective matter which is also influenced by the lighting, film and exposure of the film. The values found from present photographs for case 1 and 2 sprays are 24° and 21° . These values are less than the angles found from the liquid flux measurements--which provide far greater sensitivity for determining the presence of liquid.

Due to limitations of spatial resolution, profiles of spray properties were only measured at $x/d \geq 50$. In particular, detailed measurements of mean and fluctuating gas velocities, Reynolds stresses and kinetic energy of the gas phase were undertaken at $x/d = 50$, in order to define initial conditions for the SF computations. These measurements will be illustrated later, when all gas-phase properties are discussed.

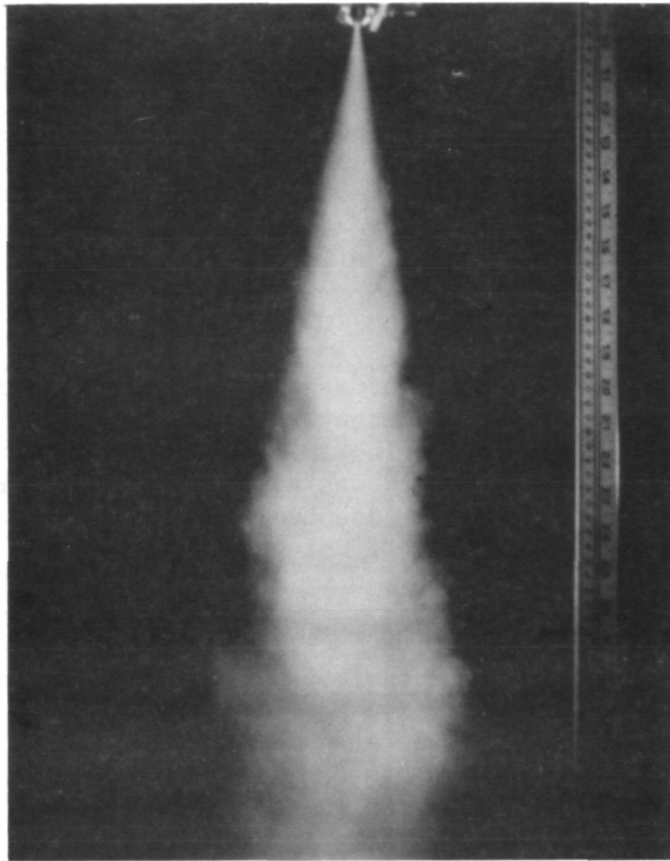


Figure 7. Photograph of the case 1 nonevaporating spray.

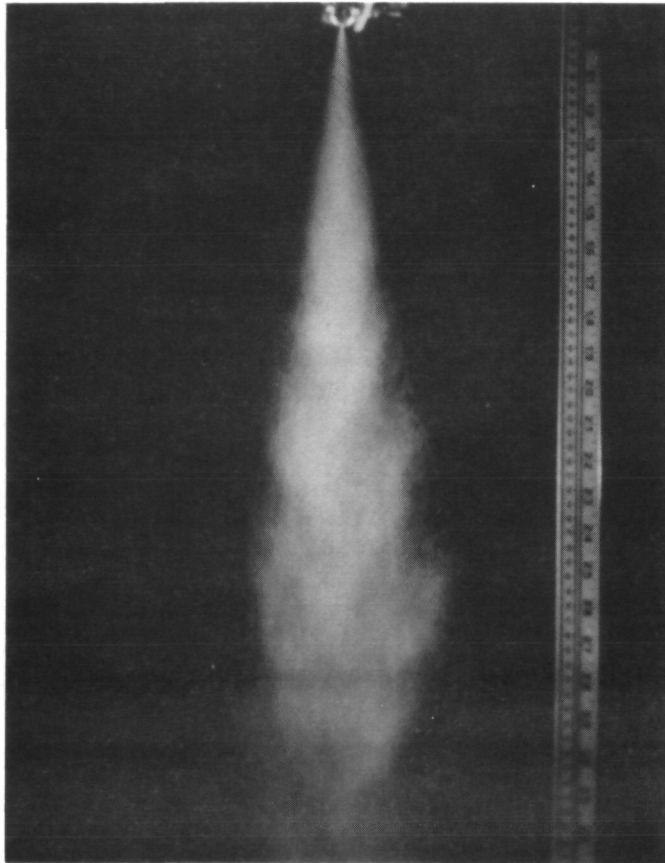


Figure 8. Photograph of the case 2 nonevaporating spray.

4.3.2 Liquid-Phase Properties

Detailed measurements of liquid flux, drop-size distributions and mean and fluctuating drop velocities were also undertaken at $x/d = 50$ for the two nonevaporating sprays. Liquid flux measurements were completed by isokinetic sampling and were interpolated to obtain initial conditions for the SF calculations.

As stated earlier, two techniques were used to measure drop-size distributions at $x/d = 50$. Drop-size distributions for various radial positions at $x/d = 50$ for the case 1 and case 2 sprays using the slide impaction technique are illustrated in Figure 9. The same measurements using the double-flash photographic technique are shown in Figure 10. Figure 11 is an illustration of the radial distribution of SMD across the sprays as calculated from the drop-size distribution data using both techniques. The above results for the case 2 (87 μm SMD) spray, which needed special attention, will be discussed after the case 1 (30 μm SMD) spray.

For the case 1 spray, although the distributions obtained by slide impaction differ in detail at the various radial locations, the SMD is relatively uniform across the spray, cf., Figure 11. The values of the SMD at this axial station are larger than the nominal size obtained by the Fraunhofer diffraction measurements, since: (1) this position is farther from the injector which allows drop sizes to increase by collisions and coalescence in the dense portion of the spray; (2) the slide impactor has reduced collection efficiencies for small drops [14], which tends to bias its measurement toward larger drop sizes even after correction; and (3) the slide impactor is more effective for finding occasional large drops than the Fraunhofer diffraction method, which also tends to increase the SMD measured by impaction.

The gross properties of the drop-size distributions as measured by the slide impaction and photographic techniques, cf., Figures 9 and 10, for the case 1 spray are quite similar, noting that the size ranges used with each technique are dissimilar and the fact that drops having diameters $< 15 \mu\text{m}$ were not measured by the photographic technique. Moreover, the radial distribution of SMD for the case 1 spray (Figure 11) as measured by the two techniques are in quite good agreement, which may not be considered entirely fortuitous, since the SMD is little affected by the small drops in the distribution. The above observation of the good agreement between the two techniques for drop-size measurement alleviates the concern that the sample sizes used for the photographic measurements were relatively small. Even so, for the case 1 spray the slide impaction data was preferred over the photographic measurements of drop-size distributions (in order to avoid velocity bias) to define initial conditions for the SF model computations.

Initial conditions of drop-size distributions for the case 2 spray had to be handled in a slightly different manner. This was due to the presence of ligaments detected at $x/d = 50$ during the course of photographic measurements of drop size and velocity. Figure 12 is a typical double-flash photograph which shows the presence of a ligament.

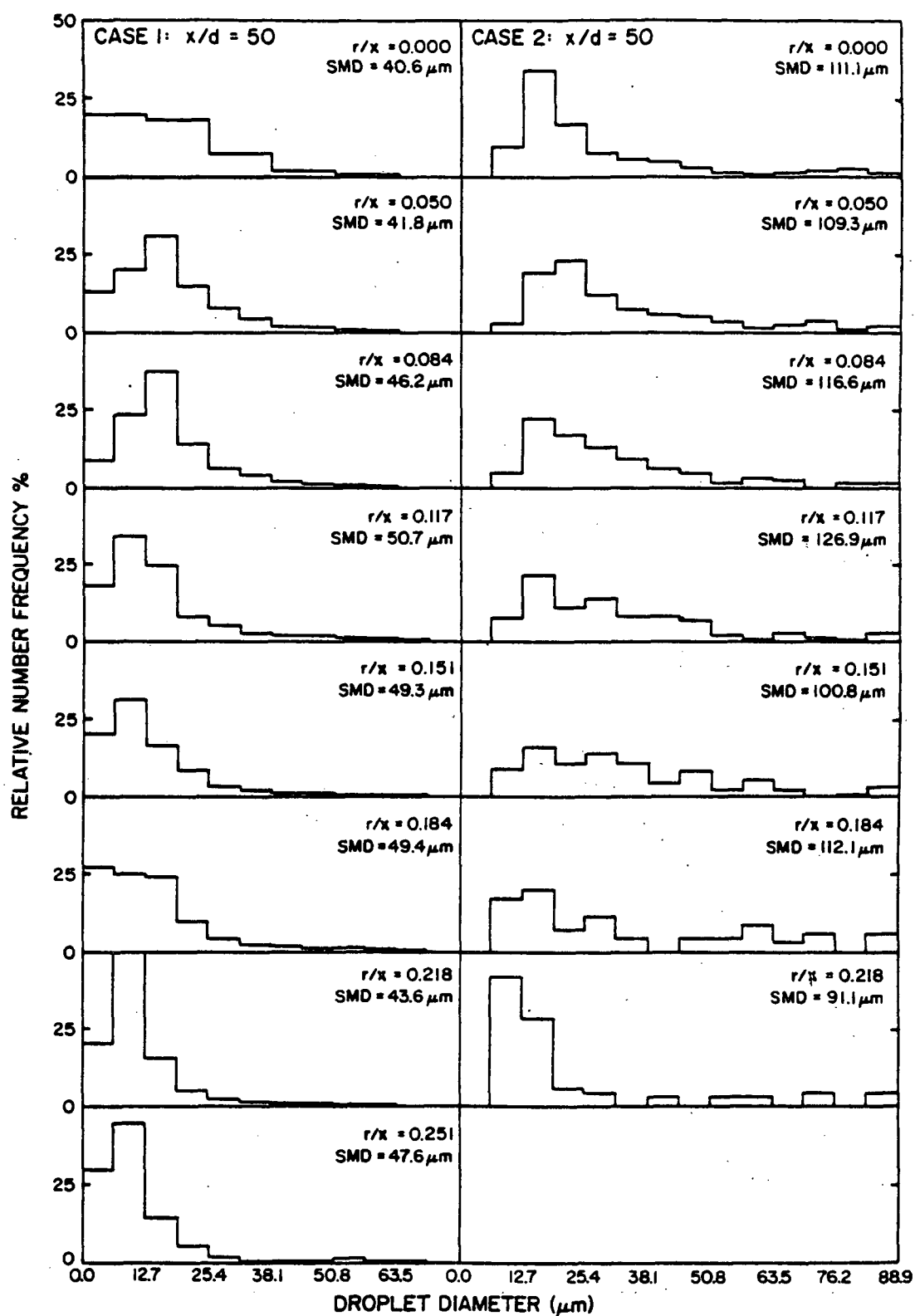


Figure 9. Drop-size distributions for the nonevaporating sprays at $x/d = 50$ (slide impaction results).

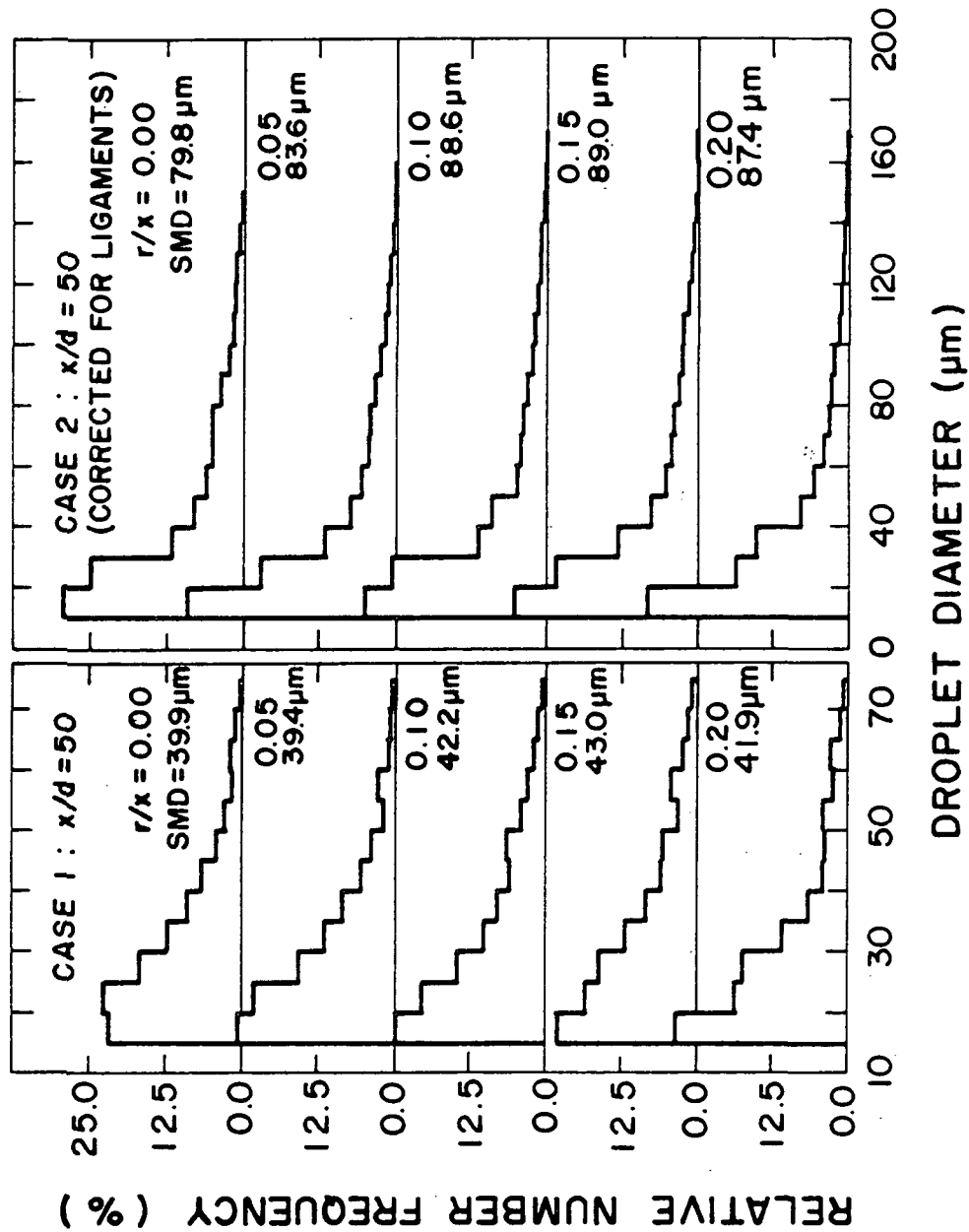


Figure 10. Drop-size distributions for the nonevaporating sprays at $x/d = 50$ (photographic results).

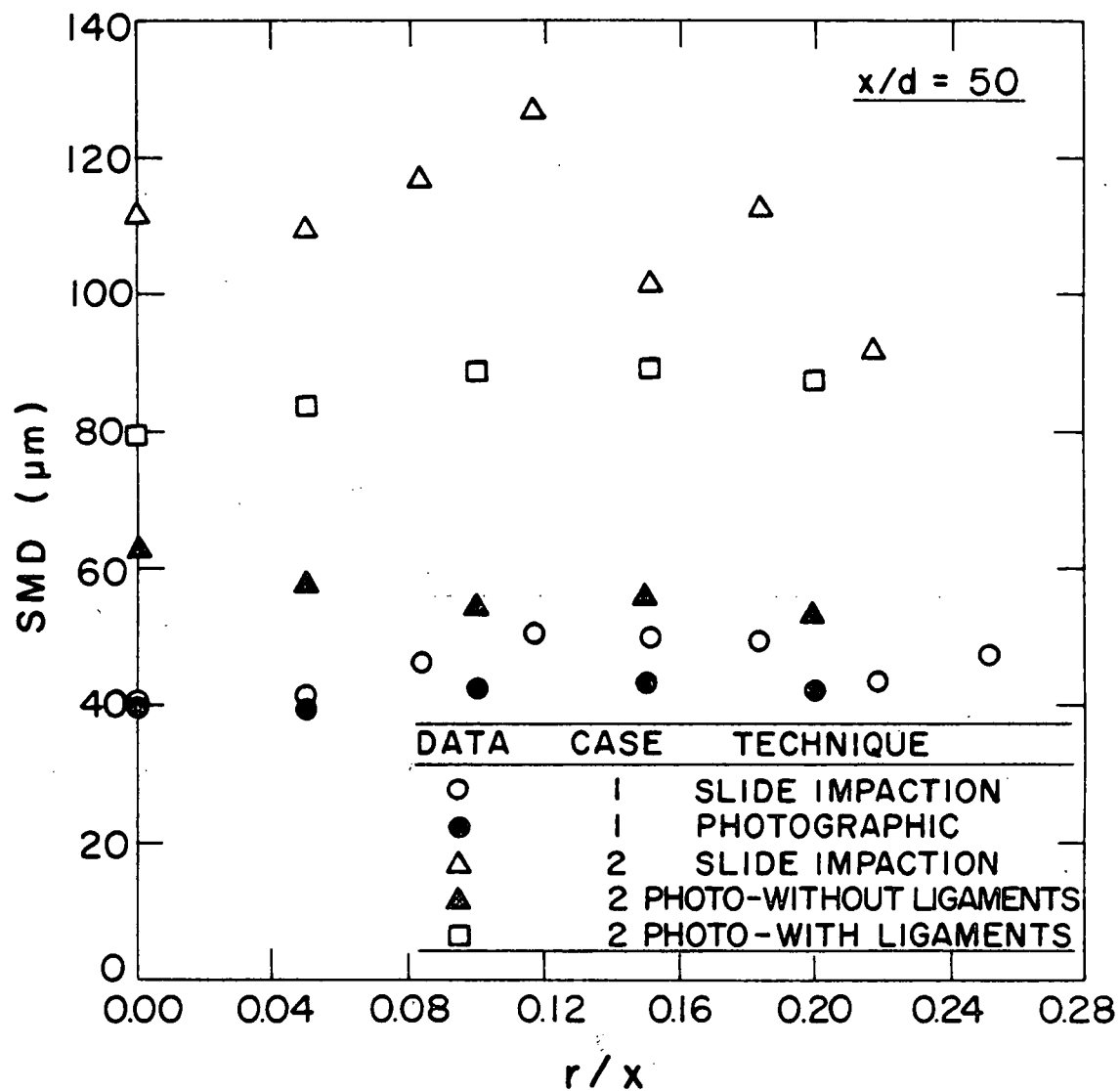


Figure 11. Radial variation of SMD in the nonevaporating sprays at $x/d = 50$.

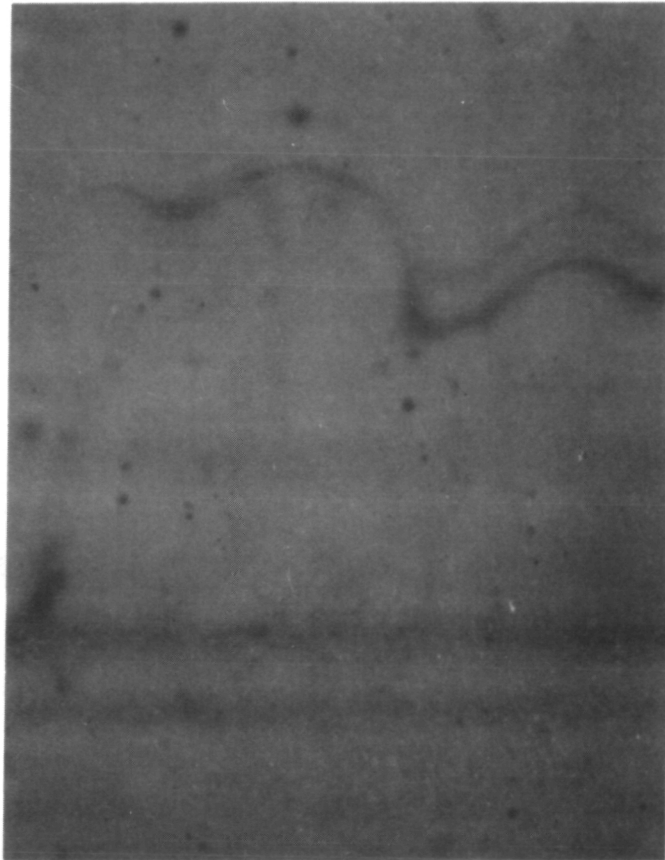


Figure 12. Double-flash shadow photograph at $x/d = 50$ in the case 2 nonevaporating spray showing presence of ligaments.

The formation of ligaments is a well-known intermediate stage in the atomization process of high-viscosity fluids by air-blast injectors [28]. Single-flash photographs of conditions at the injector exit for both the case 1 and case 2 sprays, cf., Figure 13 and 14, respectively, show the formation of ligaments and the subsequent breakdown of these ligaments into stable drops. For the case 1 spray, which had a lower loading ratio (higher air to liquid mass flow rate ratio), the ligament-breakup process was completed by $x/d = 50$, whereas the process took longer in the case 2, higher loading ratio spray. This was confirmed by photographic measurements downstream of $x/d = 50$ in the case 2 spray, where the ligaments were observed to have disappeared by $x/d = 100$.

From the photographs at $x/d = 50$ in the case 2 spray, the ligaments were estimated to be 20-25% by mass of the liquid flux at any radial location, and, therefore, were considered significant enough to be taken into account. The results of neglecting the ligaments is seen in Figure 11 where the SMD computed from the photographic data without including the ligaments is underestimated by about 15-30%, when compared to the results of the Fraunhofer diffraction and slide impaction techniques. The ligaments were therefore artificially broken down into a distribution of stable drops with the help of jet breakup theories given in Refs. [29,30], and knowledge of the maximum stable droplet diameter as obtained from photographic measurements downstream of $x/d = 50$. Appendix A gives a short description of the treatment of the ligaments.

Figure 10 shows the drop-size distributions at $x/d = 50$ in the case 2 spray after addition of the drops due to ligament breakup, and Figure 11 shows the corrected SMD. Since the drop-size distributions for this spray as determined by the slide impaction tests, cf., Figure 9, contain uncertainties (e.g., irregular ligament breakup at the probe inlet), the corrected photographic data was used as initial conditions for the SF calculations. Also, the spatial drop size distributions were transformed to temporal values by weighting the number fraction of each size group with the corresponding mean drop velocities, before using the data as initial conditions.

The SMD measurements illustrated in Figure 11 indicate that drops are observed for $r/x > 0.2$, which is beyond the edge of most fully-developed, single-phase jets. This effect is attributable to both initial radial velocities produced at the injector and dispersion of drops by turbulent fluctuations. Further implications of this observation and other measurements at the initial condition ($x/d = 50$) will be considered later.

Initial conditions of mean axial drop velocities for various radial locations at $x/d = 50$ in the case 1 and case 2 sprays are illustrated in Figures 15 and 16, respectively. For the case 1 spray, cf., Figure 15, a distinct increase of mean axial velocity with drop size is observed. For the case 2 spray, the velocities of drops with diameters greater than 150 μm , which were produced exclusively by the late breakup of ligaments as explained earlier, were estimated by extrapolation. In spite of this uncertainty, it is seen that the

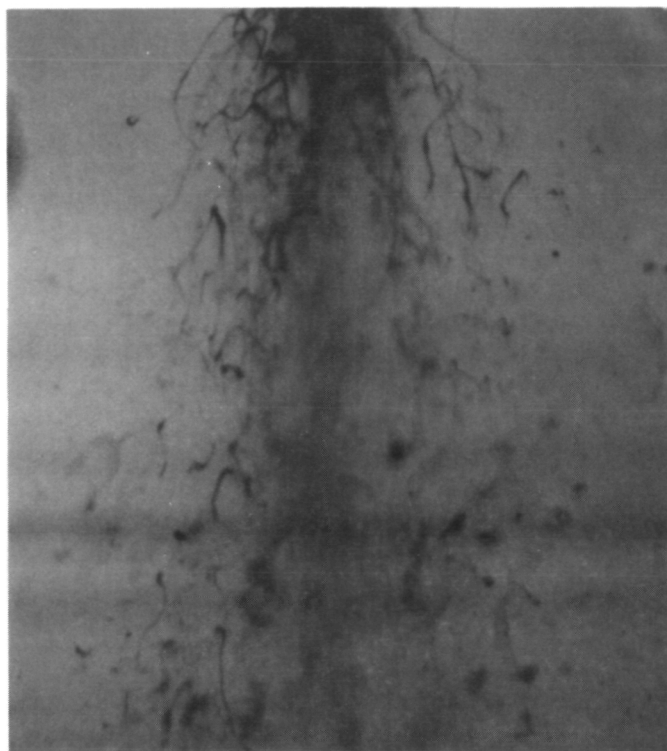


Figure 13. Photograph at exit of injector showing atomization process in the case 1 nonevaporating spray (flash exposure time duration = $0.8 \mu\text{s}$; x8 magnification).

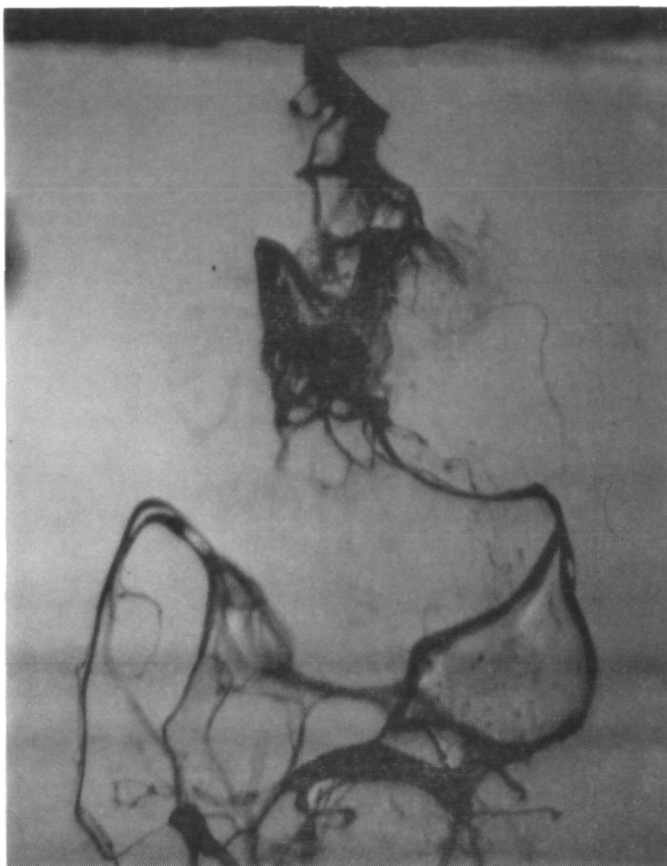


Figure 14. Photograph at exit of injector showing atomization process in the case 2 nonevaporating spray (flash exposure time duration = $0.8 \mu\text{s}$; x8 magnification).

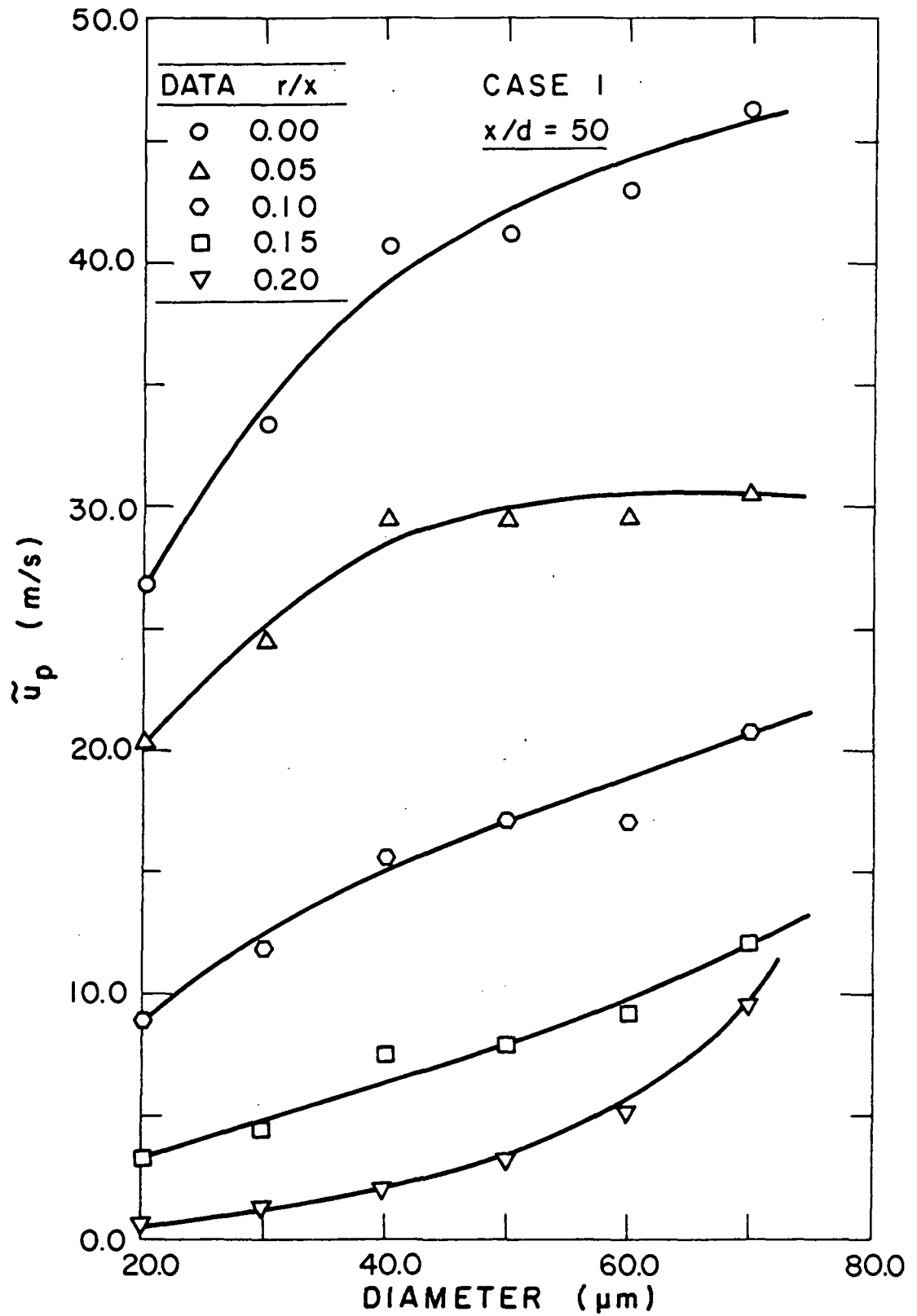


Figure 15. Initial conditions of drop size versus mean axial drop velocity at $x/d = 50$ for the case 1 nonevaporating spray.

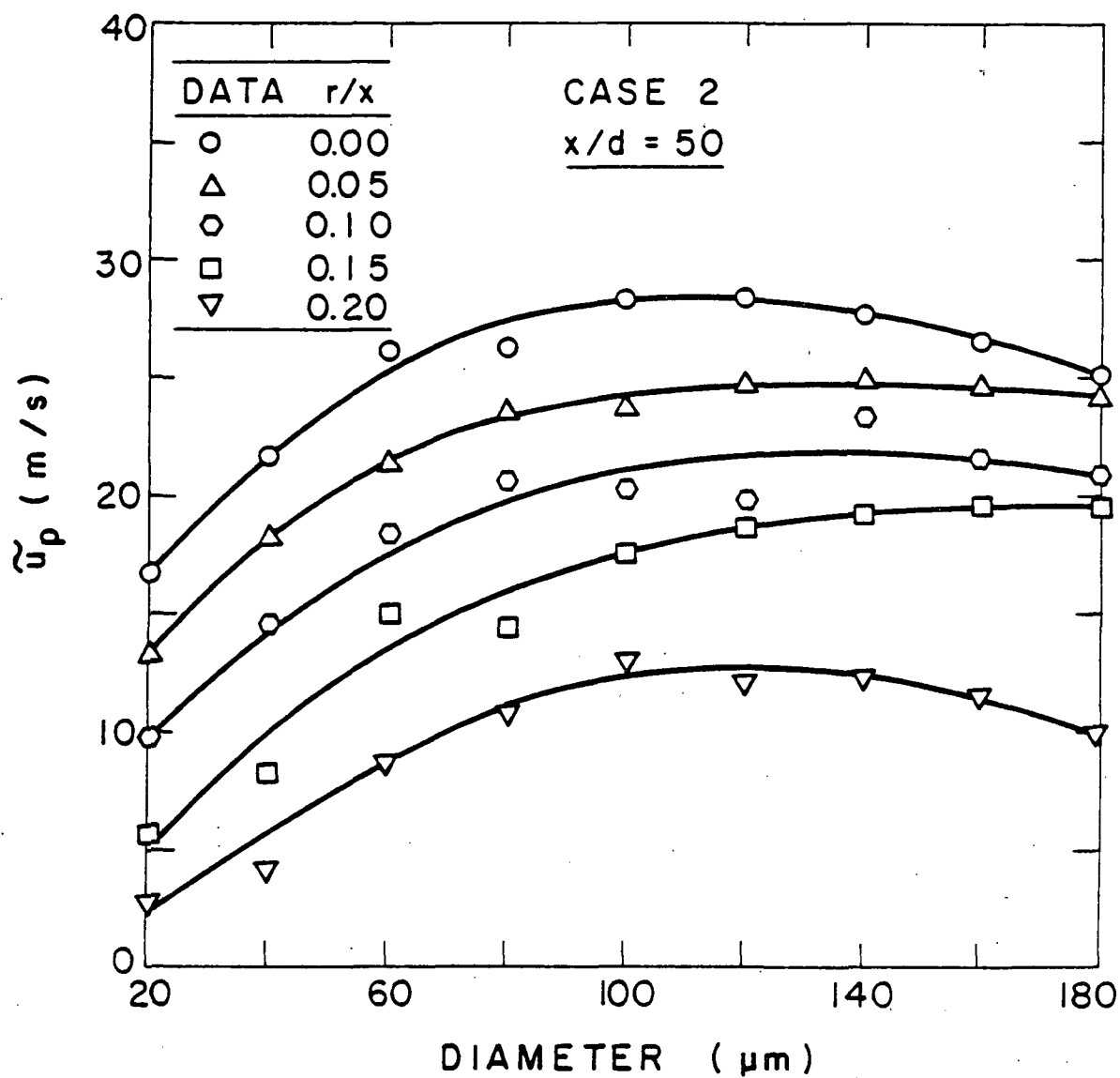


Figure 16. Initial conditions of drop size versus mean axial drop velocity at $x/d = 50$ for the case 2 nonevaporating spray.

velocities of drops greater than $100\text{ }\mu\text{m}$ is relatively uniform. As will be seen later, these and other drop velocity measurements downstream of $x/d = 50$ in the case 2 spray, suggests that the velocities of drops produced by breakup of ligaments in the late stages of atomization, are lower than those produced earlier in the process--differences in slip velocities in the two stages probably being the main reason for this behavior.

For both sprays at this axial location, drops with diameters $\leq 30\text{ }\mu\text{m}$ were found to possess axial velocities 10-15% below the gas-phase velocity for radial positions at or near the centerline of the sprays. This difference generally increased to 20-90% for positions near the edges of the sprays. Initial radial velocities and turbulent dispersion of drops is felt to be responsible for these observations. High initial radial velocities produced at the injector exit during the atomization process and turbulent dispersion of these drops to the far edges of the spray, into regions of low velocity (since at $x/d = 50$, drops of these sizes would have had sufficient residence time to undergo turbulent dispersion), would explain the presence of drops for $r/x > 0.2$, cf., Figure 11. Subsequent turbulent dispersion and re-entrainment of these drops back toward the center of the spray would result in drop velocities lower than the gas-phase velocity. These possible reasons are reinforced to a certain extent by photographic measurements at the edges of the sprays, which showed evidence of slight recirculation for drops with diameters $\leq 30\text{ }\mu\text{m}$, particularly for the case 1 spray. The largest drops, however, were found to have velocities 10-300% greater than the local gas-phase velocity.

Initial conditions of fluctuating axial drop velocities in the case 1 spray for various radial locations at $x/d = 50$ are illustrated in Figure 17. Despite the scatter in the data, it is seen that the fluctuating axial drop velocities generally increase with drop size, just as in the case of the mean velocities. In addition, the relative fluctuation levels (relative to the mean axial drop velocities at the centerline) were between 25-40% at the spray axis, and decreased to 2-10% at the edges of the spray. The same measurements for the case 2 spray, however, exhibit a great deal of scatter as seen in Figure 18--the relatively slower rate of the atomization process probably being the main reason for this behavior.

As stated earlier, the resolution of the photographic technique used to measure drop size and velocity did not permit measurement of mean and fluctuating radial drop velocities. Hence, for SF model computations, the initial mean radial drop velocity was assumed to increase linearly from the spray axis to the edge of the flow, matching the spray angle at the latter condition, viz. $\bar{v}_p = 0.7 \bar{u}_p r/x$. Initial conditions of fluctuating radial drop velocities were specified to be a constant ratio of the corresponding measured fluctuating axial drop velocity, viz. $(\tilde{v}_p^2)^{1/2} = (\tilde{u}_p^2)^{1/2}/3.0$. The above constants were selected to best match the predictions of the SSF model with measurements downstream of $x/d = 50$. The same specifications for the above quantities were used for both sprays.

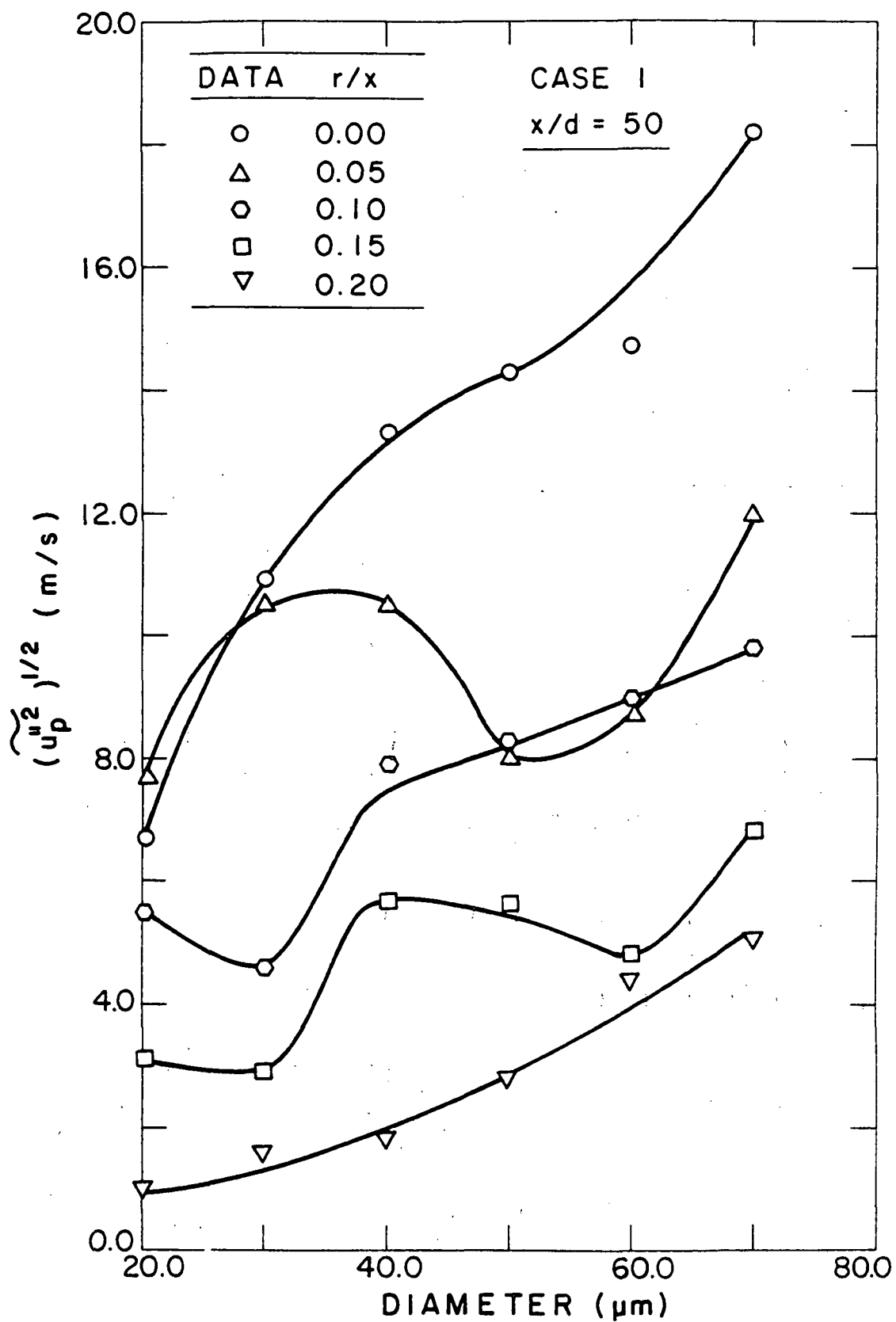


Figure 17. Initial conditions of drop size versus fluctuating axial drop velocities at $x/d = 50$ for the case 1. nonevaporating spray.

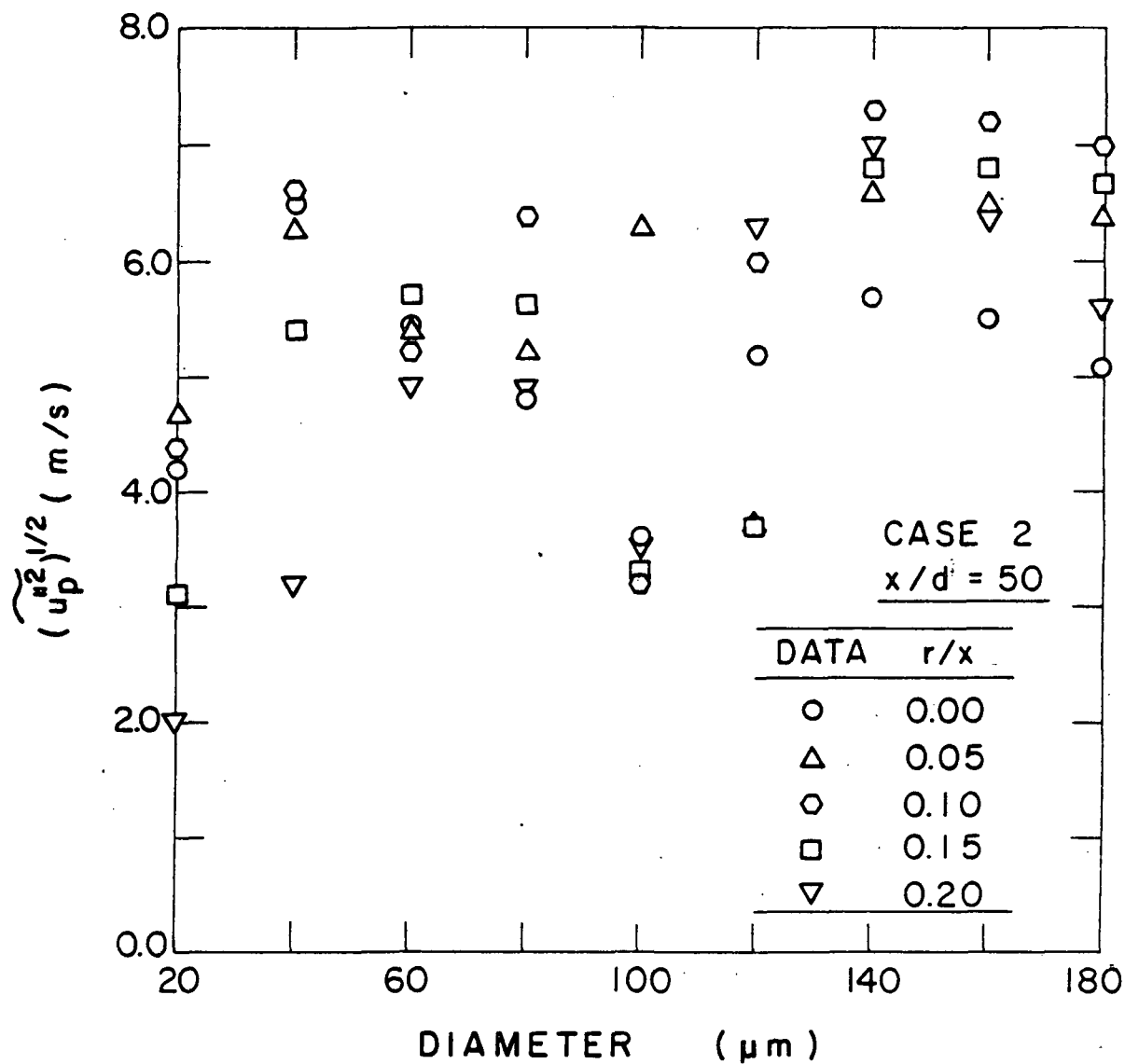


Figure 18. Initial conditions of drop size versus fluctuating axial drop velocity at $x/d = 50$ for the case 2 nonevaporating spray.

4.4 Axial Variation of Spray Properties

Once initial conditions were established, the remaining measurements were used to evaluate model predictions. Since the LHF model was not limited to a dilute spray and had appropriate initial conditions at the injector exit, results for this model were obtained throughout the entire flow. The DSF and SSF model predictions, however, were limited to the dilute portion of the spray--beginning at $x/d = 50$ where initial conditions for these models were measured.

Predicted and measured mean-gas velocities along the axis of the two sprays are illustrated in Figure 19. The LHF predictions of mean velocity for the more finely atomized spray tend to underestimate the measurements slightly, similar to the findings of Shearer et al. [14] for an evaporating spray having a similar SMD. It will become evident, however, that this agreement is partly fortuitous, since the LHF model significantly underestimates the width of this spray. Typical of earlier experience with LHF models of sprays [14] the LHF model overestimates the decay of axial velocity in the coarser spray, due to the neglect of effects of slip between the phases. In contrast, the SSF model provides satisfactory predictions of mean centerline velocities for both sprays.

The same models are compared with measurements of liquid mass flux along the axis of the two sprays in Figure 20. The LHF predictions do not approach the measurements until large values of x/d , where effects of interphase slip are relatively small. The SSF model, however, provides reasonably good predictions throughout the range of x/d where it was used.

Predicted and measured mean axial drop velocities along the axis of the case 1 and case 2 sprays are illustrated in Figures 21 and 22, respectively. In both cases, the mean drop velocity becomes less variable with changes in drop size, with increasing axial distance from the injector. The larger drops are decelerated at a faster rate relative to the smaller drops due to both the higher initial slip velocities of the large drops and the nonlinear nature of the drag law. Furthermore, at greater axial distances, the intermediate-size drops have had sufficient residence time to be dispersed radially outwards into lower velocity regions of the spray at some period during their history. Far downstream, at $x/d = 600$, the slip velocity decreases to a negligible value (considering the error-limits associated with the velocity measurement techniques of both phases), except for the largest drops.

As mentioned earlier, the largest size drops (diameters $\geq 160 \mu\text{m}$) generated by the late breakup of ligaments in the case 2 spray are observed to have relatively lower velocities. This can be noted from the data for the case 2 spray at $x/d = 100$ and $x/d = 150$, cf., Figure 22.

Predictions of both the DSF and SSF models are also compared with the mean axial drop velocity measurements illustrated in Figures 21 and 22. Beginning at the same initial conditions for the mean-drop

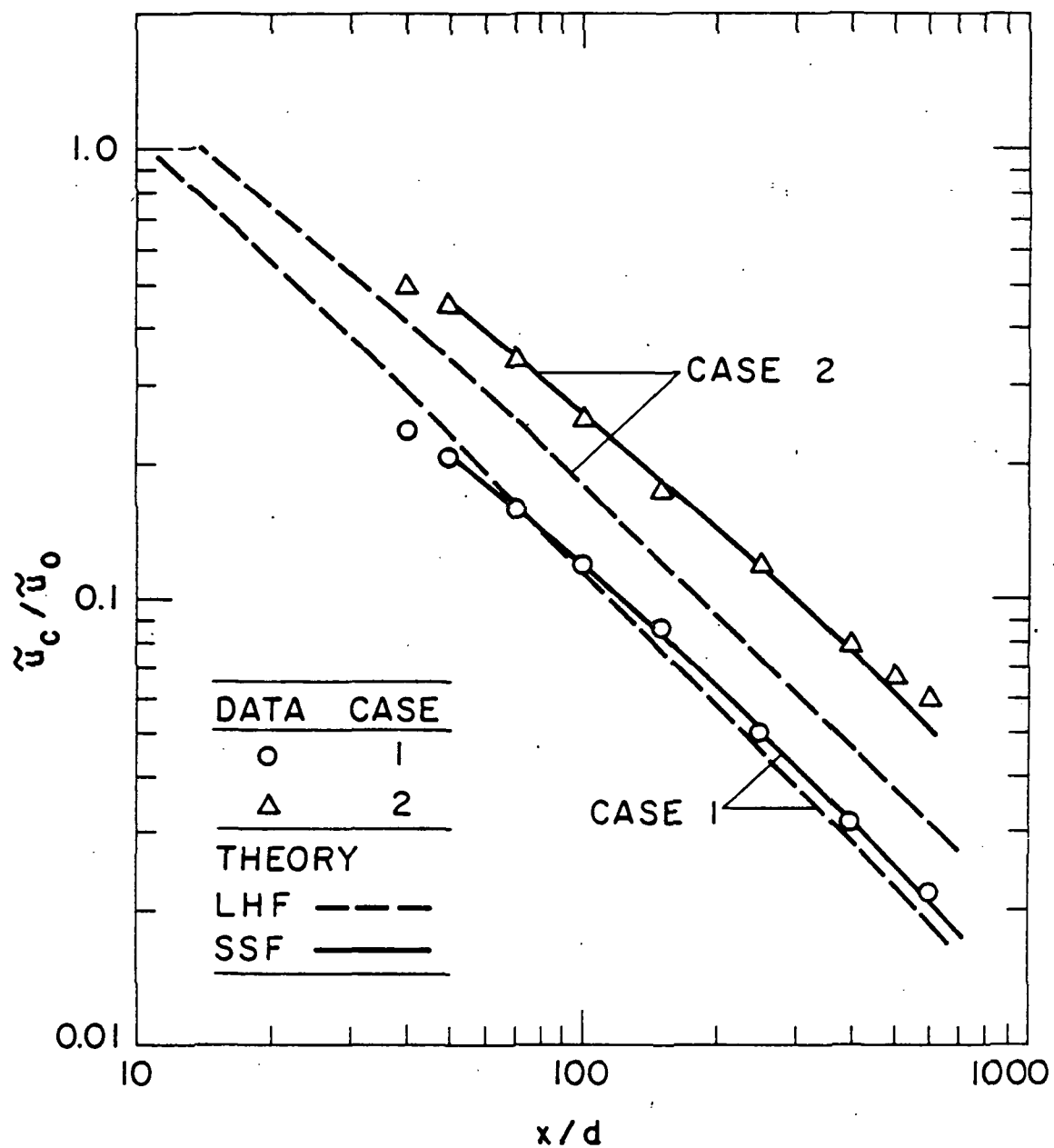


Figure 19. Predicted and measured mean gas-phase velocities along the axis of the nonevaporating sprays.

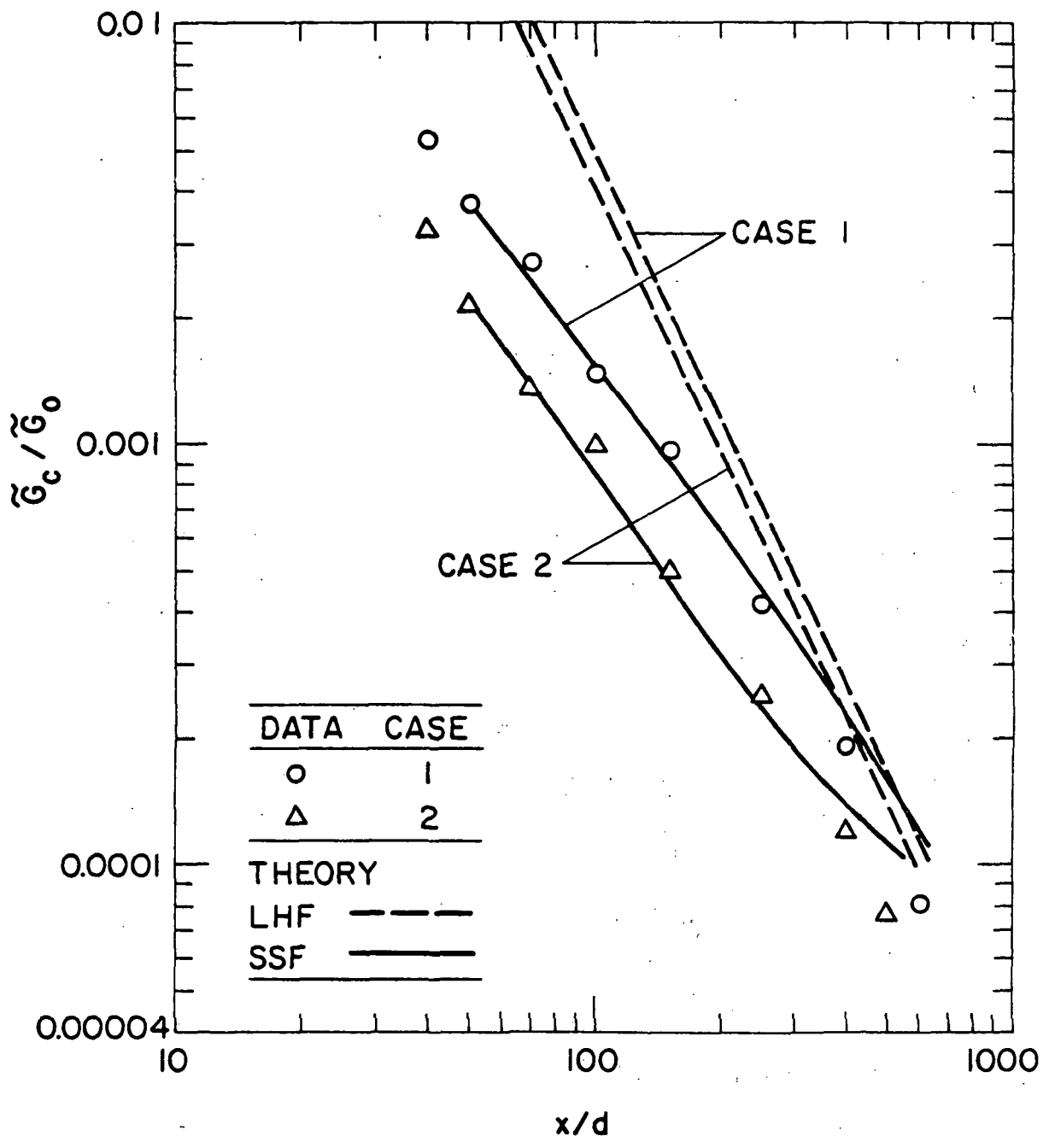


Figure 20. Predicted and measured mean liquid flux along the axis of the nonevaporating sprays.

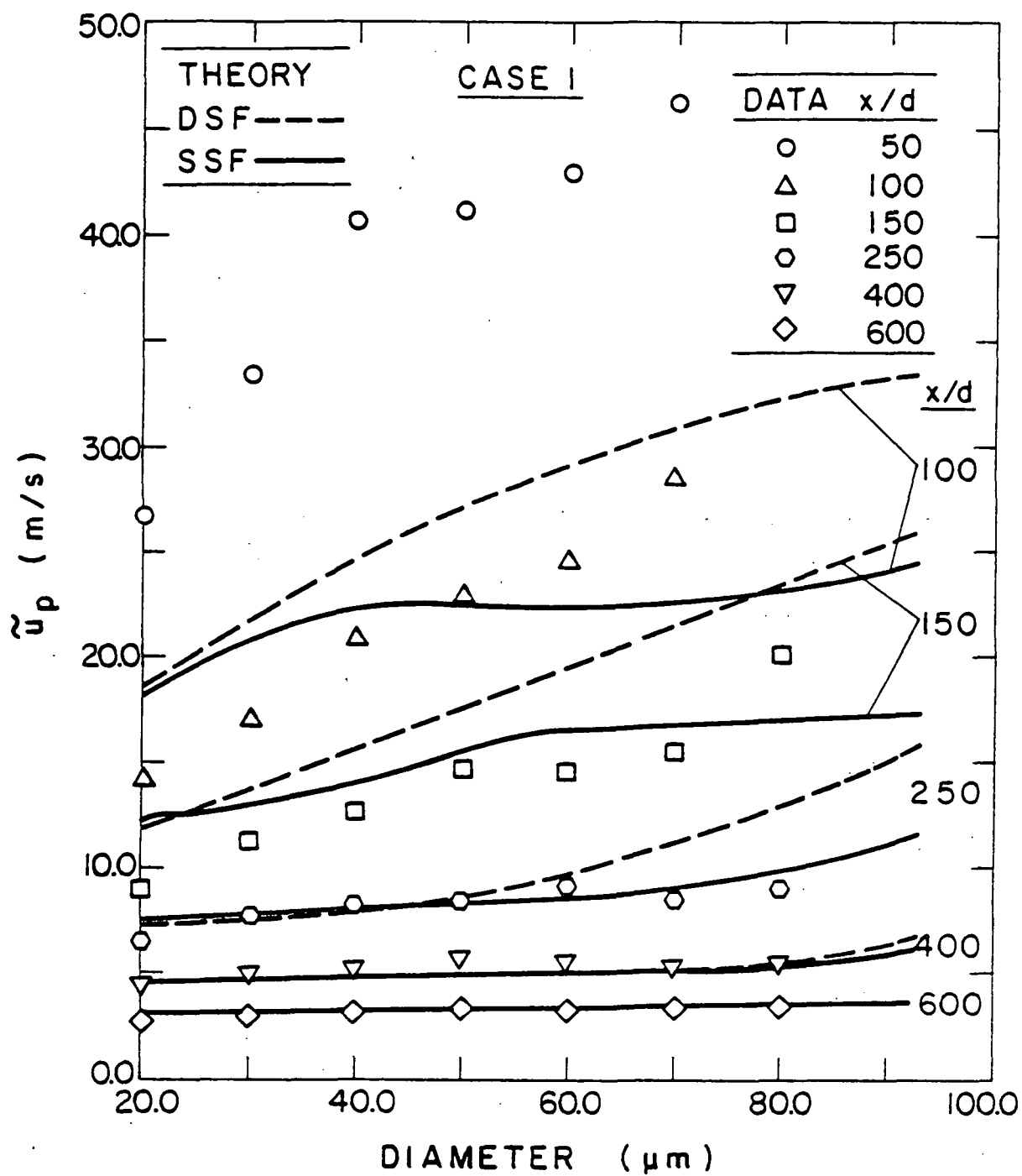


Figure 21. Predicted and measured mean axial drop velocities along the axis of the case 1 nonevaporating spray.

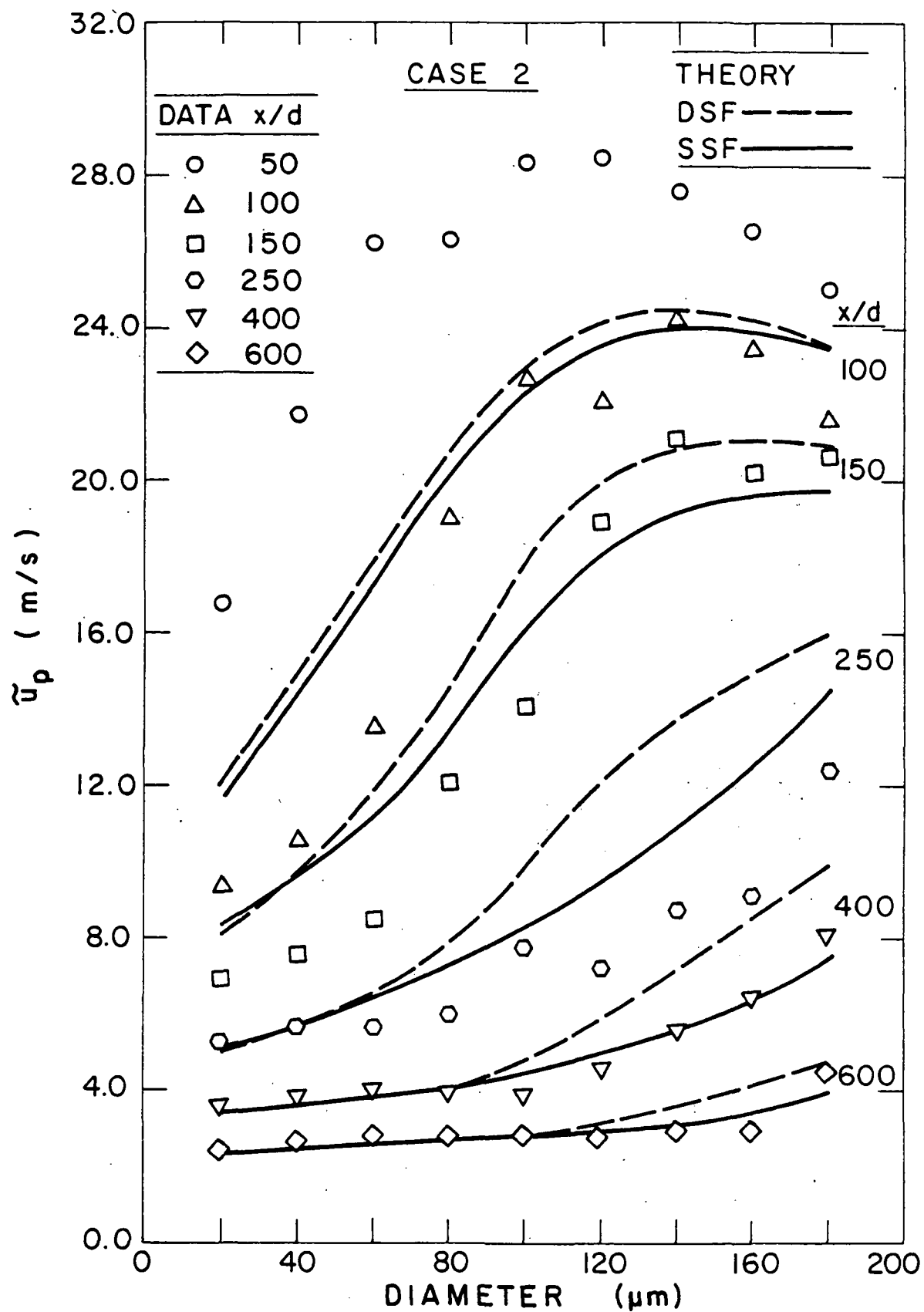


Figure 22. Predicted and measured mean axial drop velocities along the axis of the case 2 nonevaporating spray.

velocities at $x/d = 50$, the DSF model underestimates the deceleration of the drops for axial distances up to $x/d = 250$, while the SSF model better estimates the data due to inclusion of the effect of turbulent fluctuations on drop motion. Both models, however, make a reasonable estimation of the data far downstream in both the sprays, especially for the smaller drops where the agreement is quite good.

Measurements and SSF model predictions of the axial variation of fluctuating axial drop velocities for the case 1 spray are shown in Figure 23. The SSF model consistently underestimates the data, especially for the larger size drops. Since the data is an average over a $10\text{ }\mu\text{m}$ diameter size range; this variance in size may partly explain the high velocity fluctuation levels measured. Furthermore, sample sizes used for the larger size drops were generally insufficient to obtain more than a qualitative indication of fluctuating drop velocities in these size ranges. The same measurements for the case 2 spray, shown in Figure 24, exhibit large scatter for $x/d \leq 250$ --which can again be explained by the slow rate of atomization for this spray. Measurements of fluctuating axial drop velocities were generally inconclusive for model evaluation due to the reasons stated above and the added uncertainties in the initial conditions for these properties; and will therefore not be considered any further here.

One of the most interesting features observed during the present study is seen in Figure 25 which shows the comparison between measurements and predictions of the SF models for the axial variation of SMD along the centerline of both nonevaporating sprays. All drop size data downstream of $x/d = 50$ were obtained by photography, and hence are spatial measurements, proportional to concentration. The temporal predictions of SMD by the SF models were therefore transformed to spatial values for purposes of comparison with measurements. In both sprays, the SMD is observed to increase gradually with axial distance. At $x/d = 600$, an increase of 16% and 23% of the values of SMD at $x/d = 100$ is noted for the case 1 and case 2 sprays, respectively. It is also seen from Figure 25 that the SSF model predicts the correct trend, being in excellent agreement for the case 1 spray in particular. On the other hand, the DSF model estimates that the SMD remains constant or decreases somewhat with increasing axial distance; resulting in an underestimation of the SMD along the centerline of both sprays. A feature such as that observed in Figure 25 is probably due to size-dependent turbulent dispersion of drops, accounted for by the SSF model, but entirely neglected in the DSF model which allows only for deterministic trajectories of drops.

A further understanding of the above phenomena can be gained by observing the evolution of drop-size distributions along the axis of the case 1 and case 2 sprays, illustrated in Figure 26. For the more finely atomized case 1 spray, a gradual increase in the relative fraction of drops $> 60\text{ }\mu\text{m}$ diameter is noticed. The relative increase in the number of these large drops at the centerline of the spray can be attributed to turbulent dispersion of the smaller drops toward the edge of the spray. As mentioned earlier, the fraction of larger drops in the size distribution have a relatively larger influence on the SMD than the fraction of smaller drops. Similar behavior is observed in

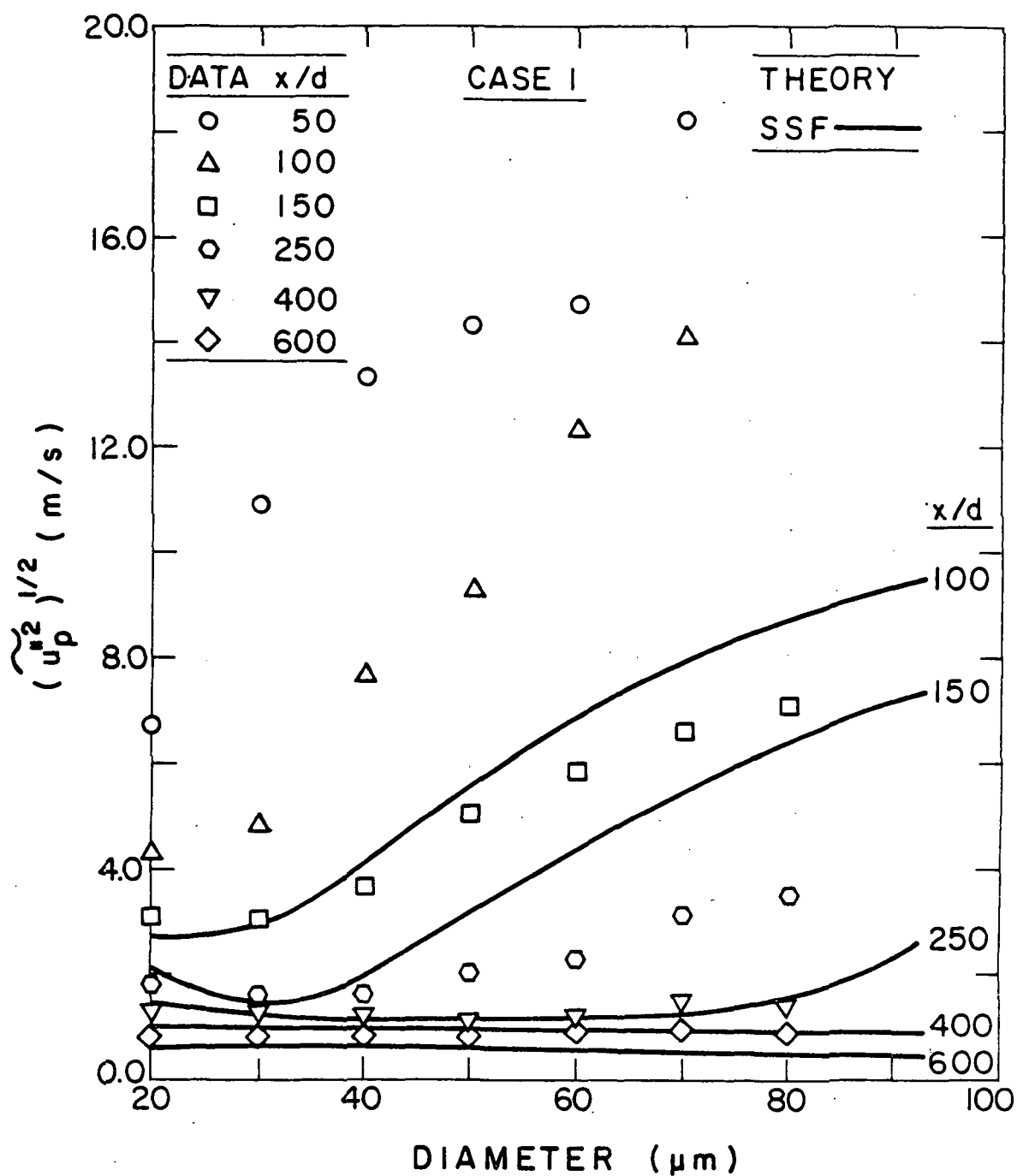


Figure 23. Predicted and measured fluctuating axial drop velocities along the axis of the case 1 nonevaporating spray.

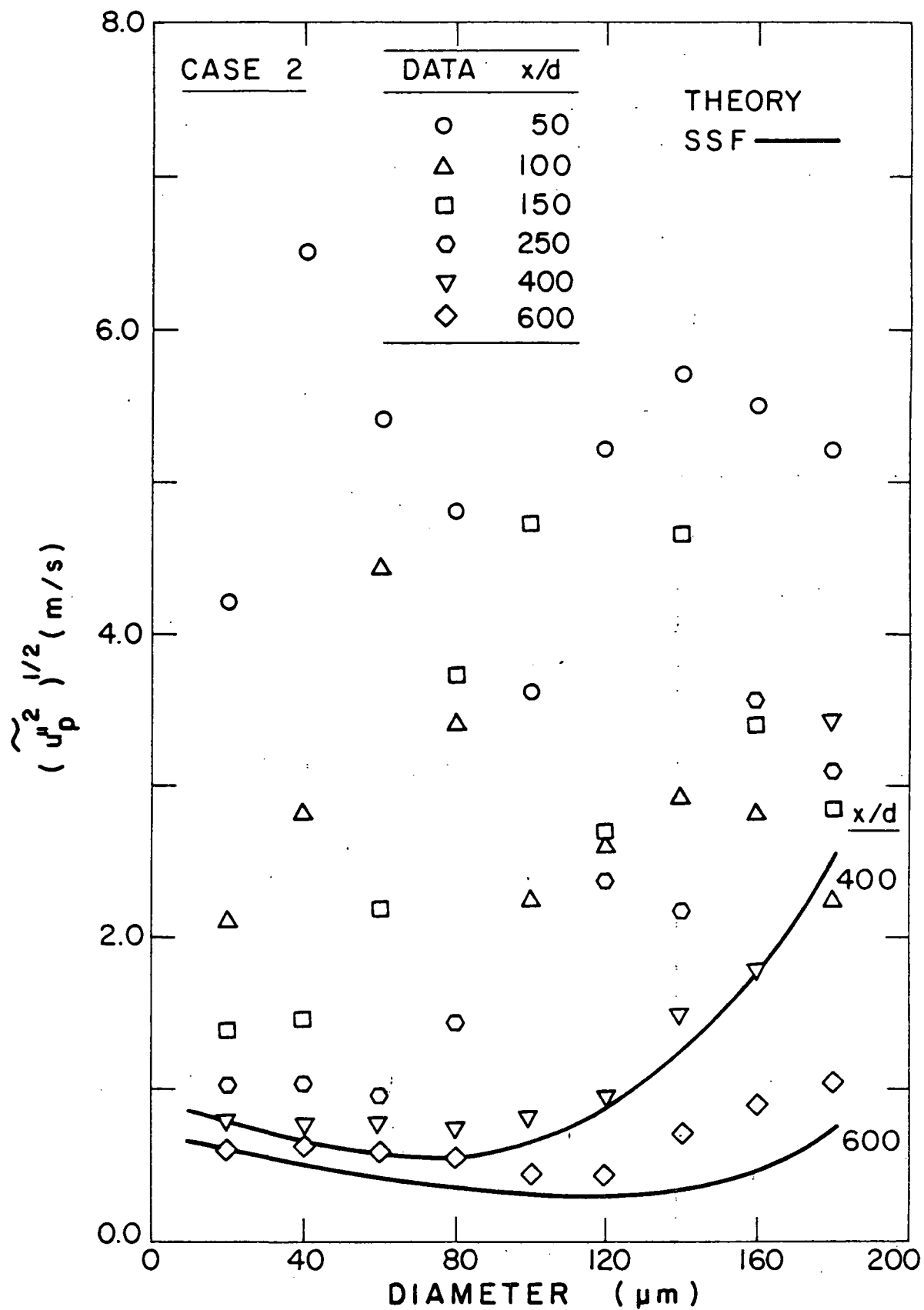


Figure 24. Predicted and measured fluctuating axial drop velocities along the axis of the case 2 nonevaporating spray.

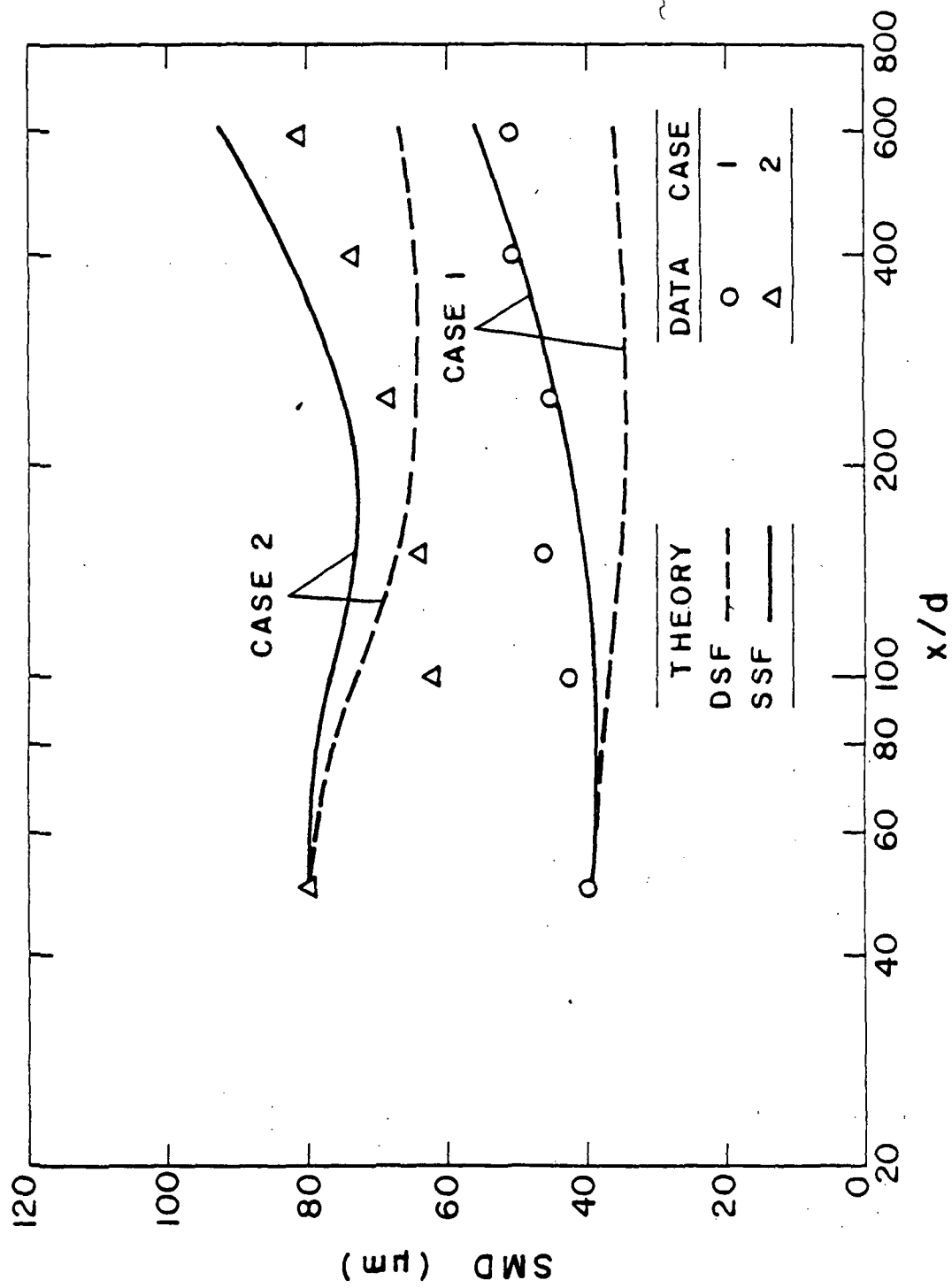


Figure 25. Predicted and measured SMD along the axis of the nonevaporating sprays.

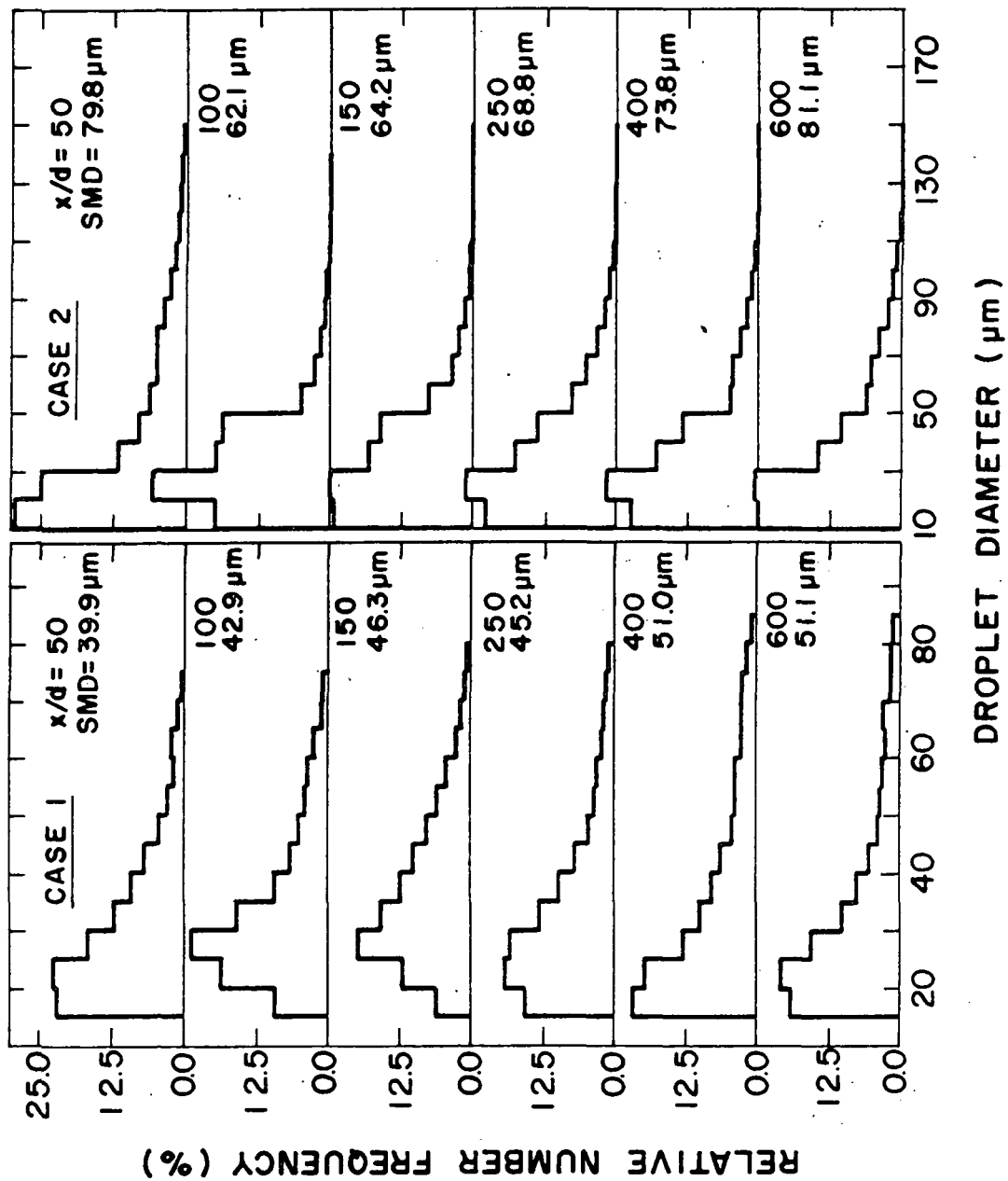


Figure 26. Drop-size distributions along the axis of the case 1 and case 2 nonevaporating sprays.

the evolution of drop-size distributions for the coarser case 2 spray, where the relative fraction of drops $> 90 \mu\text{m}$ diameter increases with axial distance.

4.5 Radial Variation of Mean-Spray Properties

Predicted and measured radial profiles of mean axial gas velocities are illustrated in Figure 27, including the initial condition at $x/d = 50$. Predictions from both the LHF and SSF models are shown on the plot. The results illustrate an interesting property of these sprays. During the computations for particle-laden jets, Reference [2], the LHF model invariably overestimated the width of the flow since neglecting slip causes the rate of dispersion of heavy particles by the turbulence to be overestimated. In the present case, however, the spray spreads more rapidly than the LHF prediction, due to enhanced dispersion of drops. The increased response of the drops in the present sprays, in comparison to the solid particles in the particle-laden jets of Reference [2], can be attributed to: (1) the smaller density of the drops; (2) the greater rates of flow deceleration due to the smaller injector dimensions of the sprays; and (3) the larger initial slip between the liquid and gas phases in the sprays. It is very encouraging that the SSF model can reproduce this unexpected effect, with no change in the modeling procedure and empirical constants.

Predicted and measured radial profiles of liquid mass flux are illustrated in Figure 28. In this case, results for the DSF model are shown along with the LHF and SSF predictions. The DSF model yields poor results, similar to particle-laden jets [2]. Neglecting drop dispersion by the turbulence causes the rate of spread of the flow to be substantially underestimated--even after allowing for the apparent radial velocity of the drops at $x/d = 50$. Other predictions of the DSF model were also not very satisfactory; therefore this method will not be considered any further here.

As before, the SSF model yields the most satisfactory predictions of flow properties for the results illustrated in Figure 28. The performance of the SSF model, however, is poorer for liquid flux than for other measurements considered during this study. Since liquid flux predictions are more sensitive to estimations of initial conditions than other spray properties, uncertainties in initial conditions are a potential source for these errors. Additional measurements of drop radial velocities will be required to resolve this effect.

Measurements of the radial variation of mean axial drop velocities at $x/d = 250$ in the case 1 spray are illustrated in Figure 29, along with the predictions of the SSF model. Drop velocities tend to be more uniform with increasing radial distance. Drops less than $30 \mu\text{m}$ diameter possessed velocities 10-50% less than the gas-phase velocity, while the largest drops had velocities 15-27% larger than the gas-phase value. The above two observations are similar to those made in the case of the axial variation of mean axial drop velocities. The SSF model slightly overestimates the data at all radial positions, except at the centerline, where the agreement is better.

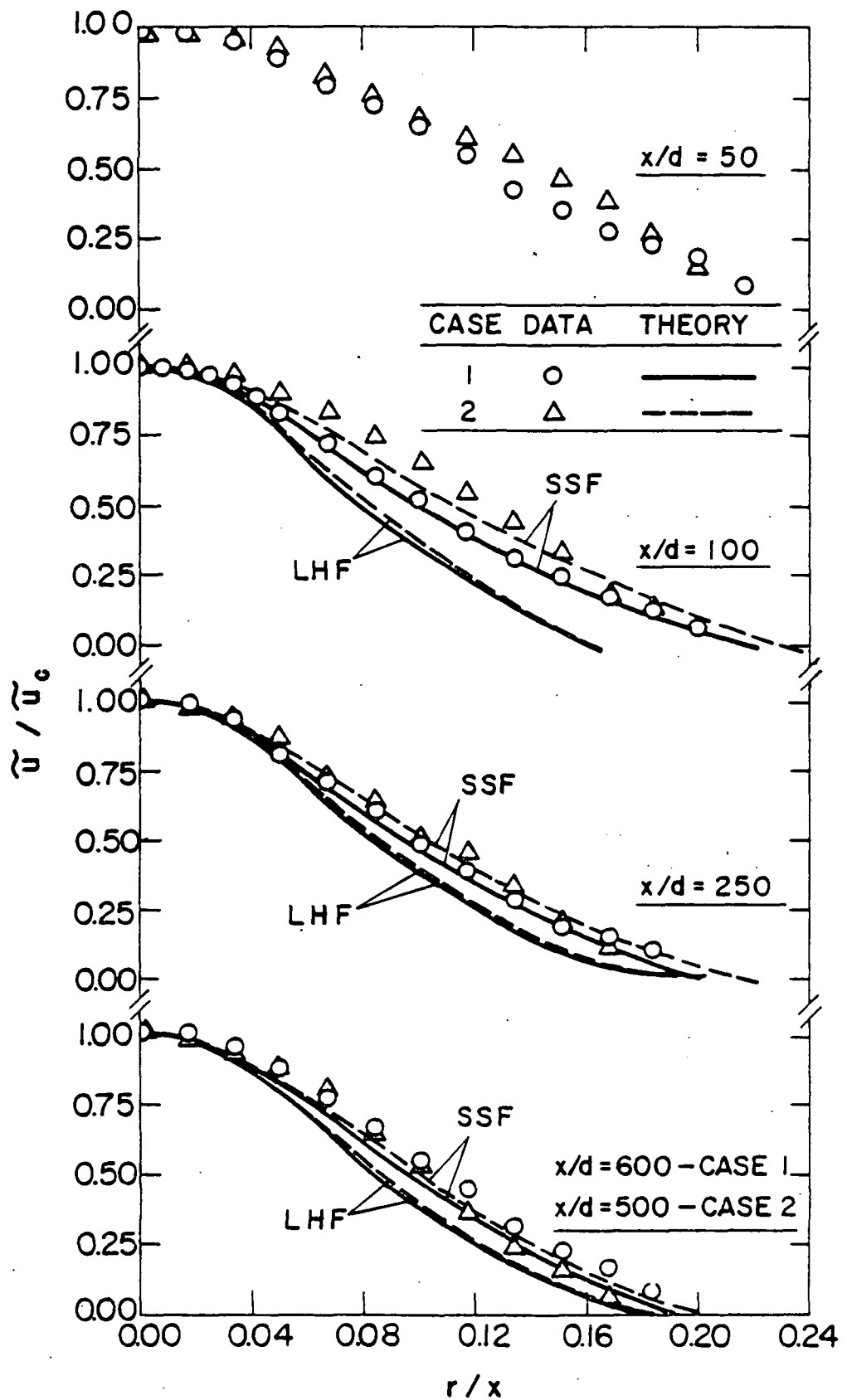


Figure 27. Predicted and measured radial variation of mean gas-phase velocities in the nonevaporating sprays.

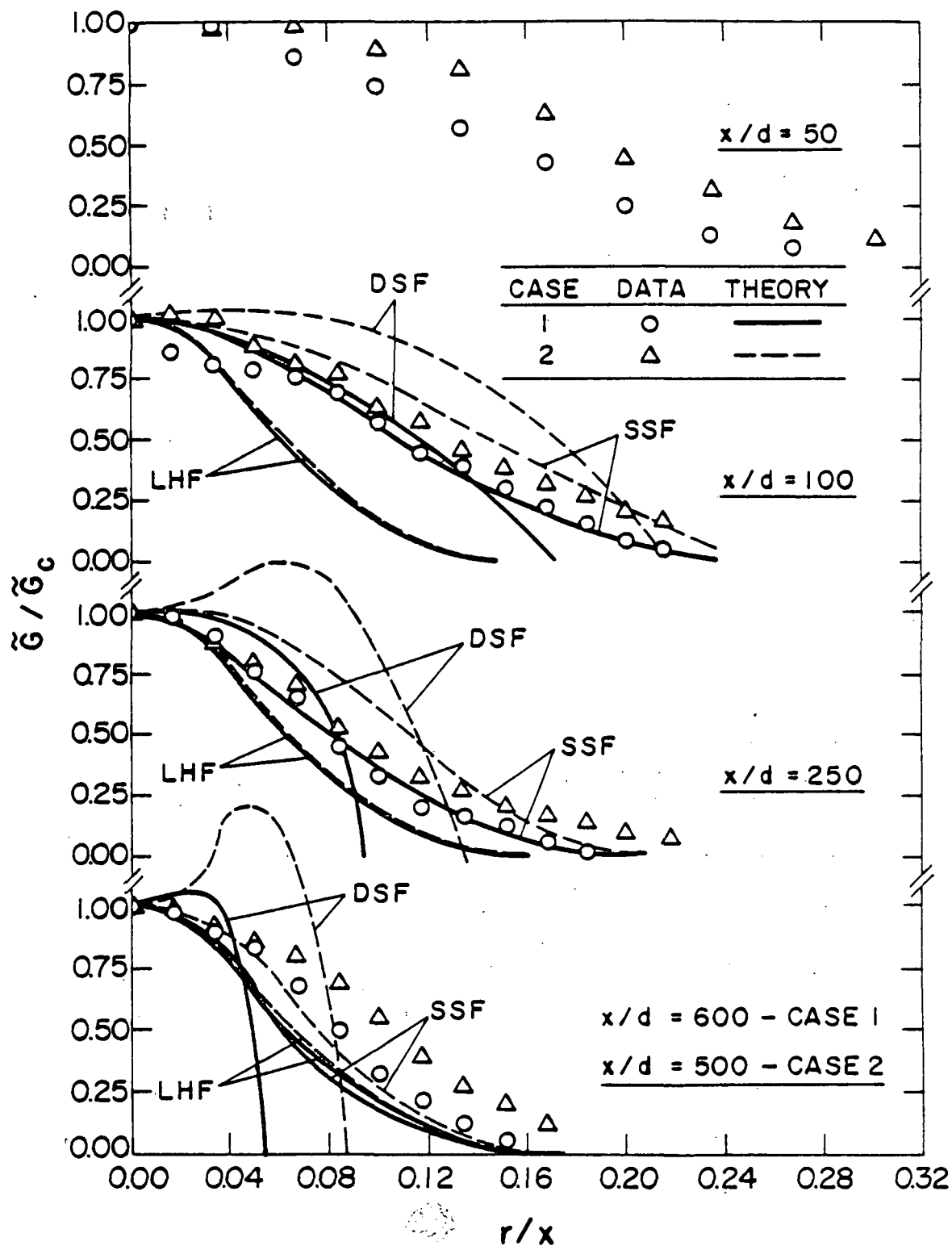


Figure 28. Predicted and measured radial variation of mean liquid flux for the nonevaporating sprays.

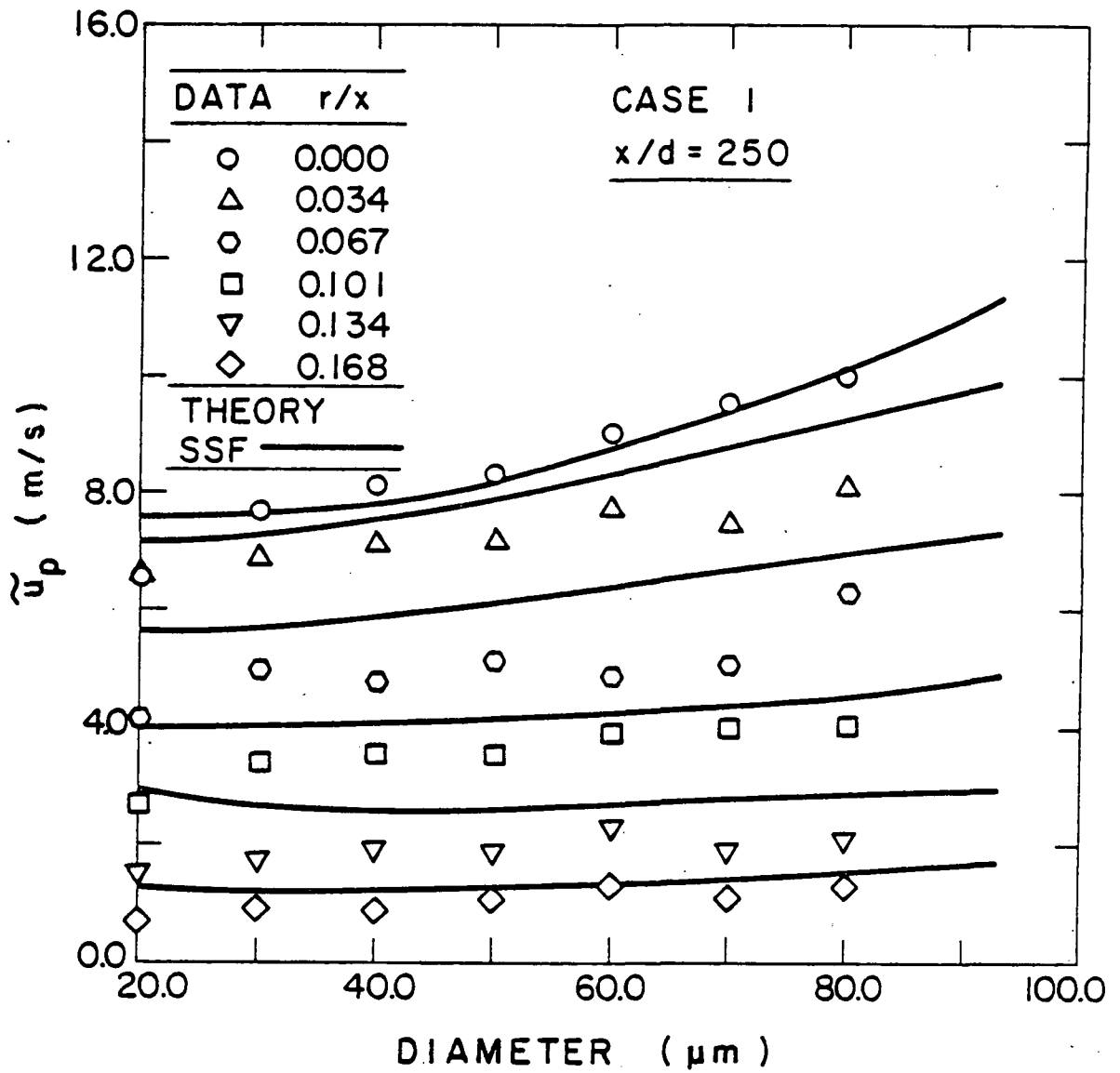


Figure 29. Predicted and measured radial variation of mean axial drop velocities at $x/d = 250$ in the case 1 nonevaporating spray.

The above results for the coarser case 2 spray are illustrated in Figure 30. In this case, the larger drops, due to their larger inertia, tend to maintain their velocities to a greater extent when compared to the more finely atomized case 1 spray data. The effect of the late breakup of ligaments again introduces uncertainties in the velocities of the large drops as evident by the scatter in the data for drops $> 120 \mu\text{m}$ diameter. As in the case of the finer spray, the SSF model overestimates the mean axial drop velocities at this axial location.

Measurements of drop-size distributions across the case 1 and case 2 sprays at $x/d = 250$ are illustrated in Figure 31. The SMD calculated from these distributions and the predictions of the SSF model are illustrated in Figure 32. No significant trend can be observed, except for the slight increase in the fraction of the larger drops and in the SMD toward the edge of the spray. Effects on drop-size distribution at this location ($x/d = 250$) can be expected to be a combination of initial radial drop velocities and turbulent dispersion of drops. The SSF model reasonably estimates the radial variation of SMD in both the sprays, cf., Figure 32.

4.6 Radial Variation of Gas-Phase Turbulence Properties

All three components of the velocity fluctuations were measured, allowing k to be computed for comparison with predictions. These results are illustrated in Figure 33. The agreement between predictions of the SSF model and the measurements is reasonably good. The fact that turbulence levels roughly correspond to values estimated from a model which ignores effects of particle motion on turbulence properties, indicates that effects of turbulence modulation (suggested by Al Taweel and Landau [31]), or turbulence production by drops, were small for the present flows. This is reasonable, since the present comparison is confined to dilute portions of the spray.

Predicted and measured profiles of Reynolds stress are illustrated in Figure 34. The SSF predictions are adequate for both sprays. This is consistent with the reasonably good predictions of mean velocities and k obtained with this model for the test sprays.

Effects of the presence of drops on turbulence properties are more evident when individual components of velocity fluctuations are examined. Measured radial profiles of u' , v' and w' are illustrated in Figures 35 and 36 for the finely and coarsely atomized sprays. Predictions were obtained assuming $(u'^2:v'^2:w'^2) = (1:0.5:0.5) k$, which is approximately observed in the fully-developed region of single-phase round jets [32,33]. Predictions constructed in this manner are in fair agreement with the measurements--particularly in the region far from the injector. A notable feature of the results, however, is that levels of anisotropy are rather high for positions near the injector and generally exceed levels observed for comparable values of x/d in single-phase jets [32,33]. Since this region abuts the dense-spray portion of the flow, it seems likely that the presence of drops are responsible for the higher degree of anisotropy since

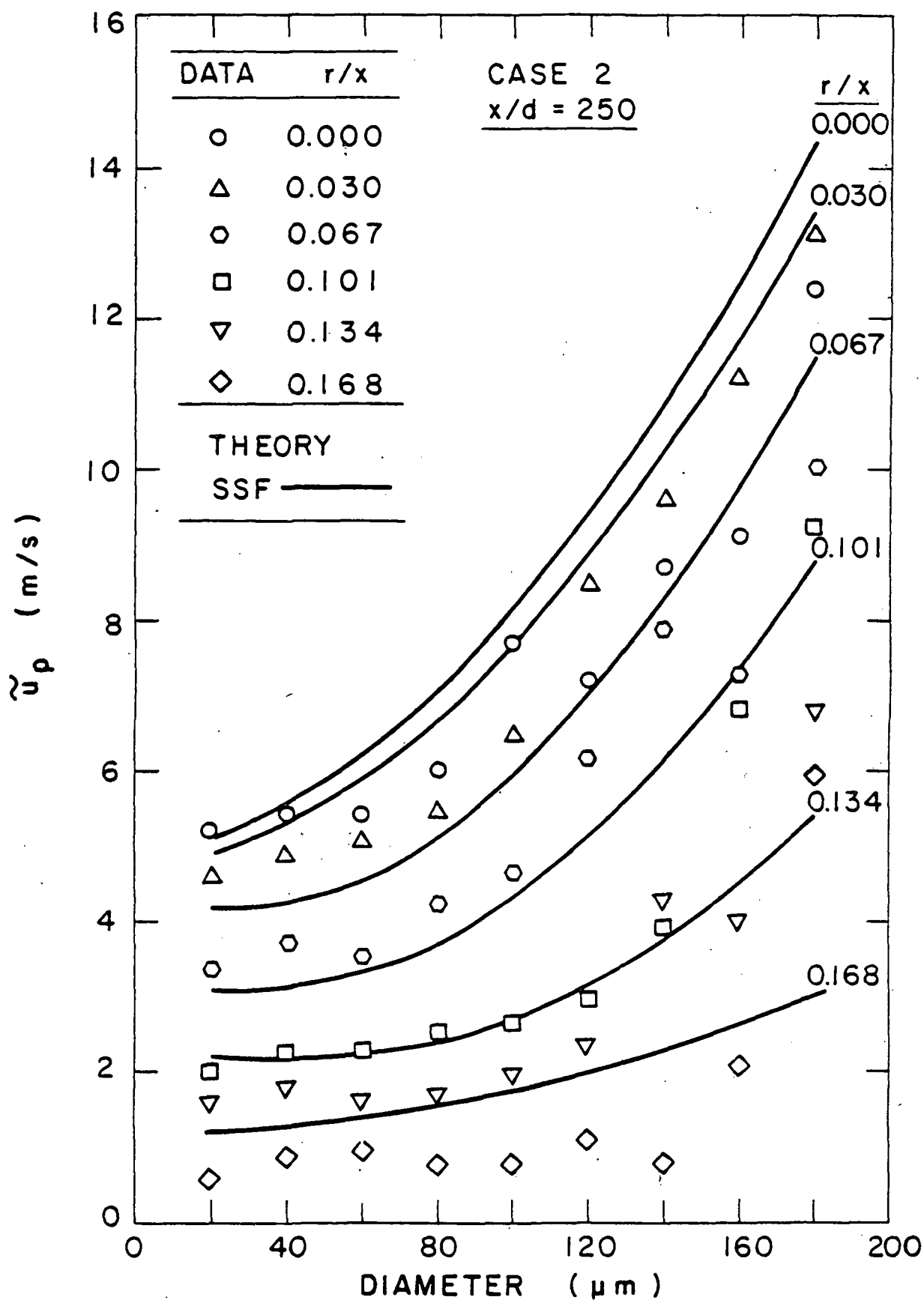


Figure 30. Predicted and measured radial variation of mean axial drop velocities at $x/d = 250$ in the case 2 nonevaporating spray.

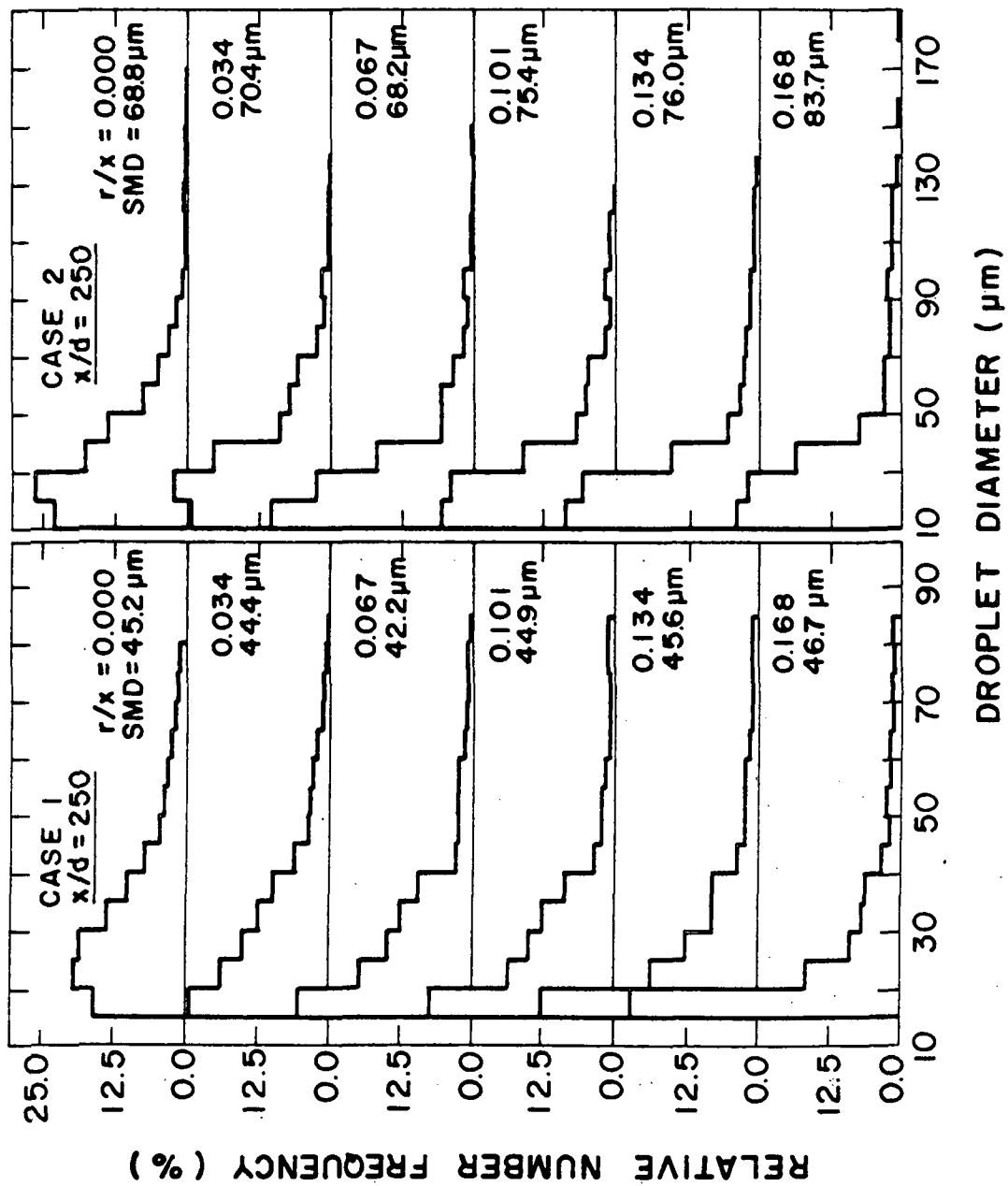


Figure 31. Drop-size distributions in the case 1 and case 2 nonevaporating sprays at $x/d = 250$.

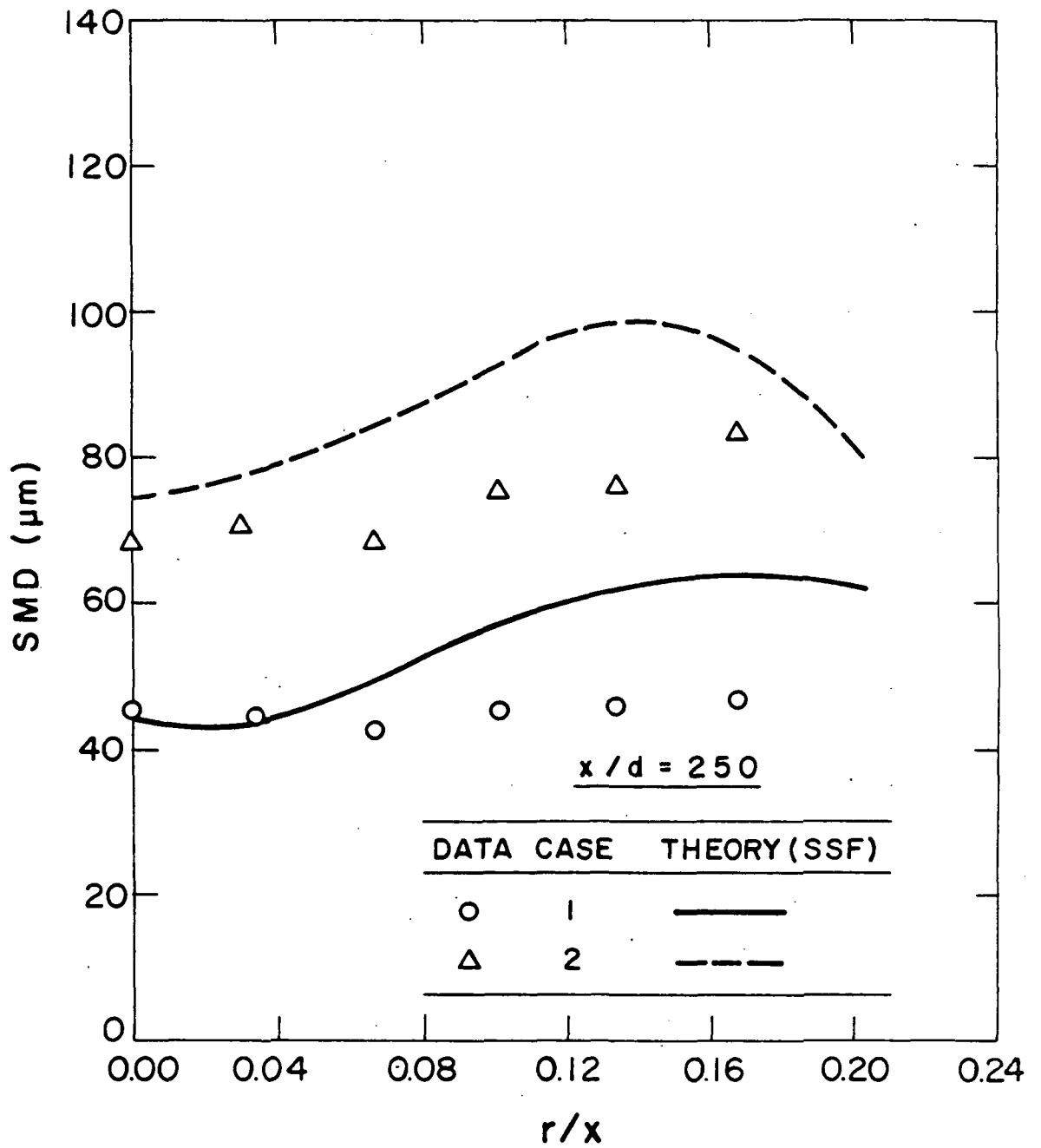


Figure 32. Predicted and measured radial variation of SMD at $x/d = 250$ in the nonevaporating sprays.

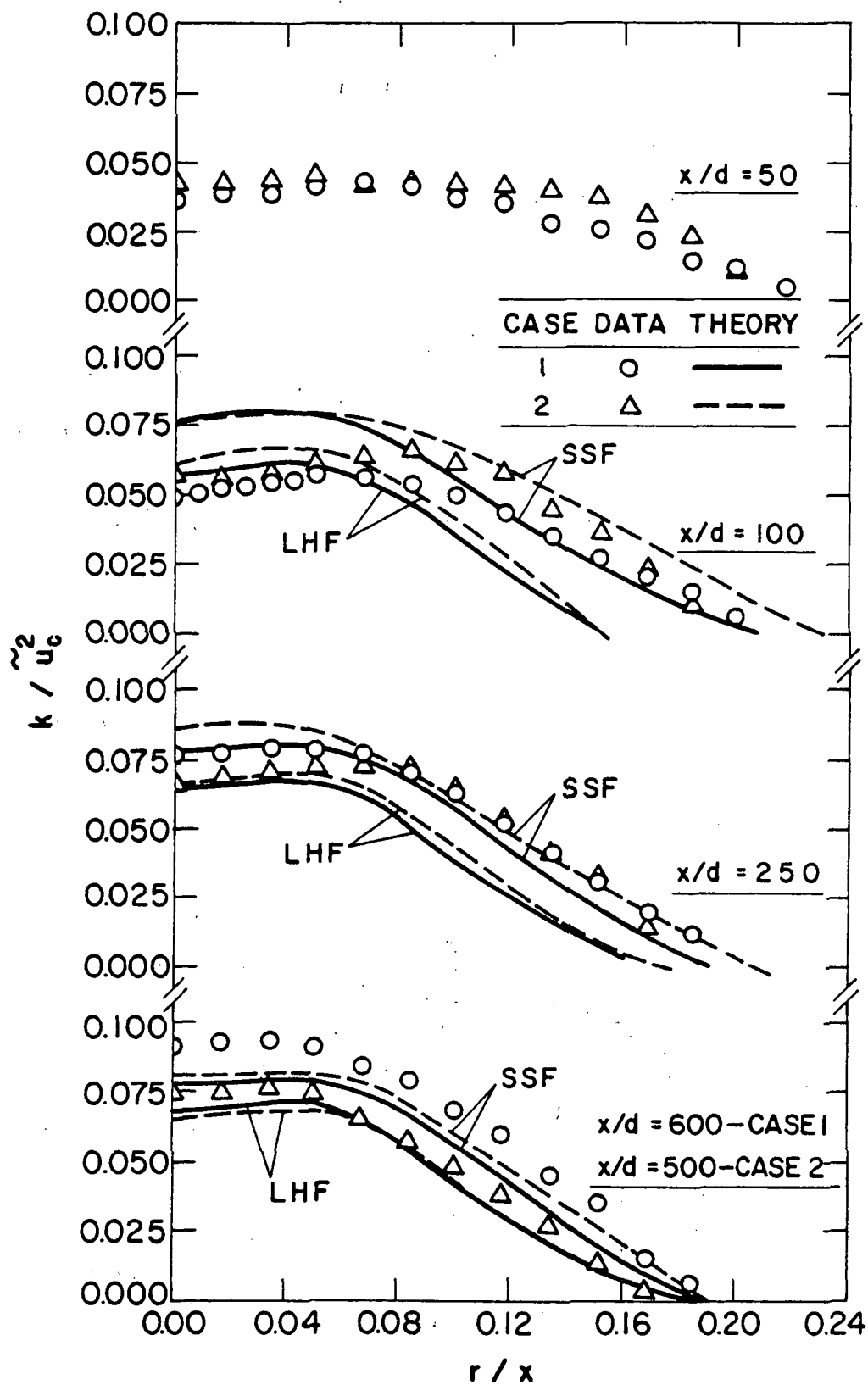


Figure 33. Predicted and measured radial variation of turbulent kinetic energy in the nonevaporating sprays.

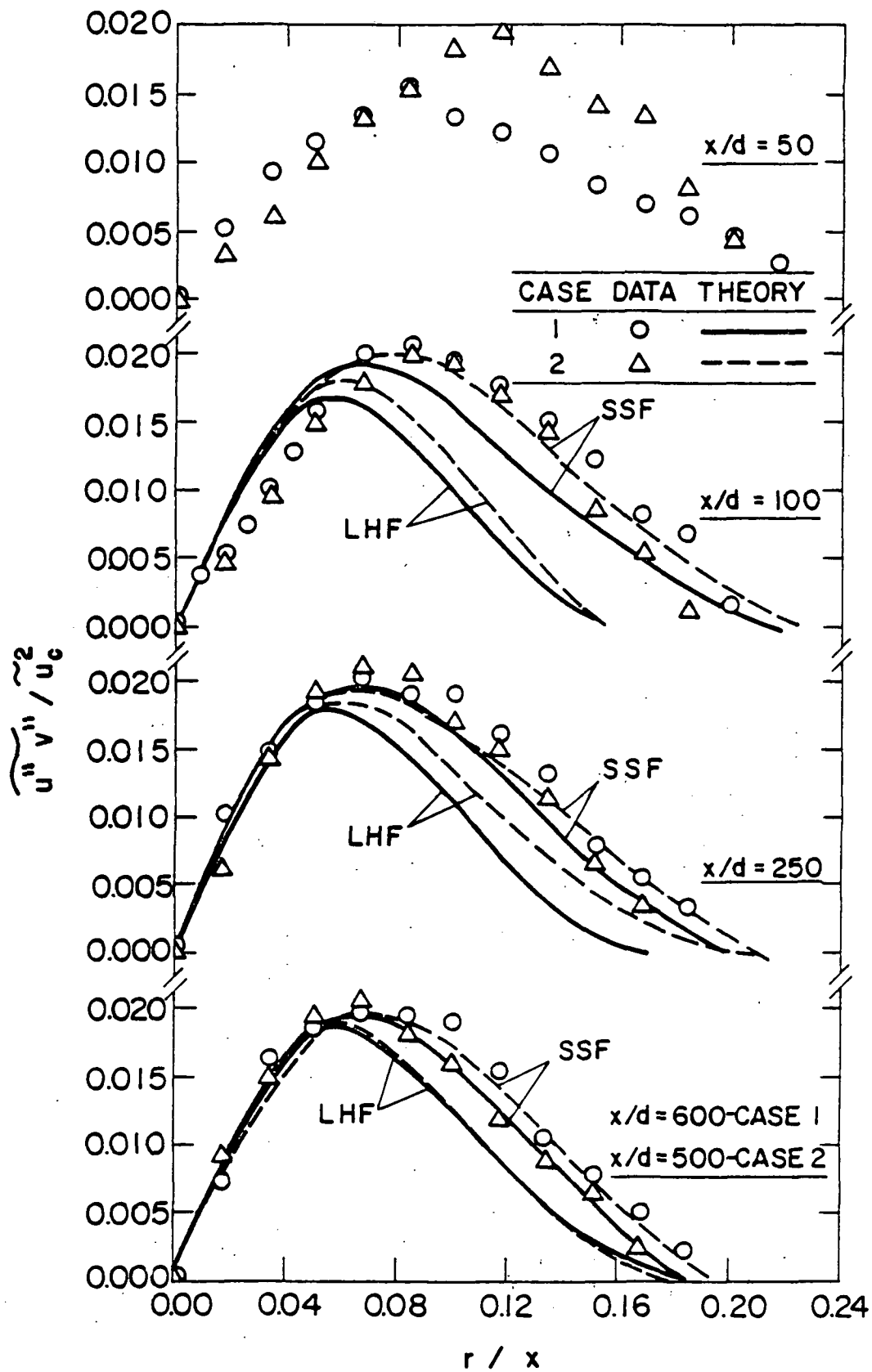


Figure 34. Predicted and measured radial variation of Reynolds stress in their non-evaporating sprays.

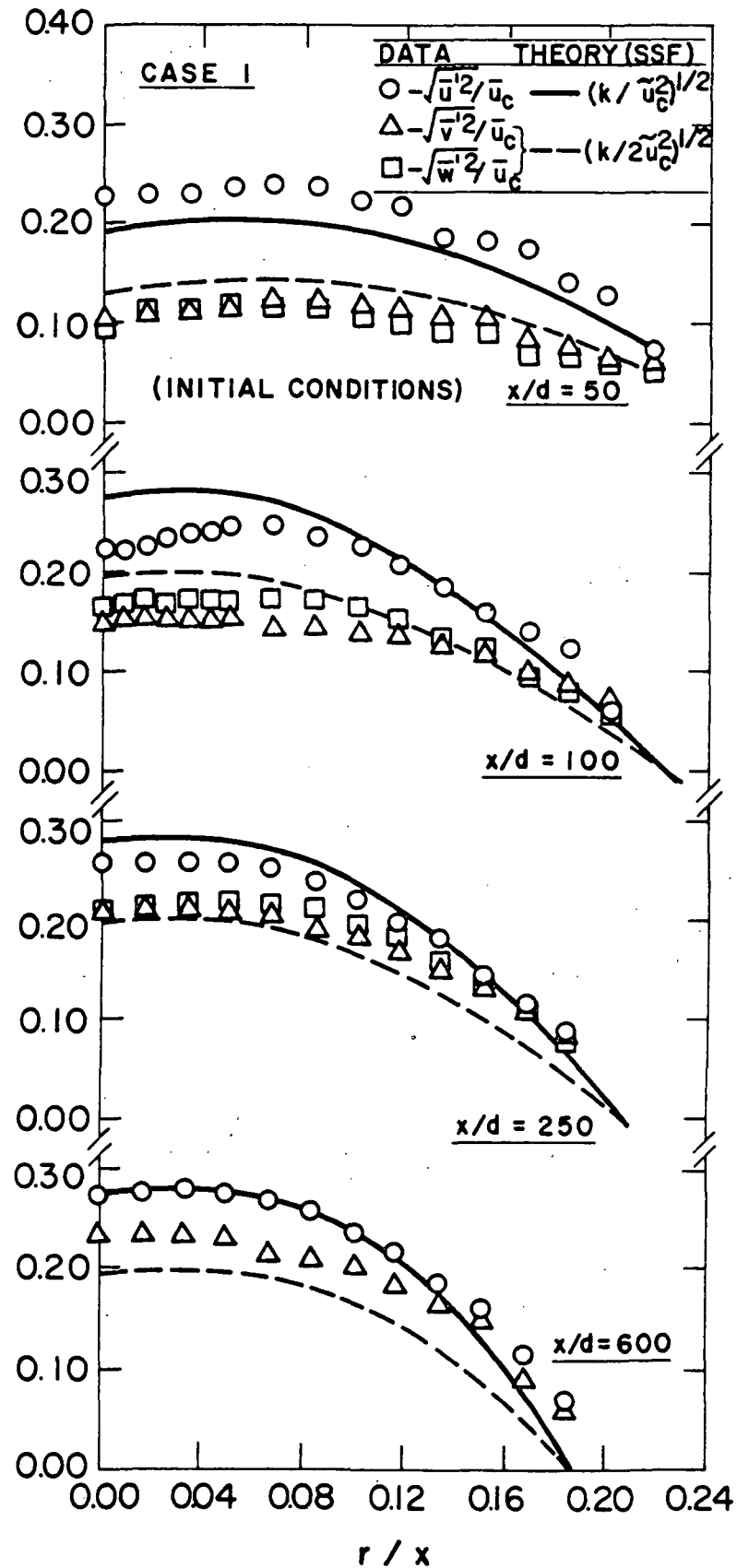


Figure 35. Predicted and measured radial variation of velocity fluctuations for the case 1 nonevaporating spray.

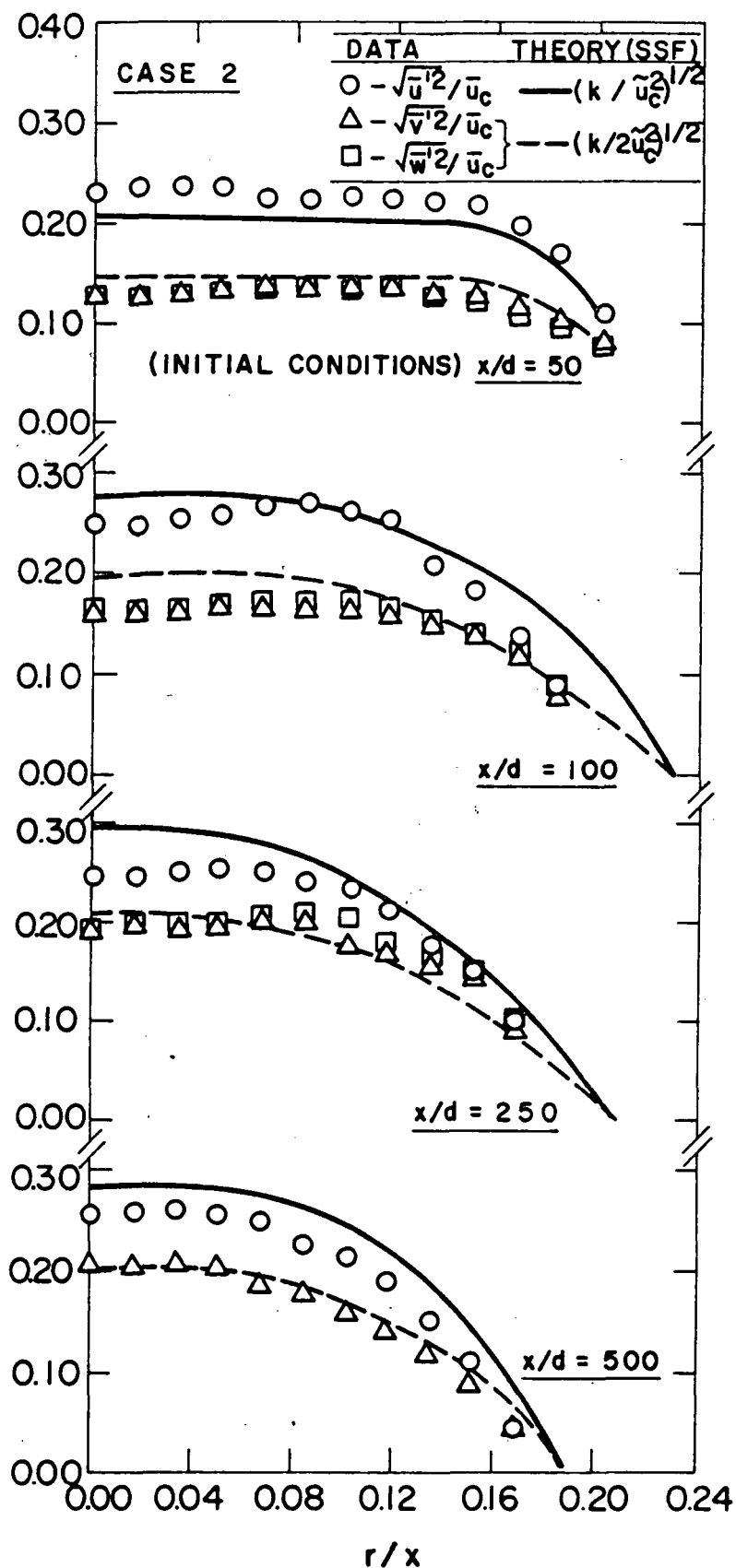


Figure 36. Predicted and measured radial variation of velocity fluctuations for the case 2 nonevaporating spray.

effects of slip are preferentially transmitted into the streamwise velocity component. High levels of anisotropy are also of concern regarding the prescription of eddy properties in the present SSF model, since this approach is based on the assumption of isotropic turbulence. This suggests that multistress models of particle-laden flows might profitably be examined in order to gain more insight concerning effects of particles on turbulence properties.

4.7 Sensitivity Study

Early in the preceding discussion, it was noted that specification of initial conditions is of vital importance to predictions using separated flow models. In the present study, care was exercised in obtaining well-defined initial conditions of all necessary flow properties, at a position as close as possible to the injector exit, viz. $x/d = 50$. However, while measurements of initial conditions of gas-phase mean and turbulence properties were considered sufficiently accurate, initial conditions of mean and fluctuating axial and radial drop velocities were estimated to contain uncertainties that could be beyond acceptable limits of experimental error, especially for the case 2 nonevaporating spray.

Uncertainties exist in the measurements of mean and fluctuating axial drop velocities due to the grouping of data into finite diameter size-ranges and the use of insufficient sample sizes, especially for the larger drops in the size distribution. Moreover, in the case 2 spray, additional uncertainties were introduced by the presence of ligaments, which had to be broken down into drops semiempirically, with mean and fluctuating axial velocities estimated by extrapolation.

Initial conditions of mean and fluctuating radial drop velocities are also of concern. These drop properties were not measured but were estimated from the measured values of the corresponding axial drop velocities and the spray angles.

Due to these uncertainties regarding measurements of initial conditions of drop properties, the sensitivity of the SSF model predictions to the variation of these parameters was examined. The results of this study are presented in Tables 5-7 and Tables 8-10 for the case 1 and case 2 nonevaporating sprays, respectively. The entries show the fractional change in predictions brought about by raising the value of the indicated input parameter by 25%--with all other parameters unchanged. The tables are presented for the major measurement stations considered in the experiments-- $x/d = 100, 250, 500$ and 600.

In general, the predicted flow properties for the gas-phase are not sensitive to the variation of initial conditions of drop velocities. This can be expected, since the model predictions are limited to the dilute portions of the sprays where effects of the dispersed phase on gas-phase properties are very small. On the other hand, the predicted liquid-phase properties show larger sensitivities to variations in the same initial conditions. This finding illustrates the importance of

Table 5. Summary of Results of Sensitivity Study for the Case 1 Nonevaporating Spray at $x/d = 100$

Output Variables	Input Variables			
	\tilde{u}_p	$(\tilde{u}_p^2)^{1/2}$	\tilde{v}_p	$(\tilde{v}_p^2)^{1/2}$
\tilde{u}_c	.01	-.00	-.00	-.00
k_c/\tilde{u}_c^2	.01	-.00	-.00	-.00
\tilde{G}_c	.03	.17	-.08	-.15
SMD_c	-.09	.15	-.14	-.04
\tilde{u}_{p_c}				
$D_p = 20$	-.04	-.05	-.04	-.02
50	.22	.09	.03	.02
90	.31	-.07	.11	-.13

Table 6. Summary of Results of Sensitivity Study for the Case 1 Nonevaporating Spray at $x/d = 250$

Output Variables	Input Variables			
	\tilde{u}_p	$(\tilde{u}_p^2)^{1/2}$	\tilde{v}_p	$(\tilde{v}_p^2)^{1/2}$
\tilde{u}_c	.01	-.00	-.00	-.00
k_c/\tilde{u}_c^2	.00	-.00	-.00	-.00
\tilde{G}_c	.03	.03	-.09	-.11
SMD_c	.03	.03	-.07	.05
\tilde{u}_{p_c}				
$D_p = 20$.01	.02	-.02	.03
50	.06	.04	.04	.02
90	.19	.03	-.01	.00

Table 7. Summary of Results of Sensitivity Study for the Case 1 Nonevaporating Spray at $x/d = 600$

Output Variables	Input Variables			
	\bar{u}_p	$(\bar{u}_p^2)^{1/2}$	\bar{v}_p	$(\bar{v}_p^2)^{1/2}$
\bar{u}_c	.01	.00	.00	.00
k_c/\bar{u}_c^2	.01	.00	-.00	-.00
\bar{G}_c	.15	.25	-.01	-.08
SMD_c	-.01	.04	-.08	-.08
\bar{u}_{p_c}				
$D_p = 20$	-.03	.02	-.01	.01
50	.05	-.00	.03	.01
90	-.02	-.05	-.05	-.03

Table 8. Summary of Results of Sensitivity Study for
the Case 2 Nonevaporating Spray at $x/d = 100$

Output Variables	Input Variables			
	\tilde{u}_p	$(\tilde{u}_p^2)^{1/2}$	\tilde{v}_p	$(\tilde{v}_p^2)^{1/2}$
\tilde{u}_c	.01	~.00	~.00	~.00
k_c/\tilde{u}_c^2	-.01	~.00	~.00	~.00
\tilde{G}_c	.05	-.09	-.26	-.20
SMD_c	-.06	-.06	-.05	-.04
\tilde{u}_{pc}				
$D_p = 20$.03	.02	~.00	~.05
100	.13	.00	~.06	~.06
180	.22	.00	~.00	~.02

Table 9. Summary of Results of Sensitivity Study for the Case 2 Nonevaporating Spray at $x/d = 250$

Output Variables	Input Variables			
	\tilde{u}_p	$(\tilde{u}_p^2)^{1/2}$	\tilde{v}_p	$(\tilde{v}_p^2)^{1/2}$
\tilde{u}_c	.03	~.00	~.00	~.00
k_c/\tilde{u}_c^2	~.00	~.00	~.00	~.00
\tilde{G}_c	.25	.10	-.19	-.19
SMD_c	.04	~.00	-.02	-.02
\tilde{u}_{p_c}				
$D_p = 20$.02	.05	.04	-.03
100	.16	.07	.01	-.03
180	.20	.07	-.16	~.00

Table 10. Summary of Results of Sensitivity Study for
the Case 2 Nonevaporating Spray at $x/d = 500$

Output Variables	Input Variables			
	\tilde{u}_p	$(\tilde{u}_p^2)^{1/2}$	\tilde{v}_p	$(\tilde{v}_p^2)^{1/2}$
\tilde{u}_c	.02	.00	-.00	-.00
k_c/\tilde{u}_c^2	-.06	-.00	-.01	-.01
\tilde{G}_c	.20	-.02	-.08	-.09
SMD_c	.01	-.01	.01	-.02
\tilde{u}_{pc}				
$D_p = 20$	-.02	.01	.05	.05
100	.07	-.02	.03	-.01
180	.16	.04	-.10	.04

defining initial drop properties in order to obtain definitive model evaluation.

Broadly, the most influential parameter for the SSF model predictions is the mean axial drop velocity, while predictions of liquid flux are most sensitive to variations in the initial conditions of drop properties. For example, a 25% change in \bar{G}_c was obtained by raising the value of u_p by 25%. The large influence of u_p is due to the effects of residence times on rates of turbulent dispersion and drop deceleration--especially for the larger drops.

5. SUMMARY AND CONCLUSIONS

5.1 Summary

Comprehensive measurements of the structure of fine and coarse nonevaporating sprays were completed to aid in the understanding of effects of drop size, coalescence, turbulence modulation and turbulent dispersion on spray properties. These measurements included mean and fluctuating gas-phase velocities, liquid fluxes, drop-size distributions and mean and fluctuating axial drop velocities. Initial conditions of spray properties were measured at a location as close to the injector exit as possible, viz. $x/d = 50$, to provide appropriate initial conditions for separated flow models of spray processes.

Measurements of the structure of the nonevaporating sprays were used to evaluate the predictions of three theoretical models, as follows: (1) a locally homogeneous flow (LHF) model, where slip between the phases is neglected; (2) a deterministic separated flow (DSF) model, where interphase slip is considered but turbulent dispersion of particles is neglected; and (3) a stochastic separated flow (SSF) model, where effects of interphase slip, turbulent dispersion and turbulent fluctuations are considered using random sampling for turbulence properties in conjunction with random-walk computations for drop motion.

The theoretical description of the continuous phase for all three models was based upon the Favre-averaged form of the conservation equations written in Eulerian coordinates. The dispersed phase was treated, for the separated flow models, by solving Lagrangian equations of motion for the particles. A modified version of the GENMIX program [25] combined with a second-order Runge-Kutta ordinary differential equation solver for drop motion were used to solve the governing equations.

A sensitivity study was conducted to investigate the influence of uncertainties in specification of initial conditions of drop properties on model predictions. The results are useful in identifying potential sources of error for both predictions and measurements.

5.2 Conclusions

The major conclusions and observations of this study are as follows:

1. The present measurements in nonevaporating sprays showed significant effects of slip between the gas and liquid phases. The rate of development of the coarser spray, having a higher loading ratio, was slower than that of the more finely atomized spray with a lower loading ratio. Present measurements were limited to the dilute portion of the flows, where void fractions were greater than 99.1%. In this region, drop coalescence and major effects of drops on turbulence properties were not observed. As the dense flow region was approached, however, gas-phase turbulent velocity fluctuations exhibited increased anisotropy--suggesting a significant modification of turbulence properties by drops. Additional measurements in the dense spray region would be required to confirm these effects. However, turbulent dispersion of drops was observed as a significant phenomena in both sprays; yielding spray widths that were generally larger than most fully-developed, single-phase jets, and a gradual increase in the SMD along the centerline of the sprays.
2. The LHF model generally overestimated the rate of flow development of the sprays, similar to past experience with this model [13-15]. However, the LHF model underestimated flow widths--unlike the results of earlier work in particle-laden jets [2]. Such enhanced turbulent dispersion of drops, for certain ranges of turbulence and drop properties, is often observed in multiphase flows. The effect was more evident for the present sprays than for the particle-laden jets due to the smaller density of the liquid, which allowed the drops to respond more readily to turbulent fluctuations; and greater initial slip and rates of deceleration in the sprays; due to smaller injector dimensions. Due to the possibility of preferential dispersion under some conditions, it may be concluded that the LHF model does not always provide an upper bound on the rate of development of sprays, as suggested in the past [5]. In spite of these shortcomings, it is felt that the LHF model is still useful as a design tool, since it provides a reasonable first estimate of spray properties with much reduced requirements for defining initial conditions than separated flow models.
3. The DSF model generally underestimated drop dispersion for the present measurements. This approach appears to have limited utility for modeling practical two-phase flows. Gosman and Ioannides [21] note, however, that uncertainties in initial conditions for multiphase flows are potentially a greater source of error than neglecting particle dispersion.
4. In contrast, the SSF model yielded reasonably good results for the present measurements. The SSF model also provided adequate treatment of enhanced drop dispersion in the sprays with no modification of the model from its original calibration (where effects of enhanced dispersion were not observed). While this is encouraging, additional evaluation of the model is

needed--particularly considering improved specifications of initial conditions. The SSF model, which employs assumptions of isotropy performed reasonably well in spite of effects of anisotropy exhibited by measurements near the dense regions of the sprays. However, further consideration of effects of anisotropy, perhaps using a multistress turbulence model, would be desirable. The SSF approach, however, appears to provide an attractive formulation for treating nonlinear interphase transport processes in drop-laden turbulent flows. Current work in this laboratory is considering evaporating sprays in the next phase of the study.

5. In general, present model predictions are relatively insensitive to the specification of gas-phase initial conditions. The specification of drop properties, however, exerts much more pronounced effects on predictions. This emphasizes the importance of measurements of initial condition of drop properties in order to obtain a convincing evaluation of separated flow models. Potential problems in obtaining reliable initial conditions include difficulties in carrying out measurements in the dense spray regions and improved understanding of the atomization process in sprays.

REFERENCES

1. Shuen, J-S., Solomon, A.S.P., Zhang, Q-F. and Faeth, G. M., "The Structure of Particle-Laden Jets and Nonevaporating Sprays," NASA CR-168059, 1983.
2. Shuen, J-S., Chen, L-D. and Faeth, G. M., "Predictions of the Structure of Turbulent, Particle-Laden, Round Jets," AIAA Paper No. 83-0066.
3. Solomon, A.S.P., Shuen, J-S., Zhang, Q-F. and Faeth, G. M., "Measurements and Predictions for Nonevaporating Sprays in a Quiescent Environment," AIAA Paper No. 83-0151.
4. Shuen, J-S., Chen, L-D. and Faeth, G. M., "Evaluation of a Stochastic Model of Particle Dispersion in a Turbulent Round Jet," AICHE J., Vol. 29, 1983, pp. 167-170.
5. Faeth G. M., "Evaporation and Combustion of Sprays," Prog. in Energy and Combust. Sci., Vol. 9, 1983, pp. 1-76.
6. Faeth, G. M., "Recent Advances in Modeling Particle Transport Properties and Dispersion in Turbulent Flow," Proceedings of the ASME-JSME Thermal Engineering Conference, Vol. 2, ASME, New York City, 1983, pp. 517-534.
7. Shuen, J-S., Solomon, A.S.P., Zhang, Q-F. and Faeth, G. M., "A Theoretical and Experimental Study of Turbulent Particle-Laden Jets," NASA CR-168293, 1983.
8. Shuen, J-S., Solomon, A.S.P., Zhang, Q-F. and Faeth, G. M., "Structure of Particle-Laden Jets: Measurements and Predictions," AIAA Paper No. 84-0038, 1984.
9. Modarress, D., Wuerer, J. and Elghobashi, S., "An Experiment Study of a Turbulent Round Two-Phase Jet," AIAA Paper No. 82-0964, 1982.
10. Modarress, D., Tan, H. and Elghobashi, S., "Two-Component LDA Measurement in a Two-Phase Turbulent Jet," AIAA Paper No. 83-0052, 1983.
11. Alpert, R. L. and Mathews, M. K., "Calculation of Large-Scale Flow Fields Induced by Droplet Sprays," Polyphase Flow and Transport Technology, American Society of Mechanical Engineers, New York, 1980, pp. 112-128.
12. Alpert, R. L., "Calculated Interaction of Sprays with Large-Scale Buoyant Flows," ASME Paper No. 82-WA/HT-16, 1982.
13. Yule, A. J., Ah Seng, C., Felton, P. G., Ungut, A. and Chigier, N. A., "A Study of Vaporizing Sprays by Laser Techniques," Combustion and Flame, Vol. 44, 1982, pp. 71-84.

14. Shearer, A. J., Tamura, H. and Faeth, G. M., "Evaluation of a Locally Homogeneous Flow Model of Spray Evaporation," J. of Energy, Vol. 3, September-October 1979, pp. 271-278.
15. Mao, C-P., Szekely, G. A., Jr. and Faeth, G. M., "Evaluation of a Locally Homogeneous Flow Model of Spray Combustion," J. of Energy, Vol. 4, March-April 1980, pp. 78-87.
16. Mao, C-P., Wakamatsu, Y. and Faeth, G. M., "A Simplified Model of High Pressure Spray Combustion," Eighteenth Symposium (International) on Combustion, The Combustion Institute, Pittsburgh, 1981, pp. 337-347.
17. El Banhawy, Y. and Whitelaw, J. H., "Calculation of the Flow Properties of a Confined Kerosene-Spray Flame," AIAA J., Vol. 18, December 1980, pp. 1503-1510.
18. Mongia, H. C. and Smith, K., "An Empirical/Analytical Design Methodology for Gas Turbine Combustors," AIAA Paper No. 78-998, 1978.
19. Boyson, F. and Swithenbank, J., "Spray Evaporation in Recirculating Flow," Seventeenth Symposium (International) on Combustion, The Combustion Institute, Pittsburgh, 1979, pp. 443-453.
20. Yuu, S., Yasukouchi, N., Hirose, Y. and Jotaki, T., "Particle Turbulent Diffusion in a Dust Laden Round Jet," AIChE J., Vol. 24, 1978, pp. 509-519.
21. Gosman, A. D. and Ioannides, E., "Aspects of Computer Simulation of Liquid-Fueled Combustors," AIAA Paper No. 81-0323, 1981.
22. Lockwood, F. C. and Naguib, A. S., "The Prediction of the Fluctuations in the Properties of Free, Round Jet, Turbulent, Diffusion Flames," Combustion and Flame, Vol. 24, 1975, pp. 109-124.
23. Bilger, R. W., "Turbulent Jet Diffusion Flames," Prog. Energy Combust. Sci., Vol. 1, pp. 87-109, 1976.
24. Jeng, S. M. and Faeth, G. M., "Species Concentrations and Turbulence Properties in Buoyant Methane Diffusion Flames," submitted to J. of Heat Transfer.
25. Spalding, D. B., GENMIX: A General Computer Program for Two-Dimensional Parabolic Phenomena, Pergamon Press, Oxford, 1978.
26. McCreath, C. G., Roett, M. F. and Chigier, N. A., "A Technique for Measurement of Velocities and Size of Particles in Flames," J. Physics E: Scientific Instruments, Vol. 5, pp. 601-604, 1972.
27. Szekely, G. A., Jr. and Faeth, G. M., "Reaction of Carbon Black Slurry Agglomerates in Combustion Gases," Nineteenth Symposium

(International) on Combustion, The Combustion Institute, Pittsburgh, pp. 1077-1085, 1982.

28. Lefebvre, A. H., "Airblast Atomization," Prog. Energy Combust. Sci., Vol. 6, pp. 233-261, 1980.
29. Reitz, R. D., "Atomization and Other Breakup Regimes of a Liquid Jet," Ph.D. Thesis 1375-T, Princeton University, 1978.
30. Taylor, G. I., "Generation of Ripples by Wind Blowing over a Viscous Fluid," Collected Works of G. I. Taylor, Vol. 3, 1940.
31. Al Tawell, A. M. and Landau, J., "Turbulence Modulation in Two-Phase Jets," Intl. J. Multiphase Flow, Vol. 3, pp. 341-351, 1977.
32. Wygnanski, I. and Fiedler, H., "Some Measurements in a Self Preserving Jet," Journal of Fluid Mechanics, Vol. 38, pp. 577-612, 1969.
33. Rodi, W., "The Prediction of Free Turbulent Boundary Layers by use of a 2-Equation Turbulence Model," Ph.D. Thesis, University of London, 1972; also cited in Launder, B. E. and Morse, A., "Numerical Prediction of Axisymmetric Free Shear Flows with a Reynolds Stress Closure," Turbulent Shear Flows I, (F. Durst et al., ed.), Springer-Verlag, Berlin, 1979, pp. 279-294.

APPENDIX A

Breakup of Ligaments--Case 2 Nonevaporating Spray, $x/d = 50$

The procedure for the breakup of ligaments observed at $x/d = 50$ in the case 2 nonevaporating spray was adapted from jet breakup theories given in Ref. [29]. Four regimes of jet breakup are identified in Ref. [29], encountered as the injection velocity is progressively increased: (1) Rayleigh jet breakup; (2) first-wind induced breakup; (3) second-wind induced breakup; and (4) atomization regime. These regimes are estimated with the help of the following nondimensional variables:

The Ohnesorge Number: $Z = \mu_L / (\rho_L \sigma_L d_j)^{1/2}$

The Reynolds Number: $Re_L = \rho_L u_j d_j / \mu_L$

The Weber Numbers: $We_L = \rho_L u_j^2 d_j / \sigma_L$

$$We_g = \rho_g u_j^2 d_j / \sigma_L$$

and the ratio of gas to liquid densities, ρ_g / ρ_L . (The Reynolds and Weber numbers are based on jet velocities relative to the surrounding gas velocity).

For conditions at $x/d = 50$ in the case 2 nonevaporating spray, the ligaments were estimated to be primarily in the second-wind induced regime, where droplet formation results from the unstable growth of short wavelength surface waves on the jet surface. The resulting spectrum of drop sizes is less than the original jet diameter. Occasional ligaments were estimated to be in the Rayleigh and first-wind induced regimes, where the resulting drop diameters either exceed or are of the order of the jet diameter. The analyses in the latter two regimes, however, predicted drop sizes to be far greater than the maximum stable drop size observed from photographs taken downstream of $x/d = 50$ in the case 2 nonevaporating spray. Hence, for purposes of estimation, all the ligaments were assumed to undergo second-wind induced breakup.

For the second-wind induced breakup regime, Ref. [29] presents the dispersion relation of Taylor's [30] analysis. Taylor [30] started with the linearized hydrodynamical equations for the liquid jet, and after making some simplifying assumptions, computed the disturbance growth rate to be

$$\omega = 2 \frac{u_j^3}{o_L} (\rho_g^3 / \rho_L)^{1/2} g (\rho_L (Re_L / We_L)^2 \rho_g, x) \quad (A.1)$$

The function $g (\rho_L (Re_L / We_L)^2 \rho_g, x)$ is shown as a function of $\rho_L (Re_L / We_L)^2 \rho_g$ and the wavelength parameter $x = \rho_g u_j^2 / o_L k$ in Fig. 37, where the wave number $k = 2\pi/\lambda$, and λ is the disturbance wavelength (proportional to the eventual droplet sizes). The results in Fig. 37 show the disturbance growth rate to increase with increasing $\rho_L (Re_L / We_L)^2 \rho_g$ and that the maximum growth rate occurs at larger wave numbers (shorter wavelengths) as the group $\rho_L (Re_L / We_L)^2 \rho_g$ increases.

From the photographs at $x/d = 50$, the size and velocity of each of the ligaments were first estimated. Previously measured values of the gas-phase velocities then enabled calculation of the relative velocity and Re_L and We_L . The dispersion relation of Fig. 37 was then used to distribute the sizes over the disturbance wavelength, λ . Downstream of $x/d = 50$ in the case 2 nonevaporating spray, the diameter of the maximum stable droplet was observed to be 190 μm . This condition was then imposed upon the estimated range of disturbance wavelengths, λ , by using a suitable empirical constant. Typical values of the empirical constants varied between 0.36-0.91.

The resulting drops from the ligaments were added to the total number of drops in each size group obtained by ignoring the ligaments, and were assumed to take up the mean and fluctuating axial velocities of that size range. The size distribution at each r/x location was thus rebuilt. The mean and fluctuating axial velocities for drops produced exclusively by the breakup of the ligaments (150-190 μm) were estimated by extrapolating the data of the lower size groups.

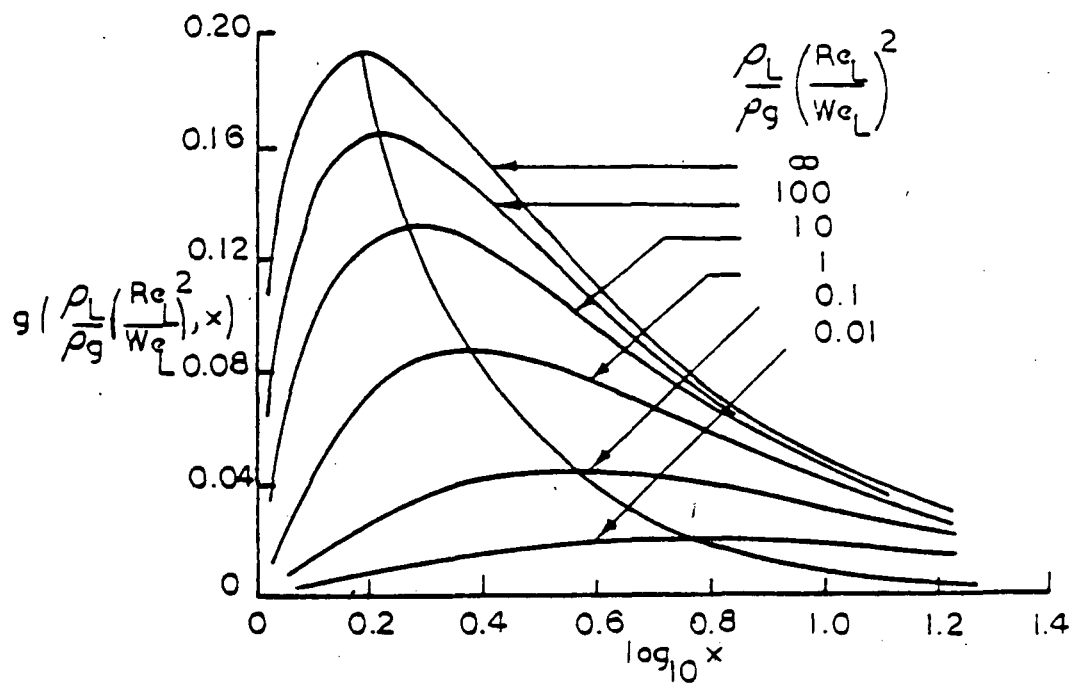


Figure 37. Dispersion relation for second-wind induced breakup from Taylor [30] as presented by Reference [29].

APPENDIX B

DEPTH-OF-FIELD BIAS CORRECTIONS FOR PHOTOGRAPHIC MEASUREMENTS OF DROP SIZE DISTRIBUTIONS

Depth-of-field bias corrections were applied to all photographic measurements of drop sizes in the present study. The depth-of-field in which droplets appear to be in focus in the optical sampling volume increases with increasing drop size. This behavior results in an underestimation of the number of smaller drops since they are counted in a smaller effective sampling volume. A correction is, therefore, necessary so that the relative numbers of droplets for each size group are counted over the same effective sampling volume.

The optical systems used in the present study were calibrated to determine the magnitude of the depth-of-field bias corrections. The calibration was performed by using thermocouple wires with diameters in the range 12.5-254.0 μm . These wires were mounted on a glass slide attached to a unislide, which enabled the wires to be moved in and out of the plane of focus of the optical system. The position of the thermocouple wires was recorded by means of a dial gauge (2.5 μm sensitivity) attached to the unislide. Photographs of the wires were then taken at various positions within the depth-of-field associated with each of the wires. As far as possible, care was taken to use the same lighting and exposure levels as that used for the spray measurements. The depth-of-field associated with each object size was determined from the photographs by defining the depth-of-field to be the distance between the positions where the size of the hazy edges of the image was equal to 10% of the original object size. The results of the calibration for the two optical systems described in Section 3.3.2.2 are illustrated in Figure 38.

The number of droplets counted in each size group was corrected by assuming that the character of the size distribution does not change over the optical path equal to the depth-of-field of the largest measured drop size for each of the test sprays. This assumption is reasonable since the test sprays were axisymmetric and full-cone, and since the largest measured drop size (190 μm) has a relatively small associated depth-of-field, cf., Figure 38.

Let F_i be the depth-of-field corresponding to the i th size group with average diameter d_{p_i} , and n_i be the number of droplets counted in that size group. Then the corrected number of droplets in the i th size group n_{c_i} , is given by

$$n_{c_i} = n_i F_{\text{max}} / F_i \quad (\text{B.1})$$

where F_{max} is the depth-of-field of the largest measured value of d_{p_i} in the size distribution. All photographic measurements of drop size distributions taken in the present study were corrected using Equation (B.1), and represent drop size by number fraction in the spray in a

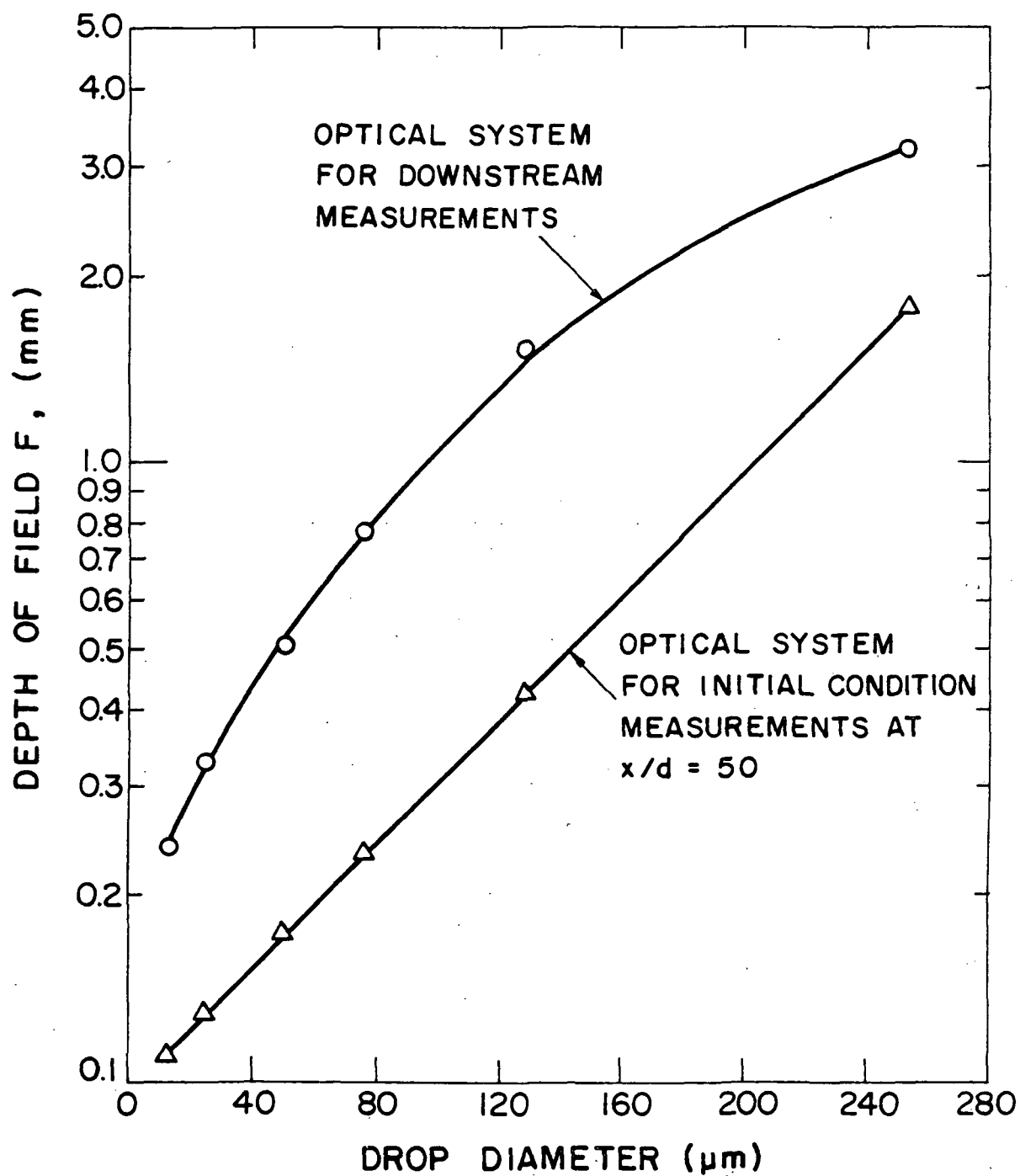


Figure 38. Depth of field versus drop diameter calibration curve for photographic measurement of drop-size distributions.

volume equal to the optical field of view corrected to the depth-of-field for the largest measured value of d_p , e.g., 85 μm and 190 μm for the case 1 and case 2 sprays, respectively. The reported Sauter mean diameters were calculated from these corrected size distributions.

APPENDIX C

Data for the Nonevaporating Spray (Case 1)

C.1 Gas-Phase Properties

Table C.1.1. Axial Variation of Centerline Velocity

x/d	\bar{u}_c / \bar{u}_o
40	0.236
50	0.204
70	0.159
100	0.118
150	0.083
250	0.050
400	0.031
600	0.022

Table C.1.2. Radial Variation of Quantities

$$x/d = 50$$

r/x	\bar{u}/\bar{u}_c	$\overline{u'v'}/\bar{u}_c^2$	$\sqrt{\overline{u'^2}}/\bar{u}_c$	$\sqrt{\overline{v'^2}}/\bar{u}_c$	$\sqrt{\overline{w'^2}}/\bar{u}_c$	\bar{k}/\bar{u}_c^2
0.0	1.0	0.0	0.229	0.104	0.099	.0365
0.017	0.983	.0051	0.231	0.108	0.101	.0375
0.034	0.952	.0091	0.229	0.110	0.112	.0386
0.050	0.886	.0116	0.238	0.113	0.118	.0416
0.067	0.799	.0134	0.239	0.124	0.117	.0431
0.084	0.722	.0153	0.238	0.123	0.112	.0421
0.101	0.654	.0132	0.222	0.116	0.106	.0371
0.117	0.557	.0120	0.221	0.116	0.099	.0359
0.134	0.422	.0104	0.189	0.109	0.089	.0279
0.151	0.357	.0082	0.186	0.108	0.081	.0264
0.168	0.277	.0069	0.178	0.086	0.069	.0220
0.184	0.233	.0060	0.141	0.080	0.064	.0151
0.201	0.180	.0046	0.133	0.066	0.057	.0127
0.218	0.085	.0025	0.075	0.060	0.051	.0059

Table C.1.3. Radial Variation of Quantities

 $x/d = 100$

r/x	\bar{u}/\bar{u}_c	$\overline{u'v'}/\bar{u}_c^2$	$\sqrt{\overline{u'^2}}/\bar{u}_c$	$\sqrt{\overline{v'^2}}/\bar{u}_c$	$\sqrt{\overline{w'^2}}/\bar{u}_c$	\bar{k}/\bar{u}_c^2
0.0	1.0	0.0	0.224	0.147	0.161	.0489
0.008	0.988	.0039	0.224	0.151	0.163	.0496
0.017	0.982	.0053	0.226	0.151	0.173	.0521
0.025	0.961	.0076	0.236	0.150	0.165	.0528
0.034	0.932	.0100	0.240	0.151	0.166	.0541
0.042	0.885	.0127	0.240	0.153	0.169	.0552
0.050	0.832	.0157	0.246	0.156	0.171	.0571
0.067	0.717	.0199	0.247	0.144	0.174	.0559
0.084	0.602	.0202	0.236	0.146	0.172	.0533
0.101	0.515	.0195	0.228	0.141	0.165	.0497
0.117	0.409	.0175	0.209	0.137	0.156	.0433
0.134	0.310	.0149	0.186	0.128	0.138	.0351
0.151	0.243	.0119	0.161	0.116	0.121	.0270
0.168	0.168	.0082	0.142	0.103	0.101	.0205
0.184	0.121	.0068	0.126	0.090	0.086	.0157
0.201	0.059	.0014	0.061	0.072	0.053	.0059

Table C.1.4. Radial Variation of Quantities

 $x/d = 250$

r/x	\bar{u}/\bar{u}_c	$\overline{u'v'}/\bar{u}_c^2$	$\sqrt{\overline{u'^2}}/\bar{u}_c$	$\sqrt{\overline{v'^2}}/\bar{u}_c$	$\sqrt{\overline{w'^2}}/\bar{u}_c$	\bar{k}/\bar{u}_c^2
0.0	1.00	0.0	0.258	0.207	0.209	.0764
0.017	0.981	.0101	0.257	0.209	0.211	.0771
0.034	0.923	.0146	0.257	0.210	0.214	.0781
0.050	0.799	.0185	0.257	0.206	0.216	.0776
0.067	0.709	.0202	0.251	0.207	0.216	.0762
0.084	0.597	.0190	0.239	0.194	0.212	.0698
0.101	0.487	.0189	0.223	0.185	0.198	.0616
0.117	0.389	.0159	0.200	0.169	0.184	.0513
0.134	0.297	.0129	0.181	0.152	0.163	.0411
0.151	0.191	.0079	0.147	0.133	0.142	.0297
0.168	0.146	.0055	0.118	0.109	0.106	.0185
0.184	0.104	.0032	0.091	0.091	0.078	.0112

Table C.1.5. Radial Variation of Quantities

 $x/d = 600$

r/x	\bar{u}/\bar{u}_c	$\overline{u'v'}/\bar{u}_c^2$	$\sqrt{\overline{u'^2}}/\bar{u}_c$	$\sqrt{\overline{v'^2}}/\bar{u}_c$	\bar{k}/\bar{u}_c^2 *
0.0	1.00	0.0	0.272	0.231	.0906
0.017	0.997	.0072	0.277	0.233	.0928
0.034	0.957	.0162	0.281	0.233	.0936
0.050	0.869	.0185	0.274	0.230	.0905
0.067	0.778	.0195	0.269	0.218	.0841
0.084	0.666	.0196	0.259	0.210	.0777
0.101	0.546	.0189	0.237	0.201	.0684
0.117	0.446	.0153	0.219	0.186	.0589
0.134	0.313	.0104	0.187	0.167	.0454
0.151	0.228	.0079	0.163	0.147	.0349
0.168	0.166	.0050	0.116	0.089	.0148
0.184	0.087	.0022	0.070	0.061	.00612

* Calculated assuming $\sqrt{\overline{w'^2}} = \sqrt{\overline{v'^2}}$

C.2 Liquid-Phase Properties

Table C.2.1. Axial Variation of Centerline Liquid Flux

x/d	$\tilde{G}_c/\tilde{G}_o \times 10^3$
40	5.25
50	3.72
70	2.65
100	1.45
150	0.96
250	0.41
400	0.19
600	0.08

C.2.2 Radial Variation of Liquid Flux

r/x	$x/d = 50$	100	250	600
	\bar{G}/\bar{G}_c	\bar{G}/\bar{G}_c	\bar{G}/\bar{G}_c	\bar{G}/\bar{G}_c
0.0	1.00	1.00	1.00	1.00
0.017	--	0.85	0.97	0.97
0.034	0.97	0.80	0.90	0.90
0.050	--	0.77	0.75	0.83
0.067	0.85	0.75	0.65	0.67
0.084	--	0.68	0.44	0.50
0.101	0.73	0.56	0.33	0.32
0.117	--	0.44	0.20	0.21
0.134	0.56	0.38	0.16	0.12
0.151	--	0.29	0.12	0.05
0.168	0.42	0.21	0.05	--
0.184	--	0.15	0.01	--
0.201	0.24	0.08	--	--
0.218	--	0.05	--	--
0.235	0.11	--	--	--
0.268	0.07	--	--	--

Table C.2.3 Radial Variation of Drop Size Distributions at $x/d = 50$
(Slide Impaction Results)

(Entries are Relative Percentage Number Frequency)

Diameter	0.00	6.36	12.72	19.09	25.44	31.80	38.16	44.52	50.88	57.24
Size Range	--	--	--	--	--	--	--	--	--	--
(μm)	6.36	12.72	19.08	25.44	31.80	38.16	44.52	50.88	57.24	63.6
<hr/>										
r/x	0.00	19.95	19.90	18.6	7.8	7.8	2.15	2.15	0.9	0.9
0.00	19.95	19.90	18.6	18.6	7.8	7.8	2.15	2.15	0.9	0.9
0.050	13.4	20.0	31.1	15.1	8.1	4.5	2.1	1.9	1.1	0.65
0.084	8.5	23.3	37.5	13.8	6.3	3.9	2.1	1.3	0.88	0.60
0.117	118.0	34.2	24.5	8.3	5.3	2.6	1.5	1.4	0.92	0.76
0.151	20.6	31.2	16.5	8.7	3.5	2.3	1.6	1.3	0.78	0.54
0.184	27.0	25.1	24.6	9.7	3.8	2.7	1.8	1.1	1.2	0.70
0.218	20.5	51.3	15.6	5.4	2.5	1.7	0.53	0.53	0.23	0.23
0.251	29.6	44.3	14.2	5.7	1.9	0.68	0.68	0.68	0.95	0.27

(Continued)

Table C.2.3. Radial Variation of Drop Size Distributions at $x/d = 50$
(Slide Impaction Results)

(Entries are Relative Percentage Number Frequency)

Diameter	63.60	69.69	76.32	82.68	89.04	95.40	101.8	108.1	114.5
Size Range	--	--	--	--	--	--	--	--	--
(μm)	69.69	76.32	82.68	89.04	95.40	101.8	108.1	114.5	120.8
<hr/>									
r/x									
0.00	0.37	0.37	0.11	0.11	0.08	0.08	0.02	0.02	0.00
0.050	0.32	0.29	0.19	0.23	0.10	0.03	0.06	0.06	0.06
0.084	0.35	0.25	0.11	0.18	0.21	0.14	0.14	0.14	0.14
0.117	0.32	0.36	0.28	0.08	0.32	0.28	0.20	0.00	0.12
0.151	0.49	0.44	0.49	0.19	0.39	0.19	0.00	0.00	0.00
0.184	0.39	0.47	0.31	0.39	0.00	0.23	0.16	0.00	0.08
0.218	0.15	0.15	0.23	0.08	0.15	0.23	0.08	0.00	0.08
0.251	0.27	0.00	0.00	0.27	0.14	0.00	0.00	0.27	0.00

Table C.2.4. Radial Variation of SMD at $x/d = 50$
(Slide Impaction Results)

x/d	SMD (μm)
0.00	40.6
0.050	41.8
0.084	46.2
0.117	50.7
0.151	49.3
0.184	49.4
0.218	43.6
0.251	47.6

Table C.2.5. Radial Variation of Drop Size Distributions at $x/d = 50$
for the Case 1 Nonevaporating Spray (Photographic Results)

(Entries are Relative Percentage Number Frequency)

Diameter	15	20	25	30	35	40	45	50	55	60	65	70
Size Range	--	--	--	--	--	--	--	--	--	--	--	--
(μm)	20	25	30	35	40	45	50	55	60	65	70	75
<hr/>												
r/x												
0.00	21.9	22.5	16.5	12.0	8.8	6.7	4.1	2.8	1.7	1.9	0.9	0.3
0.05	25.4	22.9	15.6	11.5	8.5	5.5	3.7	1.9	2.7	1.0	0.8	0.5
0.10	24.9	20.5	14.6	10.1	7.6	5.9	6.2	3.9	2.6	1.8	1.3	0.6
0.15	23.0	17.8	15.9	11.6	8.4	6.0	5.6	3.5	4.2	2.1	1.2	0.7
0.20	28.5	18.7	17.1	10.7	6.4	4.1	3.9	4.1	2.2	2.7	1.1	0.6

Table C.2.6. Radial Variation of SMD at $x/d = 50$
in the Case 1 Nonevaporating Spray
(Photographic Results)

x/d	SMD (μm)
0.00	39.9
0.05	39.4
0.10	42.2
0.15	43.0
0.20	41.9

Table C.2.7. Initial Conditions of Mean Axial Drop Velocities (m/s)
at $x/d = 50$ for the Case 1 Nonevaporating Spray

r/x	0.00	0.05	0.10	0.15	0.20
Diameter Size Range (μm)					
15-25	26.7	20.4	9.0	3.2	0.55
25-35	33.4	24.6	11.8	4.5	1.30
35-45	40.6	29.5	15.6	7.5	1.95
45-55	40.6	29.5	15.6	7.5	1.95
55-65	42.9	29.6	17.0	9.2	5.09
65-75	46.4	30.5	20.7	12.1	9.59

Table C.2.8. Initial Conditions of Fluctuating Axial Drop Velocities (m/s) at $x/d = 50$ for the Case 1 Nonevaporating Spray

r/x	0.00	0.05	0.10	0.15	0.20
Diameter Size Range (μm)					
15-25	6.7	7.7	5.5	3.1	1.02
25-35	10.9	10.5	4.6	2.9	1.58
35-45	13.3	10.5	7.9	5.7	1.78
45-55	14.3	8.0	8.3	5.6	2.76
55-65	14.7	8.7	8.9	4.8	4.40
65-75	18.2	11.9	9.8	6.8	5.03

Table C.2.9. Axial Variation of Drop-Size Distributions Along the Centerline of the Case 1 Nonevaporating Spray (Photographic Results).

(Entries are Relative Percentage Number Frequency)

Diameter Size Range (μm)	15	20	25	30	35	40	45	50	55	60	65	70	75	80
	--	--	--	--	--	--	--	--	--	--	--	--	--	--
	20	25	30	35	40	45	50	55	60	65	70	75	80	85
<hr/>														
x/d														
100	9.2	18.5	23.6	15.8	9.2	6.6	4.9	4.2	3.5	2.6	1.1	0.9	--	--
150	6.1	11.9	19.5	15.7	12.3	10.1	7.8	6.1	4.2	2.5	1.8	1.3	0.7	--
250	15.8	19.1	18.2	13.3	9.8	6.9	4.2	3.5	3.2	2.0	1.9	1.3	0.9	--
400	21.7	19.5	12.9	10.0	7.7	6.2	4.1	3.6	3.6	2.8	2.6	2.6	1.9	0.9
600	19.3	20.9	15.4	10.2	7.5	5.4	3.9	3.5	3.2	2.6	2.9	1.9	1.9	1.4

Table C.2.10. Axial Variation of SMD along
the Centerline of the Case 1
Nonevaporating Spray
(Photographic Results)

x/d	SMD (μm)
100	42.9
150	46.3
250	45.2
400	51.0
600	51.1

Table C.2.11. Mean Axial Drop Velocities (m/s) along the Centerline for the Case 1 Nonevaporating Spray

x/d	100	150	250	400	600
Diameter Size Range (μm)					
15-25	14.2	8.9	6.5	4.4	2.7
25-35	17.0	11.3	7.7	5.0	2.9
35-45	20.9	12.7	8.1	5.1	3.0
45-55	23.0	14.6	8.3	5.7	3.3
55-65	24.6	14.4	9.0	5.5	3.1
65-75	28.5	15.5	8.5	5.3	3.2
75-85	--	20.1	9.0	5.4	3.2

Table G.2.12. Fluctuating Axial Drop Velocities (m/s) along the Centerline for the Case 1 Nonevaporating Spray

x/d	100	150	250	400	600
Diameter Size Range (μm)					
15-25	4.3	3.1	1.8	1.3	0.79
25-35	4.8	3.0	1.6	1.3	0.84
35-45	7.7	3.6	1.6	1.2	0.85
45-55	9.3	5.0	2.0	1.1	0.82
55-65	12.3	5.8	2.3	1.2	0.89
65-75	14.1	6.6	3.1	1.5	0.92
75-85	--	7.1	3.5	1.4	0.83

Table C.2.13. Radial Variation of Drop-Size Distributions at $x/d = 250$
for the Case 1 Nonevaporating Spray (Photographic Results)

(Entries are Relative Percentage Number Frequency)

Diameter Size Range (μm)	15	20	25	30	35	40	45	50	55	60	65	70	75	80	85
	--	--	--	--	--	--	--	--	--	--	--	--	--	--	--
20	20	25	30	35	40	45	50	55	60	65	70	75	80	85	
<hr/>															
r/x															
0.034	24.3	17.8	15.1	12.2	9.7	6.0	3.6	3.3	3.1	2.1	1.2	0.9	0.6	0.4	
0.067	30.2	19.4	15.0	12.5	9.3	2.7	2.4	2.5	1.9	1.4	1.0	0.7	0.6	0.4	
0.101	32.1	18.3	14.6	12.2	8.4	3.6	2.2	2.2	1.6	0.9	0.8	0.8	1.2	1.3	
0.134	37.7	18.5	12.5	7.9	7.8	3.4	2.2	2.3	2.1	1.5	1.0	1.1	1.0	1.0	
0.168	47.0	16.5	8.6	6.7	6.2	3.1	1.8	2.2	1.6	1.7	1.2	1.4	1.0	1.1	

Table C.2.14. Radial Variation of SMD at $x/d = 250$
for the Case 1 Nonevaporating Spray
(Photographic Results)

r/x	SMD (μm)
0.034	44.4
0.067	42.2
0.101	44.9
0.134	45.6
0.168	46.7

Table C.2.15. Radial Variation of Mean Axial Drop Velocities (m/s)
at $x/d = 250$ for the Case 1 Nonevaporating Spray

r/x	0.034	0.067	0.101	0.134	0.168
Diameter Size Range (μm)					
15-25	6.6	4.2	2.6	1.4	0.7
25-35	6.9	5.0	3.4	1.7	0.9
35-45	7.1	4.8	3.6	1.9	0.8
45-55	7.2	5.2	3.5	1.8	1.0
55-65	7.7	4.9	3.9	2.3	1.3
65-75	7.5	5.0	4.0	1.8	1.0
75-85	8.1	6.3	4.0	2.1	1.3

Table C.2.16. Radial Variation of Fluctuating Axial Drop Velocities
(m/s) at $x/d = 250$ for the Case 1 Nonevaporating Spray

r/x	0.034	0.067	0.101	0.134	0.168
Diameter Size Range (μm)					
15-25	1.38	1.60	1.19	0.86	0.53
25-35	1.50	1.84	1.62	0.90	0.74
35-45	1.65	1.95	1.77	1.21	0.70
45-55	1.40	1.62	1.64	1.18	0.76
55-65	1.58	1.92	1.72	1.44	0.91
65-75	1.90	1.88	1.87	1.07	0.67
75-85	1.87	2.28	1.92	1.87	0.91

Table C.2.17. Collection Efficiencies for Liquid Mass
Flux Data Obtained by Isokinetic Sampling
at Major Axial Measurement Stations

x/d	Percent of Injector Mass Flow Rate Collected
50	97.5
100	97.6
250	93.7
600	99.0

APPENDIX D

Data for the Nonevaporating Spray (Case 2)

D.1 Gas-Phase Properties

Table D.1.1. Axial Variation of Centerline Velocity

x/d	\bar{u}_c / \bar{u}_o
40	0.490
50	0.447
70	0.338
100	0.249
150	0.182
250	0.118
400	0.078
500	0.066
600	0.060

Table D.1.2. Radial Variation of Quantities

$$x/d = 50$$

r/x	\bar{u}/\bar{u}_c	$\overline{u'v'}/\bar{u}_c^2$	$\sqrt{\overline{u'^2}}/\bar{u}_c$	$\sqrt{\overline{v'^2}}/\bar{u}_c$	$\sqrt{\overline{w'^2}}/\bar{u}_c$	\bar{k}/\bar{u}_c^2
0.0	1.000	0.0	0.228	0.125	0.126	.0416
0.017	0.998	.0034	0.234	0.127	0.126	.0434
0.034	0.956	.0060	0.236	0.128	0.127	.0441
0.050	0.924	.0103	0.235	0.132	0.130	.0448
0.067	0.829	.0132	0.222	0.134	0.132	.0422
0.084	0.773	.0152	0.222	0.136	0.133	.0429
0.101	0.693	.0179	0.226	0.136	0.133	.0434
0.117	0.614	.0196	0.222	0.134	0.130	.0420
0.134	0.550	.0166	0.220	0.129	0.128	.0408
0.151	0.462	.0140	0.216	0.127	0.122	.0388
0.168	0.391	.0133	0.198	0.114	0.105	.0316
0.184	0.148	.0041	0.110	0.081	0.078	.0124

Table D.1.3. Radial Variation of Quantities

 $x/d = 100$

r/x	\bar{u}/\bar{u}_c	$\overline{u'v'}/\bar{u}_c^2$	$\sqrt{\overline{u'^2}}/\bar{u}_c$	$\sqrt{\overline{v'^2}}/\bar{u}_c$	$\sqrt{\overline{w'^2}}/\bar{u}_c$	\bar{k}/\bar{u}_c^2
0.0	1.000	0.00	0.248	0.157	0.163	.0564
0.017	0.998	.0046	0.247	0.159	0.159	.0558
0.034	0.972	.0096	0.252	0.161	0.162	.0576
0.050	0.899	.0149	0.258	0.164	0.166	.0605
0.067	0.836	.0179	0.266	0.166	0.171	.0637
0.084	0.745	.0199	0.269	0.164	0.172	.0645
0.101	0.656	.0192	0.259	0.162	0.172	.0613
0.117	0.548	.0169	0.252	0.156	0.166	.0576
0.134	0.447	.0142	0.208	0.149	0.155	.0447
0.151	0.333	.0086	0.181	0.138	0.141	.0359
0.168	0.159	.0054	0.138	0.117	0.121	.0237
0.184	0.113	.0010	0.089	0.076	0.088	.0108

Table D.1.4. Radial Variation of Quantities

 $x/d = 250$

r/x	\bar{u}/\bar{u}_c	$\overline{u'v'}/\bar{u}_c^2$	$\sqrt{\overline{u'^2}}/\bar{u}_c$	$\sqrt{\overline{v'^2}}/\bar{u}_c$	$\sqrt{\overline{w'^2}}/\bar{u}_c$	\bar{k}/\bar{u}_c^2
0.0	1.000	0.00	0.246	0.192	0.189	.0663
0.017	0.983	.0061	0.248	0.196	0.197	.0694
0.034	0.923	.0141	0.251	0.193	0.199	.0700
0.050	0.863	.0192	0.253	0.195	0.198	.0706
0.067	0.739	.0209	0.251	0.201	0.203	.0722
0.084	0.644	.0203	0.241	0.203	0.209	.0716
0.101	0.517	.0169	0.234	0.177	0.203	.0636
0.117	0.453	.0149	0.211	0.169	0.181	.0530
0.134	0.336	.0113	0.176	0.154	0.167	.0414
0.151	0.199	.0067	0.149	0.146	0.150	.0331
0.168	0.121	.0035	0.099	0.090	0.101	.0141

Table D.1.5. Radial Variation of Quantities

 $x/d = 500$

r/x	\bar{u}/\bar{u}_c	$\overline{u'v'}/\bar{u}_c^2$	$\sqrt{\overline{u'^2}}/\bar{u}_c$	$\sqrt{\overline{v'^2}}/\bar{u}_c$	\bar{k}/\bar{u}_c^2 *
0.0	1.000	0.0	0.255	0.204	.0742
0.017	0.985	.0091	0.258	0.202	.0741
0.034	0.939	.0148	0.261	0.207	.0768
0.050	0.866	.0194	0.254	0.205	.0745
0.067	0.813	.0206	0.246	0.187	.0652
0.084	0.646	.0180	0.224	0.180	.0575
0.101	0.532	.0160	0.214	0.159	.0483
0.117	0.365	.0118	0.190	0.140	.0378
0.134	0.251	.0089	0.150	0.119	.0257
0.151	0.163	.0063	0.110	0.088	.0138
0.168	0.069	.0024	0.045	0.046	.0032

* Calculated assuming $\sqrt{\overline{w'^2}} = \sqrt{\overline{v'^2}}$

D.2 Liquid-Phase Properties

Table D.2.1. Axial Variation of Centerline Liquid Flux

x/d	$\bar{G}_c/\bar{G}_o \times 10^3$
40	3.24
50	2.13
70	1.34
100	0.99
150	0.50
250	0.25
400	0.12
500	0.076

Table D.2.2 Radial Variation of Liquid Flux

r/x	$x/d = 50$	100	250	600
	\tilde{G}/\tilde{G}_c	\tilde{G}/\tilde{G}_c	\tilde{G}/\tilde{G}_c	\tilde{G}/\tilde{G}_c
0.0	1.00	1.00	1.00	1.00
0.017	--	1.01	0.99	0.98
0.034	0.97	0.99	0.87	0.92
0.050	--	0.88	0.80	0.85
0.067	0.99	0.81	0.70	0.80
0.084	--	0.76	0.52	0.68
0.101	0.88	0.63	0.43	0.55
0.117	--	0.57	0.32	0.39
0.134	0.80	0.45	0.27	0.27
0.151	--	0.37	0.20	0.20
0.168	0.62	0.31	0.16	0.12
0.184	--	0.26	0.14	--
0.201	0.44	0.20	0.10	--
0.218	--	0.16	0.07	--
0.235	0.31	--	--	--
0.268	0.18	--	--	--
0.302	0.11	--	--	--

Table D.2.3 Radial Variation of Drop Size Distributions at $x/d = 50$
(Slide Impaction Results)

(Entries are Relative Percentage Number Frequency)

Diameter	0.00	6.36	12.72	19.08	25.44	31.80	38.16	44.52	50.88	57.24	63.60
Size Range	--	--	--	--	--	--	--	--	--	--	--
(μm)	6.36	12.72	19.08	25.44	31.80	38.16	44.52	50.88	57.24	63.60	69.96
<hr/>											
r/x											
0.00	0.0	10.1	33.9	16.8	8.1	5.7	5.3	3.0	1.0	0.67	1.0
0.050	0.0	3.1	19.5	23.2	12.2	7.3	5.7	5.3	3.4	1.5	2.3
0.084	0.0	4.9	22.1	17.2	12.9	9.2	6.7	4.3	1.2	3.1	2.5
0.117	0.0	8.8	21.7	11.2	14.3	8.1	8.1	6.8	1.9	0.6	2.5
0.151	0.0	9.4	16.4	10.9	14.1	10.9	4.7	8.6	2.3	5.5	2.3
0.184	0.0	41.8	28.4	6.0	4.5	0.0	2.9	0.0	2.9	2.9	0.0
0.218	0.0	41.8	28.4	6.0	4.5	0.0	2.9	0.0	2.9	2.9	0.0

(Continued)

Table D.2.3 Radial Variation of Drop Size Distributions at $x/d = 50$
(Slide Impaction Results)

(Entries are Relative Percentage Number Frequency)

Diameter	69.69	76.32	82.68	89.04	95.40	101.8	108.1	114.5	120.8	127.2	133.6
Size Range	--	--	--	--	--	--	--	--	--	--	--
(μm)	76.32	82.68	89.04	95.40	101.8	108.1	114.5	120.8	127.2	133.6	139.9
<hr/>											
r/x											
0.00	1.6	2.6	1.0	1.3	0.7	0.7	0.7	0.3	1.3	0.3	1.0
0.050	3.8	0.8	1.9	1.1	1.1	0.8	0.8	0.4	1.5	1.1	0.0
0.084	0.0	1.3	1.3	0.6	1.3	1.3	0.6	0.0	1.3	0.6	0.6
0.117	1.2	0.62	2.5	0.0	1.9	1.2	0.6	0.6	0.0	0.6	0.0
0.151	0.0	0.78	3.1	1.6	1.6	1.6	1.6	0.0	0.8	0.0	0.0
0.184	5.7	0.0	5.7	1.4	0.0	0.0	1.4	0.0	0.0	1.4	0.0
0.218	4.5	0.0	4.5	0.0	0.0	0.0	0.0	0.0	0.0	0.0	0.0

(Continued)

Table D.2.3. Radial Variation of Drop Size Distributions at $x/d = 50$
(Slide Impaction Results)

(Entries are Relative Percentage Number Frequency)

Diameter	139.9	146.3	152.6	159.0	165.4	171.7	178.1	184.4	198.8	197.2
Size Range	--	--	--	--	--	--	--	--	--	--
(μm)	146.3	152.6	159.0	165.4	171.7	178.1	184.4	190.8	197.2	203.5
<hr/>										
r/x										
0.00	0.7	0.0	1.0	0.3	0.0	0.3	0.0	0.3	0.0	0.3
0.050	0.4	0.4	0.0	0.4	0.0	0.4	0.4	0.4	0.0	0.8
0.084	0.6	0.6	0.0	0.6	0.0	0.0	0.0	1.2	1.2	0.0
0.117	0.6	1.2	0.6	0.6	0.0	0.6	1.9	0.0	1.2	0.0
0.151	0.8	0.8	0.8	0.8	0.0	0.8	0.0	0.0	0.0	0.8
0.184	0.0	1.4	1.4	0.0	0.0	0.0	0.0	0.0	0.0	1.4
0.218	0.0	0.0	0.0	1.5	0.0	0.0	0.0	0.0	0.0	0.0

Table D.2.4. Radial Variation of SMD at $x/d = 50$
(Slide Impaction Results)

r/x	SMD (μm)
0.00	111.1
0.050	109.3
0.084	116.6
0.117	126.9
0.151	100.8
0.184	112.1
0.218	91.1

Table D.2.5 Radial Variation of Drop-Size Distributions at
 $x/d = 50$ for the Case 2 Nonevaporating Spray
 (Photographic Results--Corrected for Ligaments)

(Entries are Relative Percentage Number Frequency)

Diameter	10	20	30	40	50	60	70	80	90	100	110	120	130	140	150	160	170	180
Size Range	--	--	--	--	--	--	--	--	--	--	--	--	--	--	--	--	--	--
(μm)	20	30	40	50	60	70	80	90	100	110	120	130	140	150	160	170	180	190
<hr/>																		
r/x	-																	
0.00	31.8	24.8	11.2	7.5	5.7	4.7	4.5	3.1	2.1	1.7	1.2	1.0	.57	.17	.04	.03	0.0	0.0
0.05	34.0	22.0	11.3	7.4	5.7	4.4	4.2	3.1	2.3	1.9	1.4	1.1	.62	.36	.22	.07	.02	0.0
0.10	30.0	25.3	11.3	8.7	5.0	4.3	3.7	2.9	2.4	2.0	1.5	1.1	.82	.49	.36	.24	.08	.02
0.15	30.2	23.4	13.1	7.6	5.2	4.2	3.9	3.0	2.4	2.2	1.6	1.1	.84	.45	.37	.21	.13	.02
0.20	33.3	18.6	15.3	8.0	5.7	3.9	3.3	2.9	2.5	1.8	1.6	1.1	.78	.46	.34	.21	.06	.01

Table D.2.6 Radial Variation of SMD at $x/d = 50$
in the Case 2 Nonevaporating Spray
(Photographic Results--Corrected
for Ligaments)

r/x	SMD (μm)
0.00	79.8
0.05	83.6
0.10	88.6
0.15	89.0
0.20	87.4

Table D.2.7. Initial Conditions of Mean Axial Drop Velocities (m/s)
at $x/d = 50$ for the Case 2 Nonevaporating Spray

r/x	0.00	0.05	0.10	0.15	0.20
Diameter Size Range (μm)					
10-30	16.7	13.2	9.9	5.9	2.7
30-50	21.7	18.1	14.6	8.2	4.0
50-70	26.2	21.4	18.4	15.0	8.7
70-90	26.3	23.6	20.6	14.4	10.6
90-110	28.3	23.6	20.2	17.5	13.0
110-130	28.4	27.2	19.8	18.8	12.0
130-150	27.5	25.0	22.6	17.5	12.5
150-170	26.5	24.6	22.0	17.5	11.5
170-190	25.0	24.2	21.6	17.1	10.0

Table D.2.8. Initial Conditions of Fluctuating Axial Drop Velocities (m/s) at $x/d = 50$ for the Case 2 Nonevaporating Spray

r/x	0.00	0.05	0.10	0.15	0.20
Diameter Size Range (μm)					
10-30	4.2	4.7	4.4	3.1	2.0
30-50	6.5	6.3	6.6	5.4	3.2
50-70	5.4	5.4	5.2	5.7	4.9
70-90	4.8	5.2	6.4	5.6	4.9
90-110	3.6	6.3	3.2	3.3	3.5
110-130	5.2	3.7	6.0	3.7	6.3
130-150	5.7	6.6	7.3	6.8	7.0
150-170	5.5	6.5	7.2	6.8	6.4
170-190	5.2	6.4	7.0	6.7	5.6

Table D.2.9. Axial Variation of Drop-Size Distributions Along the Centerline of the Case 2 Nonevaporating Spray (Photographic Results)

(Entries are Relative Percentage Number Frequency)

Diameter	10	20	30	40	50	60	70	80	90	100	110	120	130	140	150	160	170	180
Size Range	--	--	--	--	--	--	--	--	--	--	--	--	--	--	--	--	--	--
(μm)	20	30	40	50	60	70	80	90	100	110	120	130	140	150	160	170	180	190
x/d																		
100	19.8	30.5	19.6	18.7	4.7	2.5	1.7	.71	.50	.30	.22	.29	.13	.08	.11	.07	.10	.06
150	24.2	25.3	18.1	16.1	7.3	3.3	2.4	1.1	.55	.52	.30	.27	.18	.09	.12	.07	.07	.03
250	22.8	26.1	17.5	13.6	7.3	5.1	3.1	1.8	.83	.46	.29	.43	.19	.21	.16	.11	.06	.03
400	22.3	26.5	17.9	13.4	5.1	4.8	3.4	2.2	1.2	.94	.84	.38	.56	.26	.12	.07	.04	.04
600	25.1	25.7	14.6	10.7	6.1	5.5	4.1	2.5	1.9	1.3	.60	.47	.36	.30	.25	.28	.18	.08

Table D.2.10. Axial Variation of SMD Along the Center-
line of the Case 2 Nonevaporating Spray
(Photographic Results)

x/d	SMD (μm)
100	62.1
150	64.2
250	68.8
400	73.8
500	81.1

Table D.2.11. Mean Axial Drop Velocities (m/s) Along the Axis of the Case 2 Nonevaporating Spray

x/d	100	150	250	400	600
Diameter Size Range (μm)					
10-30	9.3	6.9	5.2	3.5	2.4
30-50	10.5	7.5	5.6	3.7	2.6
50-70	13.5	8.5	5.6	3.9	2.7
70-90	19.0	12.1	6.0	3.9	2.8
90-110	22.6	14.1	7.7	3.8	2.8
110-130	22.1	18.9	7.2	4.5	2.7
130-150	24.2	21.1	8.7	5.5	2.9
150-170	23.4	20.2	9.1	6.4	2.9
170-190	21.6	20.7	12.4	8.0	4.4

Table D.2.12. Fluctuating Axial Drop Velocities (m/s) Along the Axis of the Case 2 Nonevaporating Spray

<u>x/d</u>	100	150	250	400	600
Diameter Size Range (μm)					
10-30	2.10	1.37	1.02	0.78	0.59
30-50	2.81	1.45	1.02	0.77	0.63
50-70	4.37	2.19	0.95	0.77	0.58
70-90	3.38	3.71	1.43	0.72	0.53
90-110	2.24	4.72	2.20	0.81	0.42
110-130	2.59	2.67	2.36	0.93	0.41
130-150	2.93	4.65	2.17	1.49	0.69
150-170	2.83	3.40	3.56	1.77	0.88
170-190	2.24	2.85	3.09	3.42	1.04

Table D.2.13. Radial Variation of Drop-Size Distributions at $x/d = 250$
for the Case 2 Nonevaporating Spray (Photographic Results)

(Entries are Relative Percentage Number Frequency)

Diameter	10	20	30	40	50	60	70	80	90	100	110	120	130	140	150	160	170	180
Size Range	--	--	--	--	--	--	--	--	--	--	--	--	--	--	--	--	--	--
(μm)	20	30	40	50	60	70	80	90	100	110	120	130	140	150	160	170	180	190
r/x																		
0.034	24.8	27.0	20.5	8.5	6.9	5.7	2.4	1.2	1.5	.30	.30	.40	.22	.14	.18	.13	.08	.07
0.067	35.2	27.3	16.8	5.4	5.4	3.4	1.7	1.2	1.7	.46	.41	.31	.15	.19	.08	.04	.04	.03
0.101	30.6	28.9	16.1	6.9	5.3	4.9	1.8	.81	1.8	.92	1.0	.44	.27	.05	.09	.08	--	.04
0.134	33.8	31.0	15.4	5.5	3.2	2.6	2.3	1.5	1.4	.85	.90	.80	.49	.05	.15	.04	.04	.04
0.168	29.1	27.1	18.6	7.0	3.0	3.0	2.2	2.0	2.5	1.5	1.5	1.4	.70	--	.30	--	--	.11

Table D.2.14. Radial Variation of SMD at $x/d = 250$
for the Case 2 Nonevaporating Spray
(Photographic Results)

r/x	SMD (μm)
0.034	70.4
0.067	68.2
0.101	75.4
0.134	76.0
0.168	83.7

Table D.2.15. Radial Variation of Mean Axial Drop Velocities (m/s)
at $x/d = 250$ for the Case 2 Nonevaporating Spray

r/x	0.034	0.067	0.101	0.134	0.168
Diameter Size Range (μm)					
10-30	4.5	3.3	2.0	1.5	0.6
30-50	4.9	3.7	2.2	1.7	0.8
50-70	5.1	3.5	2.3	1.6	0.9
70-90	5.4	4.2	2.5	1.7	0.8
90-110	6.5	4.6	2.6	2.0	0.8
110-130	8.5	6.2	3.0	2.3	1.1
130-150	9.6	7.9	3.9	4.3	0.8
150-170	11.2	7.3	6.8	4.0	2.0
170-190	13.1	10.0	9.2	6.8	6.9

Table D.2.16. Radial Variation of Fluctuating Axial Velocities (m/s)
at $x/d = 250$ for the Case 2 Nonevaporating Spray

r/x	0.034	0.067	0.101	0.134	0.168
Diameter Size Range (μm)					
10-30	1.33	1.06	0.81	0.87	0.42
30-50	1.41	1.14	1.03	0.88	0.57
50-70	1.28	1.17	0.94	0.71	0.66
70-90	1.53	1.24	1.09	0.88	0.34
90-110	2.52	2.25	1.31	1.13	0.49
110-130	2.27	2.05	2.13	1.19	0.73
130-150	1.33	3.07	2.03	1.69	0.35
150-170	2.78	2.95	3.83	1.72	2.1
170-190	4.20	5.37	--	1.41	--

Table D.2.17. Collection Efficiencies for Liquid Mass
Flux Data Obtained by Isokinetic Sampling
at Major Axial Measurement Stations

x/d	Percent of Injector Mass Flow Rate Collected
50	88.6
100	84.3
250	85.7
500	99.0

1. Report No. NASA CR-174668		2. Government Accession No.		3. Recipient's Catalog No.	
4. Title and Subtitle A Theoretical and Experimental Study of Turbulent Nonevaporating Sprays				5. Report Date June 1984	
				6. Performing Organization Code	
7. Author(s) A. S. P. Solomon, J-S. Shuen, Q-F. Zhang, and G. M. Faeth				8. Performing Organization Report No. None	
				10. Work Unit No.	
9. Performing Organization Name and Address The Pennsylvania State University Mechanical Engineering Building University Park, Pennsylvania 16802				11. Contract or Grant No. NAG 3-190	
				13. Type of Report and Period Covered Contractor Report	
12. Sponsoring Agency Name and Address National Aeronautics and Space Administration Washington, D.C. 20546				14. Sponsoring Agency Code 505-31-42	
15. Supplementary Notes Final report. Project Manager, Robert Tacina, Aerothermodynamics and Fuels Division, NASA Lewis Research Center, Cleveland, Ohio 44135.					
16. Abstract Measurements and analysis limited to the dilute portions of turbulent nonevaporating sprays injected into a still air environment were completed. Mean and fluctuating velocities and Reynolds stress were measured in the continuous phase. Liquid phase measurements included liquid mass fluxes, drop sizes and drop size and velocity correlation. Initial conditions needed for model evaluation were measured at a location as close to the injector exit as possible. The test sprays showed significant effects of slip and turbulent dispersion of the discrete phase. The measurements were used to evaluate three typical models of these processes: (1) a locally homogenous flow (LHF) model, where slip between the phases were neglected; (2) a deterministic separated flow (DSF) model, where slip was considered but effects of drop dispersion by turbulence were ignored; and (3) a stochastic separated flow (SSF) model, where effects of interphase slip and turbulent dispersion were considered using random-walk computations for drop motion. For all three models, a k-ε model was used to find the properties of the continuous phase. The LHF and DSF models did not provide very satisfactory predictions for the present measurements. In contrast, the SSF model performed reasonably well - with no modifications in the prescription of eddy properties from its original calibration. Some effects of drops on turbulence properties were observed near the dense regions of the sprays. Treatment of such dense flow effects will require extension of the present SSF model. The SSF approach, however, appears to provide an attractive formulation for treating nonlinear interphase transport processes in drop-laden turbulent flows.					
17. Key Words (Suggested by Author(s)) Spray modeling Turbulence interactions Combustor			18. Distribution Statement Unclassified - unlimited STAR Category 07		
19. Security Classif. (of this report) Unclassified		20. Security Classif. (of this page) Unclassified		21. No. of pages 137	
				22. Price* A07	

National Aeronautics and
Space Administration

Washington, D.C.
20546

Official Business

Penalty for Private Use, \$300

SPECIAL FOURTH CLASS MAIL
BOOK



Postage and Fees Paid
National Aeronautics and
Space Administration
NASA-451

NASA

POSTMASTER: If Undeliverable (Section 154
Postal Manual) Do Not Return
